Tatiana Ivanova

ATOMIC LAYER DEPOSITION OF CATALYTIC MATERIALS FOR ENVIRONMENTAL PROTECTION

ACTA UNIVERSITATIS LAPPEENRANTAENSIS 859

LUT University

Tatiana Ivanova

ATOMIC LAYER DEPOSITION OF CATALYTIC MATERIALS FOR ENVIRONMENTAL PROTECTION

Dissertation for the degree of Doctor of Science (Technology) to be presented with due permission for public examination and criticism in MUC Auditorium, Mikkeli University Consortium, Mikkeli, Finland on the 11th of June, 2019, at noon.

Acta Universitatis
Lappeenrantaensis 859

Supervisor Professor Mika Sillanpää
LUT School of Engineering Science
Lappeenranta-Lahti University of Technology LUT
Finland

Reviewers Professor Markku Leskelä
Department of Chemistry
University of Helsinki
Finland

Dr. Mikko Utriainen
VTT, Sensing & Integration, MEMS
Finland

Opponent Professor Mikko Ritala
Department of Chemistry
University of Helsinki
Finland

ISBN 978-952-335-384-8
ISBN 978-952-335-385-5 (PDF)
ISSN-L 1456-4491
ISSN 1456-4491

Lappeenranta-Lahti University of Technology LUT
LUT University Press 2019

Abstract

Tatiana Ivanova
Atomic Layer Deposition of Catalytic Materials for Environmental Protection
Lappeenranta 2019
78 pages
Acta Universitatis Lappeenrantaensis 859
Diss. Lappeenranta-Lahti University of Technology LUT
ISBN 978-952-335-384-8, ISBN 978-952-335-385-5 (PDF), ISSN-L 1456-4491, ISSN 1456-4491

The reduction of toxic pollutants emitted by human activities to ambient air is an important issue nowadays. The technological approach to this problem is the development of different oxidation techniques together with catalytic materials, which can convert toxic emission products to safe compounds. Current methods for the preparation of heterogeneous catalysts which fully control the structure, size and composition are limited. The atomic layer deposition (ALD) technique can create catalytic thin films with precise thickness and structure control even on complex substrates.

The present work describes the development of TiO_2, CeO_2 and Ag-doped CeO_2 catalytic thin films deposited by ALD in order to find their capacity for the decomposition of toluene and soot. TiO_2 catalytic films with different thicknesses were grown to investigate their nucleation delay and changes in their polycrystalline structure and the impact of these on their photocatalytic properties. It was shown that porous glass filters coated by TiO_2 in combination with a dielectric barrier discharge (DBD) reactor could decompose toluene at a concentration of 2450 ppm with the specific input energy (SIE) of 336 J/l.

In CeO_2 studies it was found that a deposition temperature of 300 °C changes the structural properties of the catalytic thin films. The combination of small crystallites, larger clusters and the existence of Ce^{3+} in CeO_2 catalytic films showed 100% soot decomposition at 450°C under loose contact mode. The doping of CeO_2 with Ag in the ratio of CeO_2:Ag = 10:1 by ALD reduced the soot decomposition temperature to 390°C. It was proposed that Ag^+ sites could promote oxygen species and reduce the Ce ions in stoichiometric CeO_2 from Ce^{4+} to Ce^{3+}. Most catalytic thin films prepared by ALD showed good durability after repetitive tests of soot decomposition.

Keywords: atomic layer deposition, titanium dioxide, cerium dioxide, silver, photocatalytic activity, soot oxidation, toluene.

Acknowledgements

This study was carried out at Lappeenranta University of Technology in the School of Engineering Science.

I would like to deeply thank my supervisor Prof. David Cameron for his significant support and for the guidance throughout the years of my PhD study.

I would like to thank Prof. Markku Leskelä and Dr. Mikko Utriainen for reviewing my thesis and giving the valuable comments.

I am grateful to Prof. Mikko Ritala for agreeing to act as an opponent.

I would like to thank Prof. Mika Sillanpää for giving me an opportunity to complete the PhD study. My thanks also go to Prof. Yuri Part for her valuable comments to this thesis.

I would like to acknowledge my colleagues from Lappeenranta University of Technology, Masaryk University and Leibniz Institute for Plasma Science and Technology from whom I learned so much. Special thanks must go to Tomáš Homola, Philipp Maydannik, Tommi Kääriäinen and Tomáš Hoder for their valuable contribution to my work.

Thanks to all my colleagues from laboratory of Green Chemistry and particularly to Evgenia, Marina, Eduard, Anton for fun and support.

In addition, I would like to thank my family: my parents Olga and Vladimir, brother Andrei and my parents in law Irina and Igor for their love and endless support. From the bottom of my heart I would like to thank my husband Oleg for his huge motivation, help, support, love and understanding! I am deeply grateful to my daughter Stefania for bringing happiness, new experience and helping me in developing time management skills.

Tatiana Ivanova

May 2019

Espoo, Finland

Contents

Abstract

Acknowledgements

Contents

List of publications **9**

Nomenclature **13**

1 Introduction **15**

2 Principles of atomic layer deposition 17
2.1 ALD characterization – saturation, linearity, and ALD window 17
2.2 Catalysts development by ALD 18
3 Methods of VOCs oxidation and diesel soot combustion 21
3.1 VOCs oxidation 21
3.1.1 Non-thermal plasma 21
3.1.2 Dielectric barrier discharge reactor 22
3.1.3 The properties and hazardous effects of toluene 23
3.2 Diesel soot combustion 24
3.2.1 Diesel exhaust and soot formation 24
3.2.2 Soot oxidation reactions 25
3.2.3 Catalytic processes of soot removal 26
3.2.4 Classification of soot oxidation catalysts 26
4 Structure and catalytic properties of TiO_2, CeO_2 and Ag-doped CeO_2 and their deposition by ALD 29
4.1 TiO_2 for VOCs oxidation 29
4.1.1 Structure and photocatalytic properties of TiO_2 29
4.1.2 TiO_2 catalytic thin films grown by ALD 30
4.2 CeO_2 and Ag-doped CeO_2 for diesel soot combustion 31
4.2.1 The use of CeO_2 for soot oxidation 31
4.2.2 ALD grown CeO_2 catalytic thin films 33
4.2.3 Silver doping of CeO_2 for soot oxidation 34
4.2.4 Silver doping in ALD grown films 37

5 Materials and methods 39

5.1 Catalytic thin film deposition 39
5.1.1 Deposition of TiO_2 catalyst 39
5.1.2 Deposition of CeO_2, Ag_2O and Ag-doped CeO_2 catalysts 39
5.2 Substrate surface pretreatment 40
5.3. Catalytic thin film characterization 41
5.3.1 Spectroscopic ellipsometry (SE) 41
5.3.2 X-ray diffraction (XRD) 41
5.3.3 Scanning electron microscopy (SEM) 42

5.3.4 Atomic force microscopy (AFM)....42
5.3.5 X-ray photoelectron spectroscopy (XPS)....42
5.3.6 UV-Vis spectroscopy....42
5.4 Catalytic film application....42
5.4.1 Toluene abatement with a single-stage DBD reactor....42
5.4.2 Soot generation and decomposition....44

6 Results and Discussion....47

6.1 TiO_2 film properties and their application for toluene decomposition....47
6.1.1 Study of TiO_2 thin film nucleation and growth on planar substrates....47
6.1.2 ALD growth of TiO_2 catalyst on porous substrates....50
6.1.3 Application of TiO_2 for toluene decomposition in DBD reactor....52
6.2 ALD synthesis of CeO_2, Ag_2O and Ag-doped CeO_2 catalysts and their use for soot oxidation....55
6.2.1 CeO_2 catalyst grown by ALD....55
6.2.2 Ag_2O and Ag-doped CeO_2 catalysts grown by ALD....58
6.2.3 Application of CeO_2, Ag_2O and Ag-doped CeO_2 catalyst in diesel soot combustion....60

7 Conclusions and further research **63**

References **65**

List of publications

I. **Ivanova T.V.**, Hoder T., Kääriäinen M.-L., Komlev A., Brandenburg R., and Cameron D.C., Enhancement of Atmospheric Plasma Decomposition of Toluene Using Porous Dielectric Conformally Coated with Titanium Dioxide by Atomic Layer Deposition, *Science of Advanced Materials* 6 (2014) 2098-2105(8).

II. Cameron D.C., Krumpolec R., **Ivanova T.V.**, Homola T., Cernák M., Nucleation and initial growth of atomic layer deposited titanium oxide determined by spectroscopic ellipsometry and the effect of pretreatment by surface barrier discharge, *Applied Surface Science* 345 (2015) 216–222

III. **Ivanova T.V.**, Toivonen J., Homola T., Maydannik P.S., Kääriäinen T., Sillanpää M., Cameron D.C., Atomic Layer Deposition of Cerium Oxide for Potential Use in Diesel Soot Combustion, *Journal of Vacuum Science & Technology A* 34 (2016) 031506.

IV. **Ivanova T.V.**, Homola T., Bryukvin A. and Cameron D.C., Catalytic Performance of Ag_2O and Ag Doped CeO_2 Prepared by Atomic Layer Deposition for Diesel Soot Oxidation, *Coatings* 8 (2018) 237

Author's contribution

I. The author performed the literature survey, most of the experimental and analysis work, and wrote the first draft of the paper.

II. The author performed ALD of TiO_2 thin films and AFM analysis, and wrote parts of TiO_2 film deposition, growing mechanism and surface morphology analysis.

III. The author performed the literature survey, most of the experimental and analysis work except X-ray diffraction (XRD) and X-ray photoelectron spectroscopy (XPS) analysis, and wrote the first draft of the paper.

IV. The author performed the literature survey, most of the experimental and analysis work except X-ray diffraction (XRD) and X-ray photoelectron spectroscopy (XPS) analysis, and wrote the first draft of the paper.

Other publications by the same author

I. **T. V. Ivanova**, P. S. Maydannik, D. C. Cameron Molecular layer deposition of polyethylene terephthalate thin films, Journal of Vacuum Science & Technology A **30**, 01A121, 2012

II. D. C. Cameron , **T. V. Ivanova**, Molecular Layer Deposition, ECS Transactions 58 *263-275*, 2013

III. **T. V. Ivanova**, G. Baier, K. Landfester, E. Musin, S. A. Al-Bataineh, D. C. Cameron, T. Homola, J. D. Whittle, M. Sillanpää, Attachment of Poly(l-lactide) Nanoparticles to Plasma-Treated Non-Woven Polymer Fabrics Using Inkjet Printing, Macromolecular Bioscience, 15(9) 1274-82, 2015

IV. T. Homola, V. Buršíková, **T.V. Ivanova**, P. Souček, P. S. Maydannik, D. C. Cameron, J. M. Lackner, Mechanical properties of atomic layer deposited Al2O3/ZnO nanolaminates, Surface and Coatings Technology, 284, 198-205, 2015

V. **T. V. Ivanova**, R. Krumpolec, T. Homola, E. Musin, G. Baier, K. Landfester, D. C. Cameron, M. Černák, Ambient air plasma pre-treatment of non-woven fabrics for deposition of antibacterial poly (l-lactide) nanoparticles, Plasma Processes and Polymers, 10 (14), 1600231, 2017

VI. S. Sampath, M. Shestakova, P. Maydannik, **T. V. Ivanova**, T. Homola, A. Bryukvin, M. Sillanpää, R. Nagumothu and V. Alagan, Photoelectrocatalytic activity of ZnO coated nano-porous silicon by atomic layer deposition RSC Advances, 6, 25173, 2016

VII. E. Iakovleva, P. Maydannik, **T. V. Ivanova**, M. Sillanpää, W. Z. Tang, E. Mäkilä, J. Salonen, A. Gubal, A.A. Ganeev, K. Kamwilaisak, S. Wang, Modified and unmodified low-cost iron-coating solid wastes as adsorbents for efficient removal of As(III) and As(V) from mine water, Journal of Cleaner Production 133, 1095-1104, 2016

VIII. S. Sampath, P.Maydannik, **T. V. Ivanova**, M. Shestakova, T. Homola, A. Bryukvin, M. Sillanpää, R. Nagumothu, V. Alagan, Efficient solar photocatalytic activity of TiO_2 coated nano-porous silicon by atomic layer deposition, Superlattices and Microstructures, 97, 155-166, 2016

IX. S. Sampath, P. Maydannik, **T. V. Ivanova**, T. Homola, M. Sillanpää, R. Nagumothu, V. Alagan, Structural and morphological characterization of Al_2O_3 coated macro-porous silicon by atomic layer deposition, Thin Solid Films 616, 628–634, 2016

Conferences

I. **T. V. Ivanova**, P. S. Maydannik, D. C. Cameron, Molecular layer deposition of polyethylene terephthalate thin films, AVS ALD 2011 Conference, Cambridge, Massachusetts, USA, 26-29 June 2011.

II. **T. V. Ivanova**, T. Hoder, M. L. Kääriäinen, D. C. Cameron, Enhancement of VOC removal from air by combining atmospheric plasma and photocatalytic porous dielectric coated by atomic layer deposition, 13th International Conference on Plasma Surface Engineering, Garmisch-Partenkirchen, Germany, 10-14 September 2012.

III. **T. V. Ivanova**, T. Höder, D. C. Cameron, Plasma catalytic degradation of organic contamination in air, 9th Asian-European International Conference on Plasma Surface Engineering, Jeju, South Korea; 08/2013

IV. **T. V. Ivanova**, E. Musin, T. Homola, G. Baier, M. Sillanpää, D. C. Cameron, Nanocapsule attachment to non-woven fabrics after plasma treatment using inkjet printing, 23rd Annual Conference of the Australasian Society for Biomaterials and Tissue Engineering, April 22nd -24th, 2014, Lorne, Australia; 04/2014

V. **T. V. Ivanova**, T. Kääriäinen, J. Skogström, M. Sillanpää, D. Cameron, Atomic Layer Deposition of Cerium Oxide for Potential Use in Diesel Soot Combustion, 14th Int. Conf. on Atomic Layer Deposition, Kyoto, Japan; 06/2014

Nomenclature

Abbreviations

AFM - atomic force microscopy
ALD - atomic layer deposition
ALE - Atomic Layer Epitaxy
CVD - chemical vapor deposition
DBD - dielectric barrier discharge
DCSBD - Diffuse Coplanar Surface Barrier Discharge
DFT - density functional theory
DPF - diesel particulate filter
DPFs - diesel particulate filters
FESEM - field emission scanning electron microscope
FTIR - Fourier transform infrared spectroscopy
GPC – growth per cycle
IPC - in-plasma catalysis
MW-CNT - multi-wall carbon nanotubes
NTP - Nonthermal plasma
PAHs - polycyclic aromatic hydrocarbons
PE-ALD - plasma-enhanced atomic layer deposition
PM - particular matter
PPC - post plasma catalysis
QC - quantum confinement
SCS - solution combustion synthesis
SE - spectroscopic ellipsometry
SIE – specific input energy
SOC - surface oxygen complex
TGA - thermogravimetric analysis
TPO - temperature programmed oxidation
TWCs - three-way catalysts
UV - ultraviolet
UV-Vis - ultraviolet–visible spectroscopy
VOCs – volatile organic compounds
VW - Volmer–Weber
XPS - X-ray photoelectron spectroscopy
XRD - X-ray diffractometry

1 Introduction

Air pollution is one of the major issues in the world nowadays and it is mainly produced by human activities. The main substances emitted to the atmosphere are carbon dioxide (CO_2), nitrogen oxides (NOx), sulfur oxides (SOx), carbon monoxide (CO), volatile organic compounds (VOCs), particulate matter (PM), chlorofluorocarbons (CFCs), ammonia (NH_3) and toxic metals [1]. Air pollution affects the environment, global warming and human health. Many technologies and strategies have been developed and applied for the reduction of air pollution. Heterogeneous catalysts play a critical role in industrial chemical production due to their efficiency in reduction of environmental pollutants. Despite the variety of other preparation methods for heterogeneous catalysts, atomic layer deposition (ALD) is a highly promising technique. It allows the uniform and controllable deposition of catalytic materials on complex substrates with high surface area [2]. Accordingly, the amount of research work based on well-known catalysts such as titanium dioxide (TiO_2) and cerium dioxide (CeO_2) grown by ALD for treatment of pollutants has increased during the last 20 years.

The traditional removal methods for VOCs such as absorption, adsorption, and incineration have many technical and economical disadvantages. Nowadays, new technologies (e.g., plasma technology, photocatalysis and biological processes) attract high attention. Nonthermal plasma (NTP) technology has been extensively studied for environmental protection because it can be operated at a low temperature and atmospheric pressure [3,4]. It has compact configuration, ease of operation, and cost-effectiveness. The combination of NTP with a photocatalyst can highly improve energy efficiency and reduce the amount of by-products generated during VOC decomposition [5]. TiO_2 has been deeply investigated because its band gap is in the range of UV-light and it is able to remove VOCs from the environment, especially from air and wastewater, under ultraviolet (UV) radiation. The UV light generated in the dielectric barrier discharge (DBD) plasma system can be used to activate the photocatalytic properties of TiO_2. For maximizing active catalytic sites, porous substrates with a high surface area can be used and uniformly coated with ALD. In addition, properties of TiO_2 thin films grown by ALD are very important for understanding photocatalytic activity during VOCs abatement and have been investigated in this thesis.

Another significant environmental pollutant arising from the emissions of diesel engines is particulate matter (PM). The strict control of the amount of PM in the environment has forced the development of different after-treatment technologies in engine emission systems [6]. PM consists mainly of soot particles (from a few up to hundreds of nanometers (nm)), which originate from incomplete oxidation of fuel. PM can be trapped with diesel particulate filters (DPFs) and soot can be decomposed to CO_2 at 200-400 ˚C exhaust gas temperature. Platinum (Pt) is the catalyst most often used for this purpose, but it has a relatively high cost. One of the most promising replacements for Pt catalysts has been found to be CeO_2. The use of CeO_2 and ceria-based materials in three-way catalysts (TWCs) has been intensively studied for automobile exhaust gas treatment [7]. CeO_2 has unique properties of uptake and release of oxygen and variation of the stoichiometric composition between CeO_2 and Ce_2O_3. The capabilities of the redox couple can be enhanced by doping with other elements, and silver is one of the examples. Ag-doped CeO_2 was also found to increase the rate and reduce the temperature of soot decomposition [8]. As catalytic coatings can be applied in diesel particulate filter systems which have a complex surface area, ALD is suggested as a promising technique for uniform distribution

of catalytic materials. The control of ALD temperature, surface morphology and dopant concentration can promote catalytic properties of CeO_2 and Ag-doped CeO_2.

The thesis has seven chapters. The first four chapters describe principles of ALD, structure and catalytic properties of thin films (i.e. TiO_2, CeO_2, Ag_2O and Ag-doped CeO_2) grown by ALD, their application for VOC oxidation and diesel soot combustion. Chapter 5 "Materials and Methods" provides an overview of scientific techniques and analytic methods that were developed and used in the thesis. Chapter 6 presents the discussion of the original results obtained in this work. Conclusions and further research plans are summarized in Chapter 7.

2 Principles of atomic layer deposition

ALD is a thin film deposition technique, which is closely related to the chemical vapor deposition (CVD) process. ALD is a unique method suited to fabrication of thin films on substrates of different shapes. ALD is a self-limiting, surface controlled layer-by-layer process and is based on sequential pulses of gaseous precursors which react with chemical groups on the surface. Repeating of ALD cycles leads to desired film thickness [9]. ALD (also known as Atomic Layer Epitaxy (ALE)) was developed independently in the Soviet Union in the beginning of the 1960s by S.I. Koltsov and V.B Aleksovskii [10,11,12], and in the late 1970s by T. Suntola in Finland [13,14,15,16].

One ALD cycle consists basically of four steps and is illustrated on Figure 1: 1) The first precursor is pulsed into the reactor chamber and adsorbs on surface sites of the substrate; 2) The reactor chamber must be purged with inert gas in order to remove the remaining precursor; 3) The second precursor is introduced into the chamber and reacts with available chemical sites from the first precursor; 4) Inert gas purges the chamber from the unreacted second precursor and reaction by-products. The process must be repeated until the appropriate film thickness is achieved.

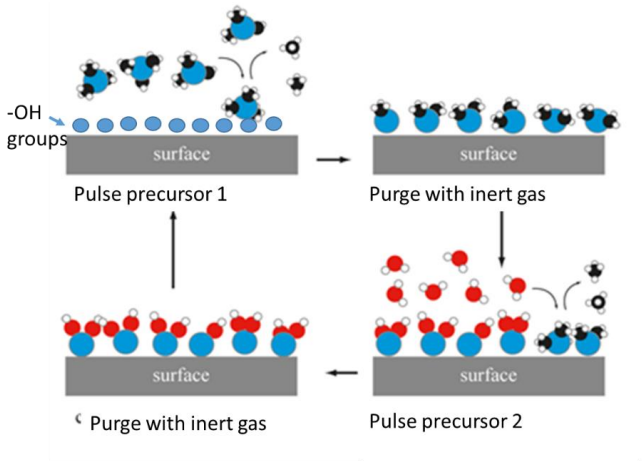

Figure 1. Diagram of a single cycle of the ALD process

2.1 ALD characterization – saturation, linearity, and ALD window

The precursor pulse and purge times need to be adjusted to avoid either too long processes, non-uniform film or CVD growth mode. The pulse and purge times should be optimized such that the substrate surface is saturated with precursor molecules and all unreacted by-products are removed from the chamber. Typical time scales for one pulse or purge may vary from one millisecond to tens of seconds depending on the reactor type, reactivity of precursors, growth temperature, and even on surface morphology. One of the main ALD characteristics is the self-saturation nature of the surface reactions happening during one cycle. The saturation curve shows how much exposure time is needed for one of the precursors to saturate surface groups and to get a constant growth per cycle (GPC). The saturation curve can be described by a

Langmuir isotherm because of the chemisorption nature of ALD process and illustrated in Figure 2 (a). Linear growth rate of the thin film with increasing number of deposition cycles can indicate thickness control during ALD process with a self-limiting behavior and is represented as a straight line (Figure 2b). Usually, perfect linear line increase can be obtained with higher number of ALD cycles but growth can be different during first few layers due to nucleation effects on the surface (e.g. different amount of reactive sites or different chemical growth mode). An ALD process window can be defined as the temperature range in which growth of a monolayer of the film is saturated (Figure 2c). Outside the ALD temperature window, some chemical and physical processes (i.e. condensation, decomposition, etching, incomplete reaction or re-evaporation) can destroy the ALD behavior. If the deposition temperature is too low, the growth of the film is not possible due to insufficient thermal energy for surface reactions and/or prevention of physical adsorption of precursor molecules or too high due to excess condensation of precursor. At a high deposition temperature, a higher growth rate can be observed due to the decomposition of precursor molecules; a lower rate can be caused by desorption or re-evaporation of chemically-adsorbed surface species. It is important to note that the GPC is not necessarily constant within the ALD window [17].

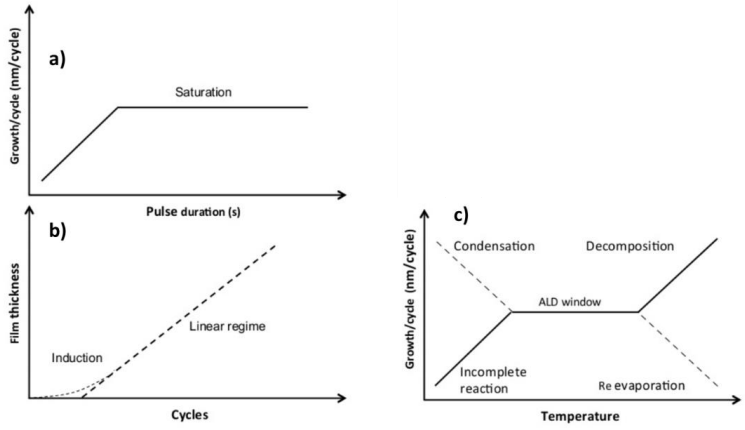

Figure 2. Characteristic of ALD processes: a) Precursor saturation, b) Linear growth per cycle, c) Flat "ALD window"

2.2 Catalyst development by ALD

Catalysis can be used for accelerating the rate of chemical reactions and chemical transformation. One of the major applications of chemical catalysts is reduction of the process temperature and reaction rate during the conversion of carbonaceous oil, gas, coal and biomass to fuels and chemicals. Globally, the catalyst market is estimated to be approximately between $16.3 and $20.6 billion per year [18,19]. A heterogeneous catalyst is the most common in industry because it can be easily separated from the products. Usually, industrial heterogeneous catalysis involves the reaction of gases being passed over the surface of solid metals, metal oxides or zeolites [20]. The most preferred form for catalyst supports in industry are solid materials with high surface area, which can provide additional catalytic function to improve the overall performance of the catalyst.

Various techniques such as precipitation, solution combustion synthesis (SCS), chemical vapor deposition (CVD), solvothermal synthesis, electrodeposition, sol-gel techniques and atomic layer deposition (ALD) have been reported for the synthesis of various catalytic materials [21]. Most of these methods can suffer from nonuniformity when they are used to deposit catalytic coatings on a high-aspect-ratio structures or porous substrates, and this may reduce catalytic performance. Among these methods, ALD is a technology which is able to meet the criteria for the design and synthesis of heterogeneous catalysts. ALD allows conformal catalytic coatings to be deposited on complex structures with extraordinary reproducibility due to the self-limiting nature of its gas-surface reactions [2,22,23,24,25,26].

In the past few years, theoretical and experimental investigations for the understanding of ALD surface reaction chemistry have been carried out. The annual number of ALD publications related to catalysis reveals a growing interest in ALD for catalytic applications [27]. Among all thin films deposited by ALD technique, metals and metal oxides are the most important materials because of their initial application in the semiconductor industry. In catalysis, metal oxides are widely used for the creation of catalytic sites, photocatalysis and the deposition of protection layers on other catalytic materials [28].

3 Methods of VOCs oxidation and diesel soot combustion

3.1 VOCs oxidation

3.1.1 Non-thermal plasma

Volatile organic compounds (VOCs), nitrogen oxides (NO_x), carbon oxides (CO and CO_2), and particulates are the major contributors to air pollution. Among all of these pollutants, VOCs are organic chemicals which endanger human health and are harmful to the environment. VOCs are released from burning fuel such as gasoline, wood, coal, or natural gas. They are also released from many consumer products such as cigarettes, solvents etc. [29,30]. They have quite high vapor pressure at a room temperature, which results in a large number of molecules evaporating or subliming from the liquid or solid form and entering ambient air. The most efficient methods of removing VOCs are thermal and catalytic combustion [31]. However, non-thermal catalytic combustion is becoming one of the most attractive method because of the much lower operation temperature and the production of no undesirable compounds such as dioxins and nitrogen oxides. Non-thermal plasma (NTP) can be the most effective air-cleaning technology for purifying indoor air from toxic gas contaminants [32,33]. It has been used for the removal of VOCs, carbon monoxide (CO), sulfur dioxide (SO_2), and nitrogen oxide (NO_x) in the presence of moisture without preheating the fuel gas. Moreover, NTP systems have many other advantages such as an easy operation and the possibility of use at room temperature and under ambient air [34,35]. A heterogeneous catalyst can be applied directly into or after the discharge zone in NTP reactors. When the catalyst is packed in the plasma reactor and can be directly activated by the plasma it is called single-stage plasma or in-plasma catalysis (IPC) [36]. In the post plasma catalysis (PPC) configuration the catalyst is located downstream from the NTP reactor. These two NTP reactor configurations are illustrated on Figure 3 [37]. In both cases, plasma can be generated continuously or in pulsed mode. The catalytic material can be applied in a powder form in a packed bed reactor, can be coated on reactor walls or electrodes, or deposited as a layer on porous supports (usually powder, pellets, fibers or porous solid foam).

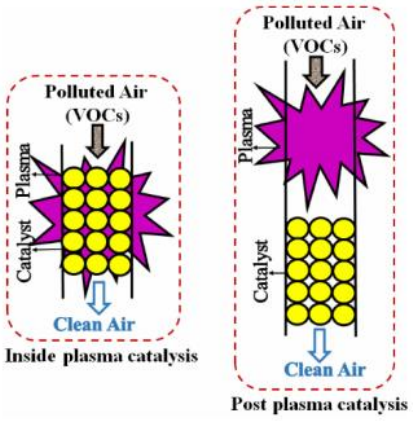

Figure 3. Schematic diagram of continuous plasma-catalysis process [37]

In this thesis, the IPC with TiO_2 thin films coated on porous glass substrates using the ALD technique were applied and investigated for toluene abatement. The combination has the advantage for toluene removal efficiency at a low operating temperature.

3.1.2 Dielectric barrier discharge reactor

Conventional NTP reactors exist in different variations such as pulsed discharges (PD), dielectric barrier discharge (DBD), atmospheric pressure plasma jets (APPJ), packed-bed reactors, microwave, and gliding arc discharges, etc. [38]. Dielectric barrier discharges (DBDs) are quite simple, scalable and can be used at atmospheric pressure compare with various types of NTPs for VOC decomposition. There are two different well-known configurations of DBD reactors: planar and cylindrical (Figure 4) with the presence of one or more insulating layers between metal electrodes. When DBDs are used, embedded metal electrodes generate strong electric fields, and discharges are initiated at a dielectric surface. Discharges gap spacing may vary in the range of 0.1-10 mm for the atmospheric pressure thus requiring variable driving voltages with the amplitude of typically 10 kV [39].

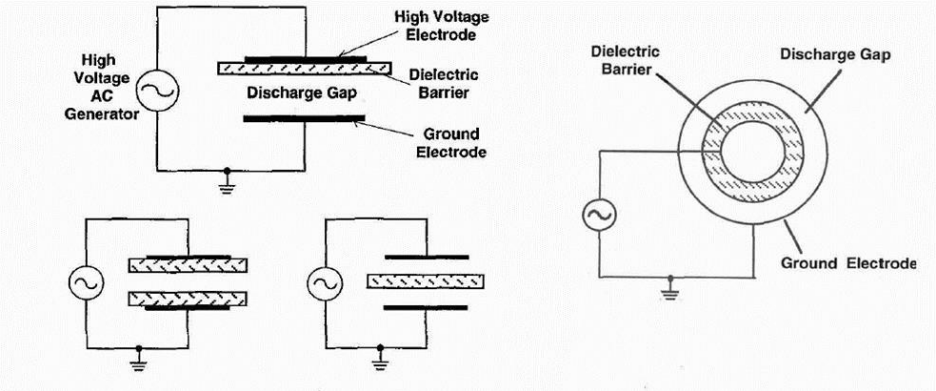

Figure 4. Common dielectric-barrier discharge configurations [39]

In the packed bed DBD reactor (Figure 5), pellets or spheres made of a dielectric or a ferroelectric material fill the space between the electrodes. The pellets can be either non-catalytic or catalytic. A very strong electric field can be generated on each pellet contacting point by applying a high voltage to the electrodes. The formation of microdischarges occurs in the void spaces between the pellets and on their surfaces [40]. A DBD reactor combined with catalyst is the most effective in terms of energy efficiency and carbon balance. The ultraviolet (UV) light generated from the plasma discharge can activate a photocatalyst (for example TiO_2, which absorbs UV light $\lambda \leq 400$ nm) deposited on porous supports to create electron–hole pairs. Consequently, plasma reactions and the TiO_2 photocatalyst can generate the reactive radicals and VOC removal efficiency can be enhanced [41].

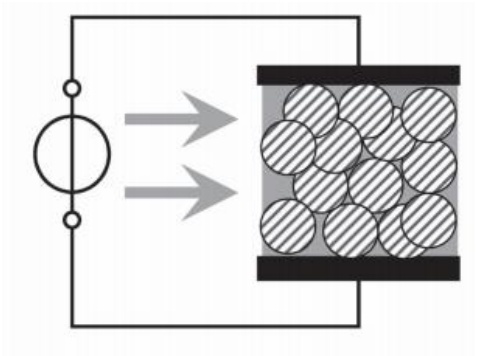

Figure 5. Illustration of parallel-plate packed-bed reactor with DBD [40]

3.1.3 The properties and hazardous effects of toluene

Toluene ($C_6H_5CH_3$) is an aromatic hydrocarbon compound, which is widely distributed in the environment. It is a matter constituent of gasoline and crude oil is used along with benzene and xylene to increase the octane rating. Toluene is emitted to the atmosphere from motor vehicles and aircraft exhaust, chemical spills, cigarette smoke, household products and industrial processes [42].Table 1 summarizes the basic properties of toluene.

Table 1. The physicochemical properties of toluene

Parameter	Value
Molar mass, g/mol	92.14
Density, g/mL	0.87 at 20°C
Melting point, °C	-95
Boiling point, °C	111
Solubility in water, g/L	0.52 at 20°C
Vapor pressure, kPa	2.8 at 20°C
Toxical limit from the Occupational Safety and Health Administration (OSHA)	200 ppm for toluene in air averaged over an 8-hour workday

The world production of toluene is expected to reach 19.6 million tons in 2020, which is worth almost USD 31.8 billion [43,44]. The effect and exposure of toluene on human health through inhalation, oral and dermal exposure routes was published in the report entitled “Toxicological Profile for Toluene” in 2000 [45]. A toluene concentration of 1800–2000 parts per million (ppm) for 1-hour inhalation exposure may be fatal for humans [46].

3.2 Diesel soot combustion

3.2.1 Diesel exhaust and soot formation

Over the past 25 years, the number of diesel-powered vehicles has risen in the world due to their lower fuel consumption with 40% improvement in a fuel economy, higher durability and in a 20% reduction in CO_2 emissions in comparison with gasoline-powered vehicles [47]. However, the main pollutants of diesel exhaust are particulate matter (PM) and nitrogen oxides (NO_x) emissions [48]. PM consists of solid carbon (soot) and unburned carbonaceous compounds originating from the incomplete combustion of fuel. Many factors such as an engine type and age may influence the composition of the particles [49]. PM may induce respiratory problems, skin cell alterations and cardiovascular diseases [50].

Legislation, which first was introduced in 1993, requires that the amount of particulates has to be controlled for diesel cars. As of now, the EURO 6 emission standard is in use in the European Union and the limit for particulate emission is limited to 5 mg/km for passenger cars and 10 mg/kWh for heavy-duty vehicles [51]. The exhaust composition usually includes harmful components in the amount of up to ~0.2 vol.% (Figure 6), where the amount of PM in the range 20–200 mg m^{-3} [52].

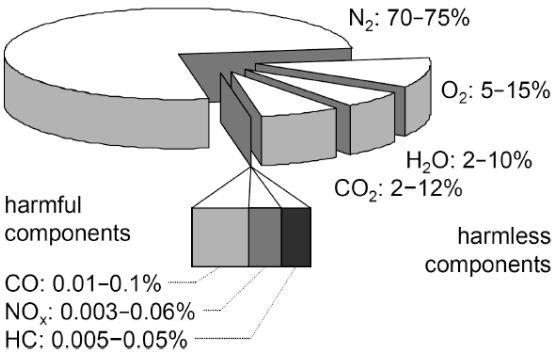

Figure 6. Composition of heavy-duty diesel engine exhaust [52,53]. The diagram shows the amount of basically harmless and harmful compounds in the exhaust gas of a diesel engine.

The formation of soot particles occurs in the region between the fuel spray and the fuel-rich side of the reaction zone of the diffusion flame. The process of soot formation can be described through 6 steps (Figure 7): 1) fuel aliphatic/aromatic molecules decomposition into alkenes, which then form acetylene precursors, 2) soot particle nucleation from heavy polycyclic aromatic hydrocarbons (PAHs), (3) particle growth from ~ 1-2 nm to 10-30 nm, (4) coagulation via reactive particle-particle collisions into larger spherical particles by sharing a carbon atom, (5) carbonization of particulate material, and, (6) oxidation of soot particles in non-premixed mixtures after the addition of oxygen-containing gases [54].

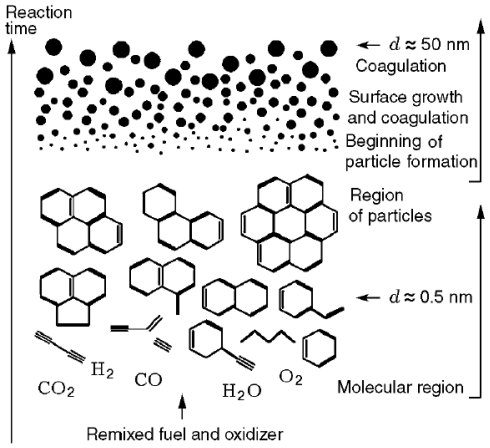

Figure 7. A schematic diagram of soot formation in homogeneous systems or in premixed flames [54].

3.2.2 Soot oxidation reactions

One of the first major research studies of uncatalyzed soot combustion was described by Neeft et al. [55]. They studied the effect of the oxygen concentration and the amount of water on different types of soot (flame soot-Printex-U and Diesel soot). It was shown that Printex-U can be used as an alternative for studying a diesel soot oxidation in the laboratories due to similar results between Printex-U and Diesel soot.

Zouaoui et al. [56,57] reported extensive work on uncatalyzed soot oxidation, where O_2 and NO could be used as oxidants. In general, several oxygen-containing gases such as O_2, H_2O, CO_2, NO or N_2O present in diesel exhaust emissions. It is remarkable that NO gases have a fairly low effect on a soot oxidation without O_2 in the mixture. On the other hand, the presence of O_2 and N_2O gases can promote quite a low soot oxidation temperature in the range of 200–580 °C [58]. CO_2 and H_2O show the lowest reactivity, with H_2O being slightly more reactive than CO_2. Therefore, several soot oxidation reactions can be described as follows [56]:

$$2C + O_2 \rightarrow 2CO \quad (1)$$
$$C + CO_2 \rightarrow 2CO \quad (2)$$
$$C + NO \rightarrow CO + \tfrac{1}{2} N_2 \quad (3)$$
$$C + N_2O \rightarrow CO + N_2 \quad (4)$$

For all the reactions, an oxygen atom reacts with a free carbon site and forms a surface oxygen complex (SOC) [59]. Thereafter, if water is present in the exhaust, carbon dioxide can be formed with oxygen exchange between two gas phase molecules:

$$CO + H_2O \rightarrow CO_2 + H_2 \quad (5)$$

The application of catalysts for soot decomposition may significantly influence soot oxidation reactions in the gas stream compared with non-catalyzed model [60].

3.2.3 Catalytic processes of soot removal

Diesel particulate abatement is based on after-treatment technologies for capturing and storing the exhaust soot. One of the mechanisms designed for soot removal is the so-called diesel particulate filter (DPF) [61,62]. A DPF requires periodic or continuous regeneration for the removal of accumulated soot from the filter. The temperature of the exhaust gas is around 250-450 °C, which is not enough for complete soot oxidation and may cause a high level of back pressure in the exhaust line. The DPF without catalysts requires a high temperature of about 600 °C to oxidize soot, which can cause additional fuel consumption and create thermal stress for the DPF [63,64]. Therefore, the combination of filters together with catalysts is very important for reducing the oxidation temperature of soot in the exhaust gas [65]. Catalysts can be used as precursors mixed into the fuel, as reactive chemicals injected upstream of the particulate trap, or as particulate trap coatings [58]. Particle filters combined with catalysts are considered to be the most practical method of soot oxidation from diesel exhaust gases. In addition, if the catalytic material is used as a coating, it may also have application to other devices such as sensors in the exhaust pipe to keep them clean by oxidizing the collected soot. Therefore, active soot oxidation catalysts have been extensively studied in the last 20 years [66].

The soot oxidation activity of catalysts can be described by several common designations: T_i is the temperature at which the oxidation initiates; T_m is the CO_2 peak-temperature (temperature programmed oxidation (TPO)); T_{50} is the temperature when 50% soot is oxidized; T_{10} is the onset temperature; T_f is the final temperature at which the soot is completely oxidized. However, a great variation in these designations can be found in the literature and, therefore, it is difficult to compare the activity of catalysts described in the publications.

Since the catalytic activity strongly depends on the interaction between the mixture of two solids and the gas, the contact between the soot and catalyst has a great influence on the soot combustion temperature [66,67]. Neeft et al. [67] defined two types of catalyst-soot contact conditions: tight and loose contacts. The tight contact condition is usually achieved in a mechanical mill to maximize the number of contact points between soot and catalyst. This method describes the catalytic morphology better, but it occurs less frequently in real conditions [68]. The loose contact condition can be obtained by gently shacking catalyst and soot with a spatula for about 1-2 min. Neeft et al. [66] observed that the contact between the catalyst and soot in a DPF is under the loose mode. In addition to the mentioned above spatula method, Van Setten et al. [69] also described loose contact methods such as shaking soot and catalyst in a bottle, dipping catalyst in a soot dispersion, and filtration from an artificial soot aerosol.

3.2.4 Classification of soot oxidation catalysts

Since the 1980s, many catalytic materials have been studied for soot oxidation in catalyzed diesel filters to replace the high costs of noble metal-based catalysts. Recent studies focus more on the development of non-noble metal materials which exhibit good mobility of oxygen species, generally referred to as the redox behavior [70]. Catalytic materials for diesel exhaust emission can be divided into:

1) Ceria-based catalysts. The reason for successful use of ceria in catalysts and especially in three-way catalysts (TWC) can be explained by its thermal stability and ability to store and release oxygen due to redox behavior of CeO_2 between Ce^{4+} and Ce^{3+} [71,72]. Bueno López et al. [73] showed a Mars–van Krevelen mechanism of CeO_2 lattice oxygen in soot oxidation.

The redox properties of CeO_2 can be strongly enhanced if other rare-earth or transition-metal elements (such as Cu, V, Mo, Co or Fe) are introduced into the cerium oxide lattice.

2) Perovskites based on Co, Cu, Mn, Ru, Fe etc., hydrotalcite, delafossite catalysts. These are rather stable materials [74,75] and induce NO_x decomposition [76]. The main advantages of these catalytic materials are assigned mainly to their changed redox properties and the promotional effect of co-ions.
3) Other metal oxides (for example La_2O_3 doped with K, Rh or Pt [77]), mixed metal oxides ($Pb_{10}La_5Co_{85}O_x$ [78]), alkaline metal ((Na, K, Cs) and alkaline-earth metal (Ca, Ba, Mg) oxides [79], in which catalytic activity is proportional with the electropositivity of the investigated metal ions.

Many different types of soot catalysts have been investigated in the past years but a comparison of the catalytic performance between them is quite difficult due to differences in experimental conditions such as the preparation methods of the catalysts and the origin of the carbon materials. Table 2 summarizes the catalysts with the lowest soot combustion temperatures under loose contact mode as this mode is closer to realistic conditions of use.

Table 2. Catalysts with the lowest soot combustion temperatures under loose contact mode

Catalysts	**Preparation method**	**Soot combustion T**	**Contact**	**Ref.**
Mo-K-Co (Al supported)	Co-impregnation from ammonium molybdate, cobaltous chloride, potassium nitrate. Calcined at 650 °C for 6 h.	T_{50} = 310 °C	loose	[80]
Ag (Zr supported)	Incipient wetness impregnation of ZrO_2 with aqueous $AgNO_3$, calcined at 500 °C for 3h.	T_{50} = 341 °C	loose	[81]
CeO_2	Precipitation from aqueous $Ce(NO_3)_3{\cdot}6H_2O$, calcined at 600 or 800 °C for 2 h.	T_{50} = 551 °C	loose	[82]
Pt (SiO2 supported)	Incipient wetness impregnation. Pt precursors: $Pt(NH_3)_4(OH)_2$, $H_2PtCl_6{\cdot}H_2O$, $Pt(NH_3)_4(NO_3)_2$ and $Pt(NH_3)_4Cl_2$. Calcination at 600 °C for 1 h.	T_m = 312 °C	loose	[83]
$BaAl_2O_4$	Precipitation from nitrate salts, calcined at 600 °C for 2 h and 800 °C for 6 h	T_m = 427 °C	loose	[84]
$Cu_{0.05}Ce_{0.95}$ (CA)	Co-precipitation from nitrates and citrate acid complex combustion synthesis from $Ce(NO_3)_3{\cdot}6H_2O$ and $Cu(NO_3)_2{\cdot}3H_2O$, calcined at	T_m = 438 °C	loose	[85]

	550 °C for 5 h.			
MnO_x-CeO_2	Sol-gel method from nitrate solutions. Calcined at 500 °C for 3 h.	T_m = 463 °C	loose	[86]
CuO-CeO_2	Citric acid sol-gel method from nitrates $Ce(NO_3)_3 \cdot 6H_2O$, $Cu(NO_3)_2 \cdot 3H_2O$. Calcined at 500 °C for 3 h.	T_m = 496 °C	loose	[87]
CeO_2	Citric acid sol-gel method from nitrates $Ce(NO_3)_3 \cdot 6H_2O$. Calcined at 500 °C for 3 h.	T_m = 501 °C	loose	[87]

4 Structure and catalytic properties of TiO_2, CeO_2 and Ag-doped CeO_2 grown by ALD

4.1 TiO_2 for VOCs oxidation

4.1.1 Structure and photocatalytic properties of TiO_2

It is well known that TiO_2, which has a non-toxic nature and has photocatalytic properties under UV light, can be used for the oxidation of organic compounds [88]. The photocatalysis of TiO_2 is schematically presented in Figure 8. The first and the most important step during photocatalytic oxidation is the formation of electron-hole pairs when the photocatalyst absorbs light with an energy equal to or higher than the band gap energy [89]. These holes and electrons may participate in redox reactions on the catalyst surface in the presence of air, oxygen and pollutant molecules. The holes can oxidize an adsorbed water molecule forming hydroxyl radicals $OH^{\cdot}$, which are highly reactive. In addition, electrons can reduce molecular oxygen O_2 to superoxide O_2^- [90]. Thus, the organic compounds can be decomposed by highly reactive species such as $OH^{\cdot}$ and O_2^- to non-toxic molecules such as CO_2 and H_2O. TiO_2 photocatalysts are capable of destroying many organic pollutions completely and the activation mechanism can be written as follows:

$$TiO_2 + h\nu \rightarrow h^+ + e^- + TiO_2, \quad (6)$$

where the h^+ and e^- are holes and electrons, which form powerful oxidizing and reducing agents, respectively.

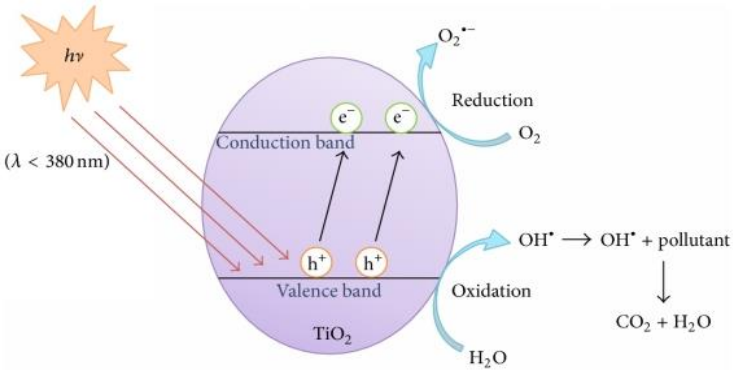

Figure 8. Schematic presentation of photocatalysis.

The photocatalytic activity of TiO_2 strongly depends on its crystal structure. TiO_2 can exist in three different crystallographic phases which are rutile, anatase and brookite. Brookite is a rare mineral, which is difficult to fabricate, with a band gap anywhere between 3 eV to 3.6 eV. The band gap energy of anatase is 3.2 eV, which corresponds to a wavelength of 385 nm, whereas the

bandgap of rutile is 3.0 eV, which is equivalent to 410 nm. This means that anatase needs more energy for activation. A UV radiation is able to activate TiO_2 catalyst [91]. Based on published material [92,93,94,95], there is no common agreement on which TiO_2 crystal structure works better as photocatalyst. Nevertheless, there are numerous examples of the higher photocatalytic activity of TiO_2 anatase structure compared to rutile due to its higher Fermi level [96], which increases the oxidation 'power' of electrons and promotes electron transfer from the TiO_2 to adsorbed organic molecules. In addition to that, the grain size and shape influence which crystal phase of TiO_2 will be more photocatalytically stable. In particular, when the grain size of TiO_2 is less than 15 nm, the anatase phase is more stable and reactive than rutile [97].

4.1.2 TiO_2 grown by ALD

The major scientific interest appeared in the development of anatase type TiO_2 nanoparticles with sizes less than 10 nm for enhancement of photocatalytic activity [98]. TiO_2 films have already been deposited by the ALD process using various titanium precursors such as halides, alkoxides, alkylamides, and heteroleptic compounds [99,100,101,102,103,104,105,106,107]. In addition to the selection of precursor, different deposition methods have been used to prepare TiO_2. However, ALD has the widest deposition temperature window for simple halide precursors such as $TiCl_4$, which has high volatility, temperature stability and reactivity with H_2O. The main reaction mechanism between the tetrachloride and water on a pore structure during the ALD process is presented on Figure 9 [108] and can be simplified as:

$$TiCl_4\ (gas) + 2\ H_2O\ (gas) \rightarrow TiO_2\ (solid) + 4\ HCl\ (gas) \quad (7)$$

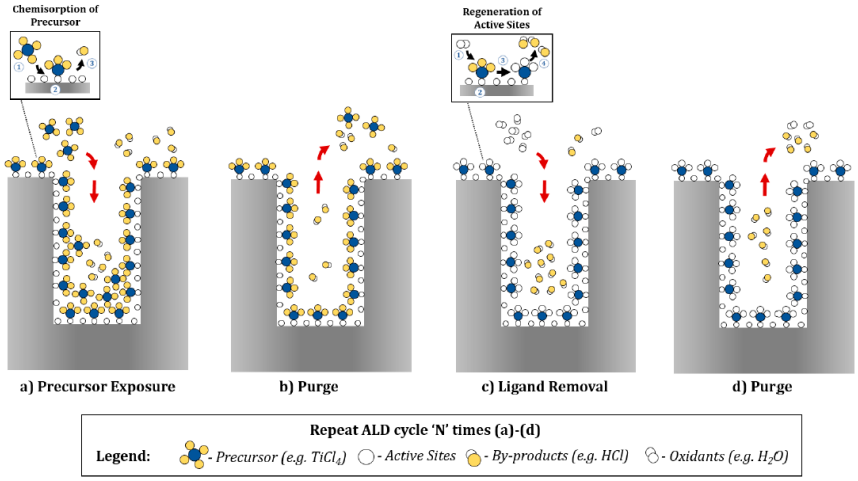

Figure 9. A schematic diagram of the ideal TiO_2 ALD cycle in a pore structure using $TiCl_4$ and H_2O precursors. (a) Introduction of precursor molecules and adsorption on the surface; (b) purge of the unreacted precursor molecules and reaction products; (c) introduction of ligand removal reactants, which react with the chemisorbed precursor molecules; and (d) purge of the excess reactants and reaction products [108].

It is important to know when the continuous TiO_2 film starts to grow and form a high-quality catalytic film. The formation of continuous TiO_2 thin films can be controlled by tuning the ALD conditions (such as temperature, precursors, number of cycles and initial substrate) as well as pre-treatment of the substrate. For example, Zhang et al. [109] have shown how oxygen plasma pre-treatment facilitates formation of nuclei on the surface of multi-wall carbon nanotubes (MW-CNT). Titanium-isopropoxide (TTIP) and H_2O were used as precursors for deposition of TiO_2 thin films. They observed that 200 ALD cycles of TiO_2 at 200°C deposition temperature are enough to obtain a continuous film after plasma pre-treatment, due to the full coalescence of the numerous growing nuclei. An average size of crystals of 7.4 nm was observed on MW-CNT without plasma pre-treatment coated with 200 ALD cycles of TiO_2, but they did not fully coalesce due to their low surface density.

The photocatalytic properties of TiO_2 were found to depend on the deposition methodology and chemistry, the growth temperature, stabilization of the desired crystal phase, the grain size and shape, film thickness, and supporting substrate [110, 111, 112, 113]. The ALD deposition temperature and thickness of TiO_2 thin films have a high impact on the crystal phase. Aarik et al. and M.-L. Kääriäinen et al. [114,97] showed that TiO_2 crystallized as anatase at the deposition temperature between 165-350 °C, but as rutile when grown above 350 °C. The photocatalytic efficiency of TiO_2 can be enhanced by careful control of the film thickness. Luttrell et al. [115] evaluated the photocatalytic activity as a function of epitaxial TiO_2 film thickness. They observed that the photocatalytic activity of anatase increased with film thickness of up to ~5 nm, while rutile films achieved their maximum photocatalytic activity with thickness of ~2.5 nm. This means that charge carriers excited deeper in the bulk contribute to the surface reactions in anatase than in rutile.

Another important factor that may enhance a catalytic activity is the increase of a surface area of either the catalyst itself or the support material, resulting in the production of more adsorption sites for pollutants to be oxidized. The ALD technique allows the growth of uniform TiO_2 films on highly complex substrates [116].

4.2 CeO_2 and Ag-doped CeO_2 for diesel soot combustion

4.2.1 The use of CeO_2 for soot oxidation

Cerium oxide is highly thermally stable material with a melting point of 2600 ºC and a density of 7.13 $g.cm^{-3}$. It has a face centered cubic (fluorite) crystal structure with a lattice constant of 5.11 Å (Figure 10) [117].

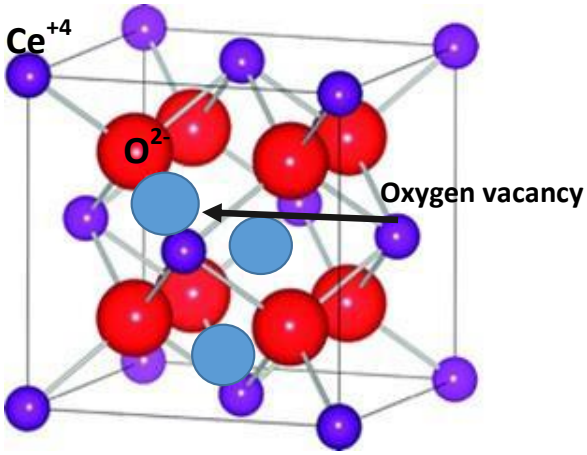

Figure 10. Crystal lattice structure of fluorite CeO_2 [118].

Many researchers have reported that CeO_2 and related materials have excellent activity in the treatment of exhaust gases from automobile engines and ceria-based catalysts have been implemented in several million vehicles in recent decades. The reason for such successful application of ceria as catalytic material in three-way catalysis (TWC) is related to its ability to take up and release oxygen while alternating between CeO_2 and CeO_{2-x} [119]. This property is called oxygen storage/release capacity (OSC) or redox behavior and may follow the retained reaction:

$$2CeO_2 \leftrightarrow Ce_2O_3 + 0.5O_2 \quad (8)$$

Oxygen storage capacity (OSC) is the major parameter of TWC performance and defined as the maximum amount of oxygen, which can be stored inside the catalyst. TWCs are widely used in the treatment of automotive exhausts to oxidize hydrocarbons, carbon monoxide and reduce nitrogen oxides NO_x, where engine exhaust gas composition is rich in oxygen, to harmless compounds such as H_2O, CO_2 and nitrogen (Figure 11). An important application of cerium oxide in TWCs has been found in the burning of harmful emissions from unburnt fuel and particulates to harmless gases by the following series of reactions at the lowest possible temperatures [120].

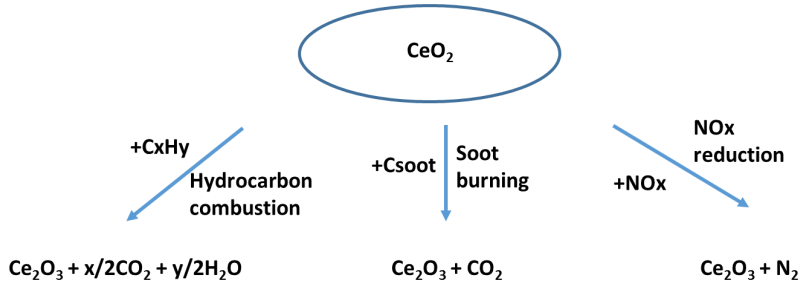

Figure 11. CeO_2 catalytic application for oxidizing hydrocarbons, carbon monoxide and reduction of nitrogen oxides.

Catalytic combustion of soot involving CeO_2 was described by Gross et al. [121], who proposed the strict reaction mechanism with the formation of superoxides, peroxides, oxygen vacancies and surface diffusion. The mechanism involves several complex steps and is shown in Figure 12.

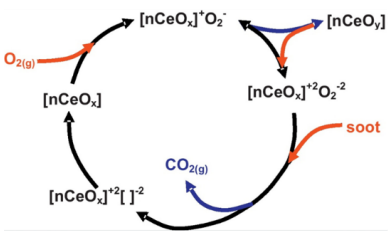

Formation of superoxide species:
$nCeO_x + O_2 \rightarrow [nCeO_x]^+O_2^-$
Conversion of superoxide into peroxide ions:
$[nCeO_x]^+O_2^- \leftrightarrow [nCeO_x]^{2+}O_2^{2-}$
Conversion of superoxide into the oxidized form of cerium oxide, 'y' being greater than 'x':
$[nCeO_x]^+O_2^- \leftrightarrow nCeO_y$
$[nCeO_x]^{2+}O_2^{2-} + C \rightarrow [nCeO_x]^{2+}[CO_2]^{2-}$
Reaction of peroxide with soot and formation of carbon dioxide:
$[nCeO_x]^{2+}[CO_2]^{2-} \rightarrow [nCeO_x]^{2+}[]^{2-} + CO_2$
Diffusion of oxygen species to yield reduced sites:
$[nCeO_x]^{2+}[]^{2-} \rightarrow nCeO_x$

Figure 12. Soot oxidation on ceria occurs by a mechanism involving superoxides and peroxides species [121].

4.2.2 ALD grown CeO_2 catalytic thin films

Cerium oxide can be synthesized by several methods such as precipitation [122], solution combustion synthesis [123], chemical vapor deposition [124], solvothermal synthesis [125], electrodeposition [126], sol–gel techniques [127], and atomic layer deposition (ALD) [128,129,130,131]. Reported precursors for the CeO_2 prepared by ALD are β-diketonates such as $Ce(thd)_4$ (thd = 2,2,6,6-tetramethyl-3,5-heptanedione), $Ce(thd)_3$phen (thd = 2,2,6,6-tetramethyl-3,5-heptanedionate, phen = 1,10-phenanthroline)cerium) [128], alkoxides such as $Ce(mmp)_4$ ((1-methoxy-2-methylpropan-2-olate)cerium) [132], cyclopentadienyls such as $Ce(iPrCp)_3$ [tris(isopropyl-cyclopentadienyl)cerium) [133], and heteroleptic cyclopentadienyl-amidinates such as $(Ce(iPrCp)_2$(N-iPr-amd) (bis-isopropylcyclopentadienyl-di-isopropylacetamidinate-cerium) [134]. H_2O, O_2 plasma and ozone (O_3) have been used as oxidants for the preparation of CeO_2 using ALD. A summary of previously used precursors for CeO_2 film growth by ALD is shown in Table 3.

Päiväsaari et al. [128] investigated CeO_2 ALD for buffer layer application using $Ce(thd)_4$ and $Ce(thd)_3$phen precursors and ozone at deposition temperature ranges of 175–375 °C and 225–350 °C, respectively. They observed narrow ALD windows of 175–250 °C for $Ce(thd)_4$ with the growth rate of 0.32 Å/cycle and 225–275 °C for $Ce(thd)_3$phen with the growth rate of 0.42 Å/cycle. The CeO_2 deposited thin films were polycrystalline on Si(100) substrates with the (200) and (111) peaks as the strongest reflections; these are thermodynamically favorable orientations for CeO_2.

Vangelista et al.[135] extended knowledge of the structural and chemical properties of ALD-deposited CeO_2 either on Si(111) or TiN substrates for finding the optimal properties for its application in microelectronics and catalysis. $Ce(thd)_4$ and ozone were used at 250 °C reaction temperature and obtained cubic polycrystalline CeO_2 films showed a dominant orientation of (200). XPS of CeO_2 showed a relative concentration of Ce^{3+} equal to 22.0% in CeO_2/Si and around 18% in CeO_2/TiN due to the presence of defects or charge compensating species on different substrates.

Several research groups [136,137,138] used $Ce(mmp)_4$ as a cerium precursor with water and obtained CeO_2 growth rates of 1.2–1.7 Å/cycle. The films showed low impurity levels.

Kim et al. [133] showed that CeO_2 thin films can be efficiently deposited by plasma-enhanced atomic layer deposition (PE-ALD). $Ce(iPrCp)_3$ and O_2 plasma were used as precursors. The obtained films were polycrystalline with cubic phases, impurity-free and nearly stoichiometric with a growth rate per cycles of 0.35 Å/cycle. The results showed that PE-ALD of CeO_2 could be a viable option as a future high-k material in the microelectronic industry.

The recent research by Golalikhani et al. [134] investigated the heteroleptic Ce precursor $Ce(iPrCp)_2$(N-iPr-amd) with H_2O. They observed a broad ALD window of 165–285 °C with a growth rate of 1.9 Å/cycle. CeO_2 polycrystalline films with cubic structure were achieved at 240 °C. XPS analysis showed that CeO_2 films were pure without any impurities with $CeO_{1.74}$ stoichiometry, which can be explained by the existence of oxygen vacancies in the films.

Table 3. Properties of cerium precursors used for ALD growth of cerium oxide.

Precursor	Melting point, °C	Growth rate, Å/cycle	Oxidizer	Evaporation temperature, °C	Ref.
$Ce(iPrCp)_3$	51	0.35	O_2 plasma	135	[133,139]
$Ce(mmp)_4$	105	1.7–1.2	H_2O	-	[136,137,138]
$Ce(thd)_4$	275	0.32	Ozone	140	[128]
$Ce(thd)_3$phen		0.42	Ozone	175	[128]
$Ce(iPrCp)_2$(N-iPr-amd)	Room temp	1.9	H_2O	145	[134]

3.2.3 Silver doping of CeO_2 for soot oxidation

Another interesting class of catalysts for diesel soot oxidation is silver-based materials. Ag doped CeO_2 has been studied in detail by many researchers [140,141,142,143,144,145,146], and considered one of the most efficient oxidation catalysts for soot combustion compared to other noble metals. Machida et al. [140] observed that Ag10%/CeO_2 catalyst managed to decrease the onset oxidation temperature of soot by more than 50 °C compared to bare ceria. This effect can be attributed to the enhanced formation of active oxygen sites promoted by Ag. The preparation and deposition methods of silver have also influence on catalytic activity. Yamazaki et al. [141] and Kayama et al. [147] investigated the mechanism of soot oxidation with rice-ball nanostructures, where silver was at the center with aggregated ceria particles on top of it. They evaluated soot oxidation by thermogravimetric analysis (TGA) and showed that CeO_2-Ag

prepared as the rice-ball nanostructure oxidized soot much more efficiently below 300 °C than CeO_2 or standard supported catalysts of Ag/CeO_2 (Figure 13).

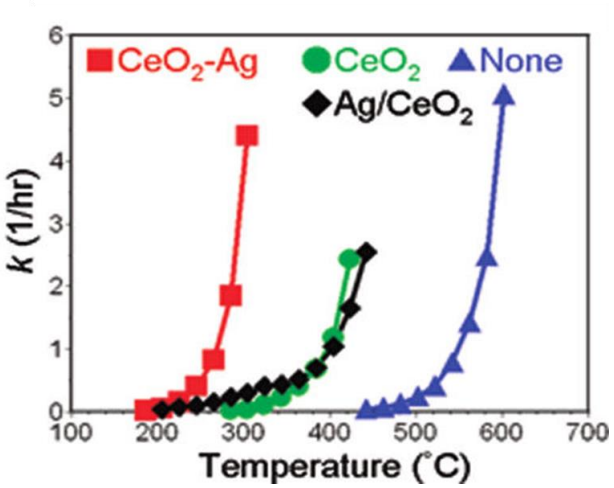

Figure 13. Evaluation of k vs. temperature of CeO_2-Ag rice-ball structure compared with conventional catalysts and the absence of a catalyst [147]

Figure 14 demonstrates that gaseous oxygen is adsorbed firstly on the surface of silver particles and then migrates to CeO_2 to form active oxygen species [141]. Furthermore, active oxygen species migrate on to the soot particle surface through the synergetic effect of CeO_2 and soot, and start to oxidize soot to CO_2. This approach addresses increasing oxygen species on silver/ceria interface. Preda et al. [143] supported this mechanism with density functional theory (DFT), where they showed charge transfer from silver to cerium oxide with formation of reduced Ce^{3+} ions and stronger bonding of gas-phase O_2 to oxidized Ag atoms.

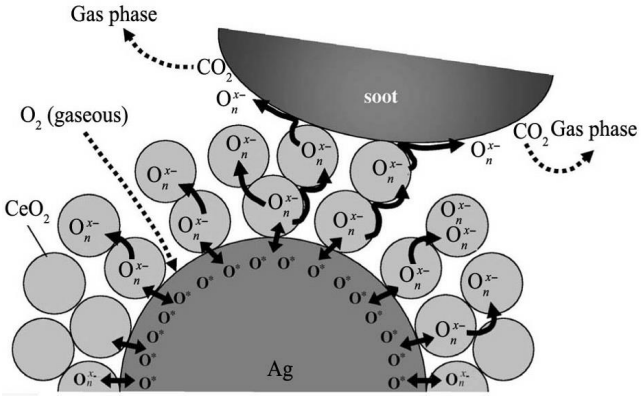

Figure 14. Schematic mechanism for soot oxidation over the CeO_2- Ag catalyst. Reprinted with permission from Ref. [141].

On the other hand, Shimizu et al. [142] showed in their work that the interaction between silver nanoparticles and the CeO_2 surface results in the enhancement of soot oxidation due to the formation of highly reactive surface oxygen (Figure 15). This behavior is similar to the surface oxygen of Ag_2O, which is the strongest soot oxidant. However, Ag_2O is deactivated after a single catalytic run and converts to Ag metal particles. Aneggi et al. [110] observed that it is likely that ceria maintains silver in an oxidation state, where Ag as metallic layer can be formed on the top of Ag_2O. Larger Ag_2O particles decompose into metallic Ag at the side opposite to the Ag_2O–CeO_2 interface and form a more powerful catalyst for soot combustion. They showed a Ce_5Ag catalyst had the lowest T_{50} compared with other tested samples (Zr_5Ag, Al_5Ag) prepared by incipient wetness impregnation.

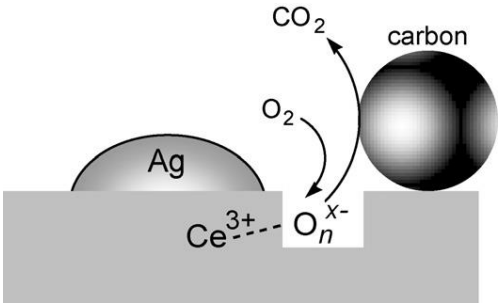

Figure 15. A Schematic diagram describing the mechanism of soot oxidation over Ag/CeO_2 catalyst. Reprinted with permission from Ref. [142]

Summarizing the available information, Ag doped CeO_2 catalysts can promote the formation of active oxygen species (peroxide and superoxide) from gas-phase O_2 adsorption or from the interface between Ag and CeO_2 and oxidize soot more efficiently at lower combustion temperatures.

4.2.4 Silver doping in ALD grown films

In addition to binary oxide deposition using ALD, multi-component oxides can be obtained by combining two or even more ALD processes in the one supercycle. The desired doped composition can be achieved by changing the cycle ratio of the base and doped materials. The main requirement for ALD of multi-component oxide films is similar deposition temperatures, otherwise, self-limiting behavior cannot be obtained. Most of the ALD processes for mixed oxides utilize organometallic precursors with O_3 processes for binary oxides.
Ag-doped CeO_2 can be prepared by a number of different methods such as precipitation [141], impregnation [148,149], and liquid-phase chemical reduction [146]. It is worth mentioning that no reports are available of ALD of silver oxide and Ag-doped CeO_2. The ALD process was mostly developed for zero-dimensional Ag due to a strong interest in its use for catalytic and plasmonic applications. The synthesis of silver nanoparticles from gas phase is quite difficult due to low thermal stability and low vapor pressure of the precursors. Previously, metal Ag nanoparticles have been prepared by plasma-enhanced (PEALD) and thermal ALD including a liquid injection ALD (LIALD) process. An overview of silver precursors used in ALD processes is summarized in Table 4.

Table 4. Summary of silver precursors studied for PEALD and thermal ALD metal Ag processes.

Ag precursor	Evaporation temp of Ag precursor, °C	Co-reactant	ALD window, °C	Growth rate, Å/cycle	Ref.
$Ag(O_2CtBu)(PEt_3)$	125	H_2/Ar	140	1.2	[150]
$Ag(fod)(PEt_3)$	106	H_2/Ar	120-140	0.3	[151]
$Ag(fod)(PEt_3)$	110	H_2/Ar	70,120,200	0.3	[152]
$Ag(fod)(PEt_3)$	95	NH_3	130	2.4	[153]
Ag(hfac)(1,5-COD) (dissolved in toluene)	130	propan-1-ol	123–128	0.16	[154]
	130	$tBuHNNH_2$	105–128	0.18	[155]
$Ag(hfac)(PMe_3)$	63 – 66	formalin (i.e. formaldehyde, 37 w % in H_2O with 10 % methanol in H_2O)	200	0.07	[156]
	63 – 66	$AlMe_3$ and H_2O	170-200	1 – 2 ng/cm^2 /cycle	[156]
$Ag(fod)(PEt_3)$	95	BH_3-$(NHMe_2)$	110	0.33	[157]

Based on the literature review, trimethylphosphine (hexafluoroacetylacetonalo)-silver $Ag(hfac)(PMe_3)$ precursor (Figure 16 b) was used at relatively high deposition temperature (200 °C) compared with others silver precursors, which makes it suitable for doping of CeO_2. TGA analysis of $Ag(hfac)(PMe_3)$ precursor showed that thermolysis occurs mostly over the temperature range 140-280 °C to leave a residue of metallic silver (Figure 16 a). In the report made by Dryden et al. [158], this Ag precursor [$Ag(hfac)(PMe_3)$] was evaporated at 95 °C and the film could be grown at 250-350 °C using a CVD process.

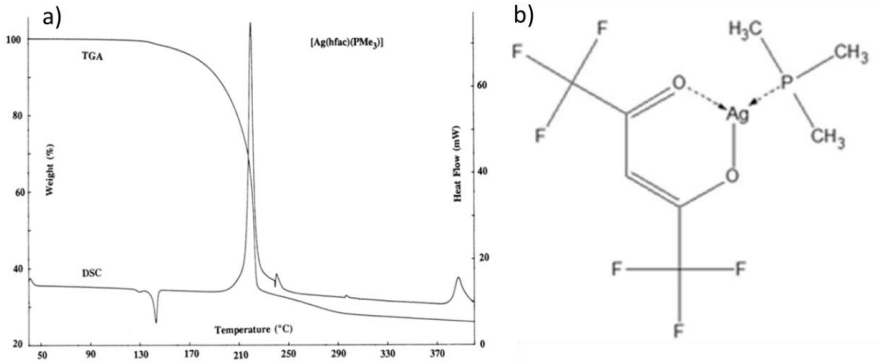

Figure 16**.** a) Thermogravimetric analysis (TGA, weight, %) and differential scanning calorimetry (DSC, heat flow, mW) traces for the thermolysis of [Ag(hfac)(PMe_3)]. In each case, the heating rate was 20 °C/min. b) View of the molecular structure of [Ag(hfac)(PMe_3)] [158].

5 Experimental methods

5.1 Catalytic thin film deposition

5.1.1 Deposition of TiO_2 catalyst

TiO_2 thin films were grown by atomic layer deposition in a TFS-500 ALD reactor (Beneq Oy) at 5-10 mbar ($5x10^2$ – $1x10^3$ Pa). TiO_2 was grown at 350 °C with four different thicknesses: 250, 500, 1000 and 1500 cycles on borosilicate porous glass filers (ROBU glasfiltergerate GMBH, Germany) 30 mm in diameter and 1 mm in thickness (Table 5). In addition to porous substrates, single-side polished Si (100) wafers (Si-Mat, Germany) of 15 mm × 15 mm were used for thickness and quality control of the TiO_2 films. Si wafers were cleaned of contaminations before deposition by using an ultrasonic bath with acetone, isopropanol and deionized water consecutively, each with a time of 300 s. Thereafter the substrates were dried with compressed air (**Papers I and II**). The porous borosilicate substrates were kept overnight at 350 °C in the reactor chamber under vacuum to remove residual moisture from the porous labyrinth before TiO_2 ALD deposition (**Paper I**).

Nitrogen (99.999%) was used as a carrier and purging gas. Titanium tetrachloride ($TiCl_4$) (99.0%, Fluka) and deionized water (H_2O) were used as precursors for the TiO_2 process. Bubblers with precursors were kept at 23°C. During deposition of TiO_2 on porous substrates, chemicals were introduced to the reactor in the sequence: $TiCl_4$ pulse – N_2 purge – H_2O pulse – N_2 purge of 10 s – 10 s – 8 s – 10 s (**Paper I**). TiO_2 was deposited on Si substrates with shorter pulsing and purging time in a sequence: $TiCl_4$ pulse – N_2 purge – H_2O pulse – N_2 purge of 0.6 s – 1 s – 0.25 s – 0.5 s (**Paper II**).

Table 5. Details of porous filters

Filter type	Pore size, µm	Pore volume, %	Specific surface area, Brunauer–Emmett–Teller (BET), m^2/gr
P2	40-100	36	0.13

5.1.2. Deposition of CeO_2, Ag_2O and Ag-doped CeO_2 catalysts

CeO_2, Ag_2O and Ag-doped CeO_2 catalytic thin films were deposited with an F-120 ALD reactor (ASM Microchemistry, Ltd., Espoo) at 1 mbar (**Papers III and IV**). Ozone was used as the co-reactant for above mentioned metal oxides and generated by an ozone generator (Wedeco Modular 4HC Lab, Herford, Germany) from a pure oxygen (>99.999%) source, with a concentration of approximately 120 g/m^3. $Ce(thd)_4$ (2,2,6,6-tetramethyl-3,5-heptadionatecerium), (Volatec, Porvoo) and (hfac)$Ag(PMe_3)$ (trimethylphosphine (hexafluoroacetylacetonalo)-silver) (99%; Strem Chemicals, Newburyport, MA, USA) were used as Ce and Ag precursors, respectively. $Ce(thd)_4$ and (hfac)$Ag(PMe_3)$ were evaporated at 160 °C and 80 °C, respectively. The sequence for CeO_2 deposition was $Ce(thd)_4$ pulse – N_2 purge – O_3 pulse – N_2 purge of 1.5 s – 2.5 s – 2.5 s – 2.5 s. CeO_2 deposition temperatures of 180, 200, 250, 300, and 350 °C were studied (**Paper III**). The sequence for Ag_2O deposition was chosen to be (hfac)$Ag(PMe_3)$ pulse

– N_2 purge – O_3 pulse – N_2 purge of 2.5 s – 2.5 s – 2.5 s – 2.5 s at reaction temperature of 200 °C.

The sequence for Ag-doped CeO_2 catalysts is presented in Figure 17 with the same pulse and purge times which were used for pure CeO_2 and Ag_2O thin films. During doping of CeO_2 with Ag, one supercycle consisted of n CeO_2 cycles, with n equal to 10, 20, and 30, and 1 cycle of Ag. In order to achieve CeO_2:Ag pulsing ratios of 10:1, 20:1, and 30:1, the supercycle was repeated 150, 75, and 50 times, respectively to obtained comparable film thicknesses (**Paper IV**).

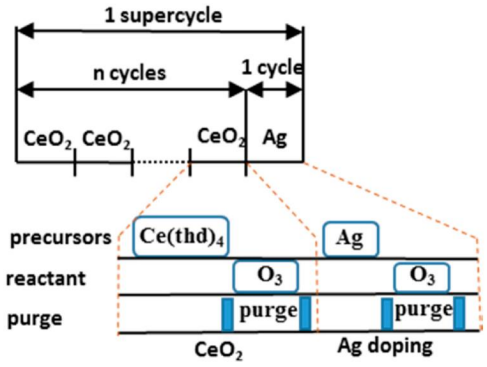

Figure 17. A schematic representation of the atomic layer deposition (ALD) supercycle used to deposit Ag doped CeO_2 catalytic thin films.

Silicon wafers (100) and stainless steel foil AISI 316 with a thickness of 0.025 mm (Goodfellow Cambridge, Ltd., London, UK) were used for ALD process control and for soot burning tests, respectively. The substrates were cut into pieces of 30x10 mm and cleaned using the procedure mentioned above in the section 5.1.1. Stainless steel foil was chosen as the substrate for soot oxidation analysis due to its relatively low weight, which minimizes the error during weighing for determining the amount of decomposed soot (**Papers III and IV**).

5.2 Substrate surface pretreatment

TiO_2 nucleation (crystallite size and density) and growth of continuous films deposited by ALD at 350 °C were evaluated on as-received single-side polished Si (100) wafers and on those pretreated by Diffuse Coplanar Surface Barrier Discharge (DCSBD) in air. The details of the DCSBD can be found from **Paper II** and the article [159]. Dynamic treatment mode (Figure 18) was applied for silicon substrates, where the samples were moved through the plasma above the dielectric surface for 5 sec with a distance between sample and ceramic surface of 0.3 mm. The power supplied to the DCSBD plasma system was 300–310W equivalent to approximately 1.5 Wcm^{-2}. The samples were subject to plasma directly before ALD process.

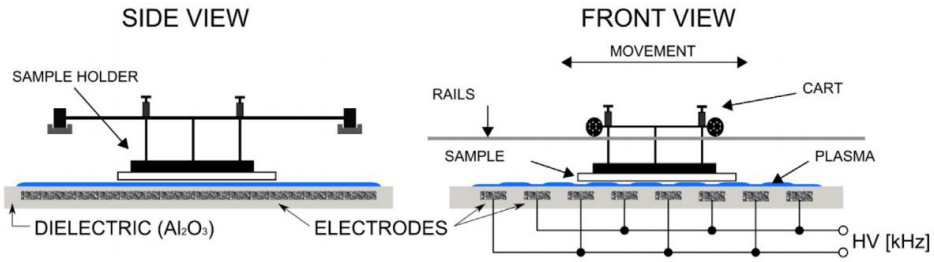

Figure 18. Schematic of experimental apparatus for plasma treatment of silicon substrates.

5.3 Catalytic film characterization

The catalytic thin films obtained during the research work were investigated by various methods such as spectroscopic ellipsometry (SE), X-ray diffractometry (XRD), field emission scanning electron microscope (FESEM) with EDX detector, UV-Vis spectrophotometer, atomic force microscopy (AFM) and X-ray photoelectron spectroscopy (XPS).

5.3.1. Spectroscopic ellipsometry (SE)

The thickness of the deposited catalytic films were measured with the spectroscopic ellipsometer J.A.Woollam M-2000UI (J.A.Woollam Co., Lincoln, NE, USA) in the wavelength range of 210-1500 nm at angles of incidence of 65°, 70° and 75°. The data were analyzed with WVASE software. Tauc-Lorentz parameters were used for TiO_2 thickness fitting and a Cauchy model was used for the other samples. The modelling of the ellipsometric data from plasma treated and untreated Si substrates before and after TiO_2 deposition was reported in **Paper II**, where the process is described in details in Appendix A.

5.3.2. X-ray diffraction (XRD)

The crystalline phases and orientation of the films were characterized by means of X-ray diffraction (XRD). A parallel beam of Cu Kα radiation was used. TiO_2 catalytic films on porous samples were measured with a Shimadzu XRD-7000 using CuKα (λ = 1.54 Å) as the X-ray source, operated at 35 kV and 30 mA. The scanning rate was 2 °/min in the 2θ range 20°–60° in the Bragg-Brentano configuration (**Paper I**). CeO_2, Ag_2O and Ag-doped CeO_2 catalytic thin films were studied by a Rigaku SmartLab® Type F XRD (Rigaku, Tokyo, Japan; Cu-Kα radiation, λ = 1.54 Å). The grazing incidence X-ray diffraction (GIXRD) scan was collected with a grazing incidence angle of 0.5°. A scan speed of 0.9°/min and 2θ values from 20° to 90° were used. The high resolution scan was taken with a speed of 0.045°/min (**Paper IV**).

Based on the XRD patterns, the grain sizes can be estimated by using Scherrer's equation:

$$\varepsilon = \frac{K\lambda}{b\cos\theta} \tag{5.1}$$

where ε is the apparent crystallite size, K is Scherrer's constant, λ is the wavelength of the radiation, b is the additional broadening due to the crystal size, and θ

is the Bragg angle. The grain sizes calculated from XRD can be compared also with SEM and AFM measurements.

5.3.3. Scanning electron microscopy (SEM)

The morphology and crystal sizes of TiO_2, CeO_2, Ag_2O and Ag-doped CeO_2 catalytic films were evaluated by field emission scanning electron microscope (FESEM) (Hitachi S4800) equipped with an EDAX EDX detector unit for determining which chemical elements were present in the thin films and estimating their relative quantity. The image obtained with SEM can be utilized so that the region of interest can be identified by the user and measured with the EDX.

5.3.4. Atomic force microscopy (AFM)

All catalytic films were measured by AFM using a Park NX10 (Park Systems, Suwon, South Korea) in noncontact mode with a cantilever force constant of 42 N/m to evaluate the surface topography features such as roughness and cluster size.

5.3.5 X-ray photoelectron spectroscopy (XPS)

The elemental composition and chemical bonding properties of catalytic thin films were investigated by XPS using an ESCALAB 250Xi (Thermo Scientific, UK) with a monochromated Al-Kα (energy of 1486.7 eV) x-ray source in the constant pass energy mode with a value of 50 eV. For high resolution spectra of Ce 3d and Ag 3d, a pass energy of 20 eV with a resolution 0.1 eV was used (**Papers III and IV**). An electron flood source was used in all measurements to minimize binding energy shifts due to charging effects. The binding energy of C1s (284.5 eV) was used for calibration. Sputtering with Ar^+ ions at 2 kV for 20 s was carried out to remove surface contaminations and actual carbon levels were obtained from the bulk material. AVANTAGE software (Version 5.938) was used with Smart type background for deconvolution and curve fitting using 70:30 Gaussian–Lorentzian peaks for CeO_2 (**Paper III**) and 90:10 Gaussian-Lorentzian peaks for Ag_2O and Ag/CeO_2 (**Paper IV**) .

5.3.6 UV-Vis spectroscopy

UV-visible transmittance studies of uncoated porous filters and with 500 and 1500 ALD-cycles of TiO_2 catalytic coating were carried out using a NICOLET 500 UV-Vis spectrophotometer in the wavelength range 200–600 nm. UV transmission spectra of bare and coated materials were measured to ensure that even the internal surfaces of the porous substrates could be activated by UV radiation from micro discharges (**Paper I**).

5.4 Catalytic film application

5.4.1. Toluene abatement with a single-stage DBD reactor

The performance of TiO_2 catalytic thin films with 500, 1000 and 1500-ALD cycles was tested by the decomposition of toluene in a single stage parallel-plate dielectric barrier discharge (DBD) reactor (**Paper I**). In order to have a stable temperature in the flow type DBD reactor, the discharge was driven for 10 min without toluene injection. The reactor presented in Figure 19 consists of two parallel plates of borosilicate glass. High voltage electrodes were made from

copper tape and were attached to the outer sides of the glass plates. A Teflon spacer was used between the glass plates to provide 1 mm of discharge zone, in which TiO_2 coated porous filters were placed. The size of the discharge zone was 100 x 50 mm. The non-thermal plasma was generated by applying 1 kHz AC voltage to the reactor, which was measured by a 1000:1 high-voltage probe (Tektronix probe P6015A). The reactor current (I) was measured by the potential across an appropriate series resistor. The power (W) (current–voltage multiplication) was computed and was simultaneously shown by an oscilloscope (Tektronix TDS 3052). The Lissajous figure method was used for calibration of the exact power estimation from the current–voltage product values. The specific input energy (SIE) was varied by changing the applied voltage and was calculated as:

$$SIE\left(\frac{J}{l}\right) = \frac{Power(W)}{Gas\ flow\ rate\ (\frac{l}{s})} \tag{5.2}$$

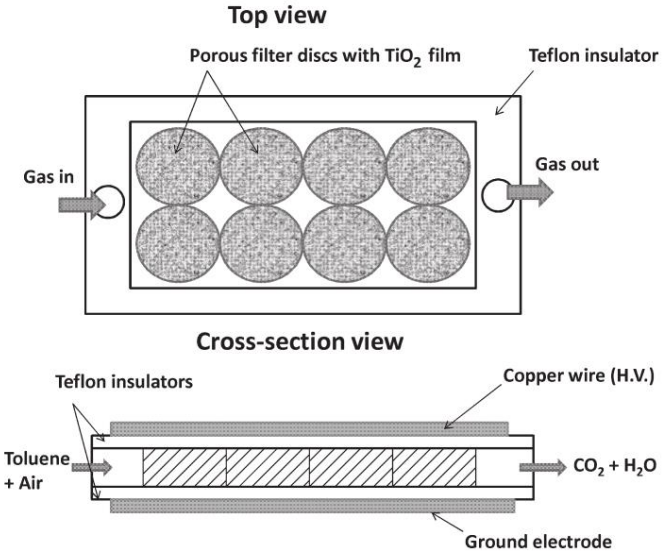

Figure 19. A schematic diagram of the single-stage DBD reactor packed with porous filters covered by TiO_2 catalysts (top and cross-section views).

The complete experimental setup is presented in Figure 20 and all measurements were carried out at room temperature and atmospheric pressure. A motor-driven syringe pump (1) was used for toluene introduction. The toluene was diluted by a synthetic airflow (20% oxygen and 80% nitrogen) to a concentration of 2450 ppm with the flow rate fixed at 1250 ml/min by a mixture system (2). The flow of diluted toluene was pulsed with two-way solenoid valve (3) into the plasma DBD reactor (4) or to the exhaust. An on-line Fourier transform infrared spectroscopy (FTIR) (Gasmet CR-2000, Ansyco, Germany) (5) was used for the detection of organic compounds and the formation of oxides. Measurements of the gas stream were made at 5 sec

intervals and the gas cell of the FTIR was heated to 60 °C to prevent any possible condensation.

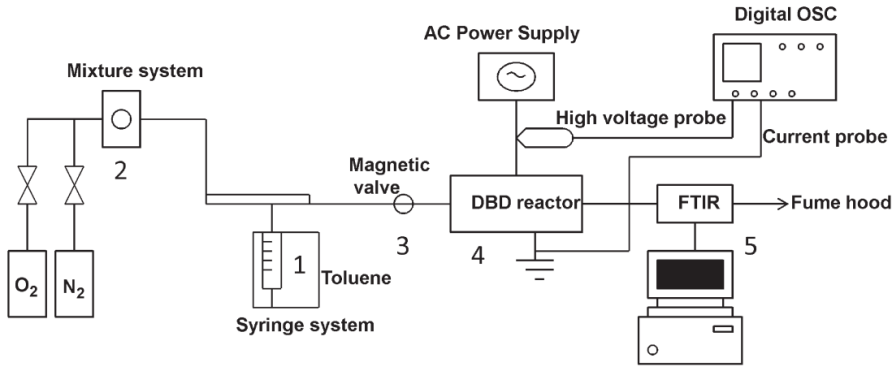

Figure 20. Experimental setup for toluene abatement

The CO_2 and CO selectivities were calculated as follows:

$$S_{CO2}\ (\%) = \frac{[CO2]}{[CO2]+[CO]}100 \tag{5.3}$$

$$S_{CO}\ (\%) = \frac{[CO]}{[CO2]+[CO]}100 \tag{5.4}$$

The carbon balance was obtained from the sum of two products:

$$Carbon\ balance\ (\%) = \frac{[CO]+[CO2]}{7*([VOC]_0-[VOC])}100 \tag{5.5}$$

where 7 means number of C atoms of toluene

5.4.2 Soot generation and decomposition

The custom-made soot deposition system is presented in Figure 21 (**Papers III and IV**). The system simulates the soot formation and collecting process that occurs in the exhaust of diesel engines. A diesel Webasto engine preheater (Webasto group, Stockdorf, Germany) was used for generation of particulate matter. Diesel fuel together with air were injected into the combustion chamber of the Webasto by an internal blower. The burnt fuel flowed from the chamber through the U-shaped pipe connected to the filter unit. The samples, on which soot should be deposited, were placed on a heating plate in the middle of the pipe and were exposed for 1.5 min to exhaust gases. The heater temperature was at 100-120 °C in order to avoid water condensation during soot deposition. The amount of accumulated soot on the samples was measured by weighing the samples before and after the soot deposition.

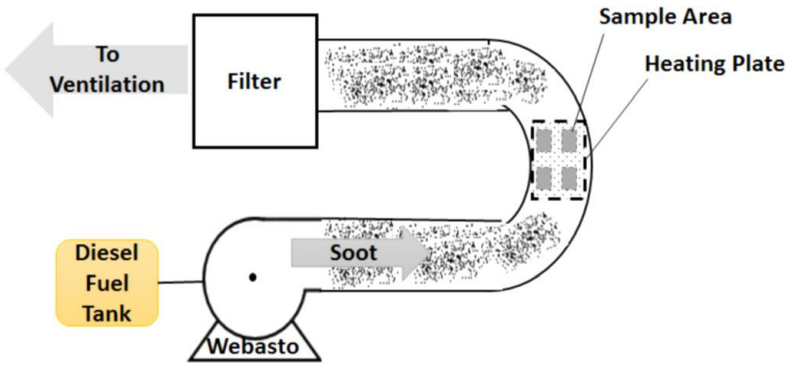

Figure 21. A schematic diagram of the soot deposition system.

In order to evaluate the catalytic activity of CeO_2, Ag_2O and Ag/CeO_2 thin films deposited on steel foil substrates by ALD under different process conditions, soot with the amount of 0.5-0.7 mg was accumulated on all samples from exhaust gas by the above-mentioned method. The catalyst/soot mass ratio was approximately 1:6. The soot decomposition on samples with catalytic coatings was performed with annealing tests in an oven by measuring their weight loss. The weight of samples was monitored for 4 hours with intermediate measurements in annealing temperature ranges of 350-490 °C and 300–490 °C in ambient atmosphere for CeO_2 and Ag/CeO_2, respectively. The annealing measurements were repeated three times for CeO_2 and five times for Ag_2O and Ag/CeO_2 catalysts to evaluate the reproducibility of the prepared catalysts.

6 Results and Discussion

6.1 TiO_2 film properties and their application for toluene decomposition

6.1.1 Study of TiO_2 thin film nucleation and growth on planar substrates

In the first place, it is essential to investigate the TiO_2 growth mechanism on planar substrates when establishing an ALD process on porous substrates. A series of TiO_2 thin films were deposited at 350 °C using $TiCl_4$ and H_2O precursors on as-received silicon substrates with a native oxide layer (named ”untreated”) and on silicon which has been treated by DCSBD source in air (named ”plasma treated”). The TiO_2 films have linear growth on both substrates with increasing number of ALD cycles from 3 up to 5000, as expected, with roughness of approximately 10% of the film thickness (Figure 22 a and b). However, the nucleation regime of TiO_2 films on plasma treated and untreated substrates is different (Figure 22 c and d). 50 and 80 ALD cycles are needed to form a continuous film on untreated and plasma treated silicon, respectively.

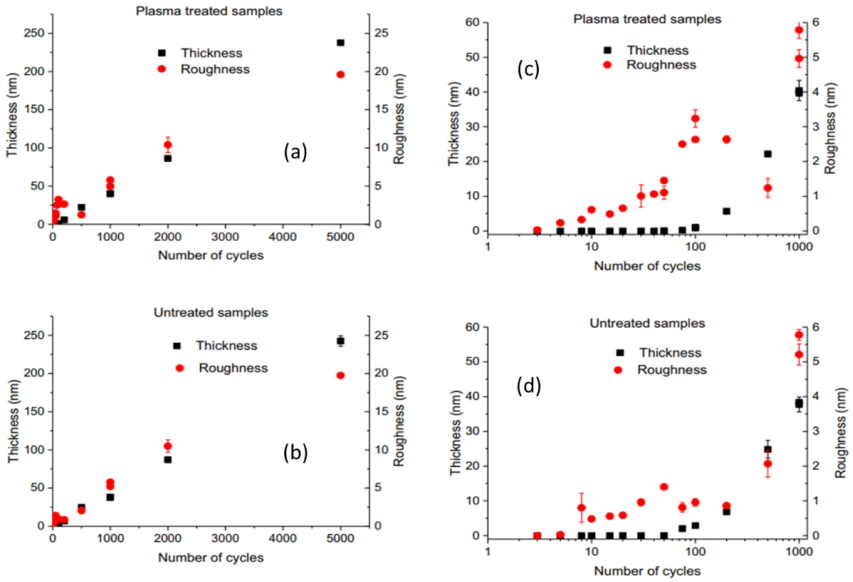

Figure 22. Film thickness and roughness vs. number of ALD cycles, (a) plasma treated, (b) untreated samples; initial growth region, (c) plasma treated (d) untreated. Note: Some error bars are not visible because the range is smaller than the data symbol.

No deposited material can be detected by ellipsometry for the first 3 and 5 cycles on plasma treated and untreated substrates, respectively. There is no continuous film formation with increasing number of ALD cycles up to 50 or 80 cycles on unteated or plasma treated substrates, respectively; the ellipsometric modeling showed zero thickness. Even though no film thickness can be detected in these ranges, the roughness increases with the number of cycles on both substrates. We can propose that isolated islands are formed before coherent film formation. The difference in film growth on plasma treated and untreated samples is not significant. A minor

distinctive difference was noticed in that continuous film formation took a greater number of cycles on plasma treated samples. This can be explained by 1) the roughness on plasma treated samples is larger and perhaps, more material is needed to cover rougher surface; 2) the thickness of the native oxide differs on the untreated substrate (2.1 nm) and on plasma treated samples (3.5nm). This may affect island formation.

Further investigation of the size of individual TiO_2 crystallites on substrates before the formation of a continuous film can be obtained from fitting the optical parameters of the ellipsometric model for TiO_2 thin films. The absorption edge obtained for thicker TiO_2 films was 3.31 eV, which corresponds to the anatase structure. This value is in a good agreement with XRD measurements of TiO_2 thin films deposited at 350 °C which showed that the anatase phase was dominant. With decreasing number of ALD cycles (≤ 50 cycles), where the film grows as isolated islands, the absorption edge of TiO_2 increases in energy (Figure 23 a). This is in a good agreement with the effect of quantum confinement (QC) in the isolated islands. The increase in bandgap, giving a large blue shift in the absorption edge, due to the decreasing size of the nanocrystals can be described by the effective mass model and adjusted equation for spherical crystallites:

$$\Delta E_g = \frac{h^2}{2D^2 m_0}\left[\frac{1}{m_e^*} + \frac{1}{m_h^*}\right] - \frac{3.6e^2}{4\pi\varepsilon_0\varepsilon_r D} \tag{6.1}$$

where h is Planck's constant, m_o is the electron mass, m_e^*, m_h^* are the effective electron and hole masses, respectively, e is the electronic charge, ε_0 is the permittivity of free space, ε_r is the relative permittivity and D is the crystallite diameter.

Based on the calculation from equation (6.1), the relation between the calculated bandgap blue shift and the diameter of spherical crystallites can be illustrated in Figure 23 (b). The hemispherical crystallite size taken from the Figure 23 (b) can be plotted vs number of ALD cycles (Figure 24). The island size increases linearly until a continuous film starts to grow. The crystal size calculated from blue shift was compared with crystallite size measured by AFM and plotted in Figure 24. AFM measurements showed somewhat larger crystallite diameter which suggests that the crystallites are not strictly hemispherical, for instance, their height is less than their radius.

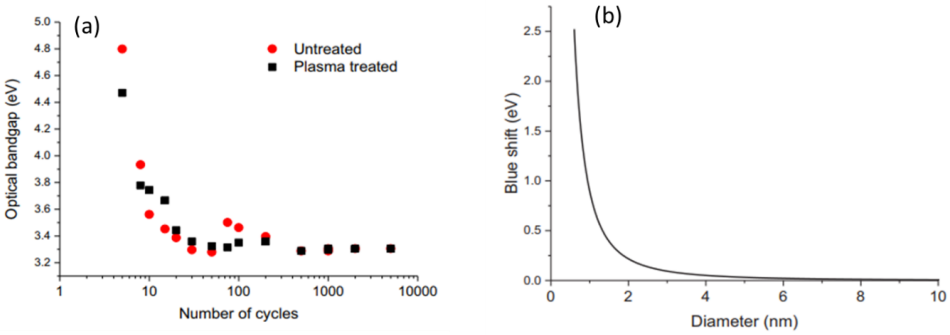

Figure 23. Optical bandgap of the TiO2 films as a function of the number of ALD cycles (a), Calculated bandgap blue shift as a function of the crystallite radius (b).

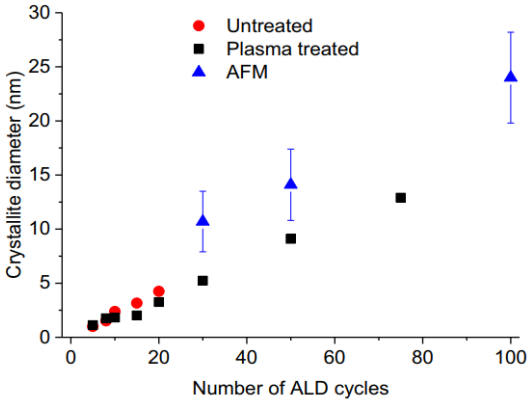

Figure 24. Crystallite diameter as a function of number of ALD cycles. The error bars shown on the AFM data points are estimates from the AFM image.

If it is assumed that crystallites are hemispherical, their height can be considered as the "film thickness". The surface roughness layer parameters can be obtained from the ellipsometry material model (srough.mat) with a mixed layer of film material and void of adjustable ratio. The details of the fitting are described in Appendix B of **Paper II**. The surface density of crystallites was plotted versus the number of ALD cycles (Figure 25). With increasing number of ALD cycles the crystallite density is dropped from initial value of around 3–4 × 10^{17} m^{-3} to approximately 2–3 × 10^{15} m^{-3}. This can be explained by Ostwald ripening, where larger crystallites are more energetically preferred than smaller ones. It is worth mentioning that crystallite density was slightly higher on plasma treated samples. This is in good correlation with crystallite size presented on Figure 24.

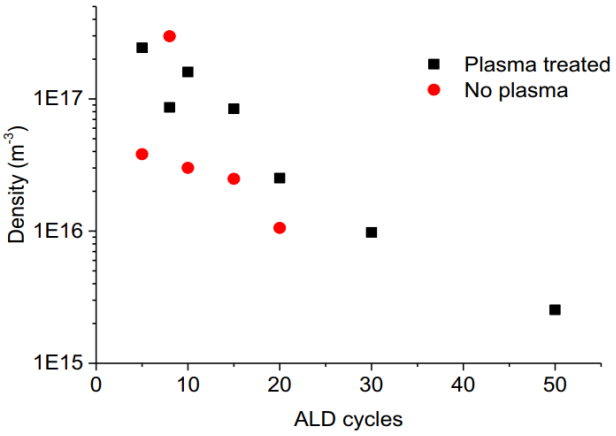

Figure 25. Surface density of crystallites as a function of the number of ALD cycles.

The growth rate of crystallite diameter of approximately 1.7 Å/cycle was obtained from Figure 24. This value can give the growth rate of TiO_2 film of 0.85Å/cycle, which is in contrast with the growth rate of 0.5 Å/cycle for thicker film. This difference can be explained by the fact that crystallites grow not only by the deposition of a surface layer, but also by the ripening process mentioned above.

6.1.2 ALD growth of TiO_2 catalyst on porous substrates

Since it is quite difficult to measure film thickness inside a porous labyrinth and estimate the uniformity of the film, EDX cross-section analysis of 1 mm porous substrates was done to demonstrate uniform coating of 1500 ALD cycles of TiO_2 on porous filter discs (Figure 8 in **Paper I**). It is very important to have sufficiently long precursor pulses, especially for porous substrates, to saturate the internal surfaces with reactive species and have uniform thin film thickness.

As was shown earlier, the initial substrate properties have an influence on TiO_2 growth. Figure 26a illustrates the weight gain of TiO_2 films deposited on porous discs versus the number of ALD cycles (**Paper I**). 500 cycles of TiO_2 showed a mass gain of approximately 7 mg. Assuming the density of TiO_2 is the bulk density of 4.23 g/cm^3, the thickness of the TiO_2 film is approximately 10.8 nm, which corresponds to a growth rate of 0.22 Å/cycle. At the same time ellipsometry measurements of 500 cycles of TiO_2 thin film deposited on Si substrate showed 19 nm, which corresponds to 0.38 Å/cycle. The difference in the growth rate of TiO_2 between calculated on porous materials and measured on Si is probably due to a TiO_2 density reduction on these substrates. This feature is commonly observed during thin film deposition on different substrates. Confirming the ALD linear growth of TiO_2 on porous substrates, the area of the anatase reflection (101) obtained from XRD measurements was calculated and plotted on Figure 26 (b). It shows that the area of the anatase peak grows linearly with increasing number of ALD cycles.

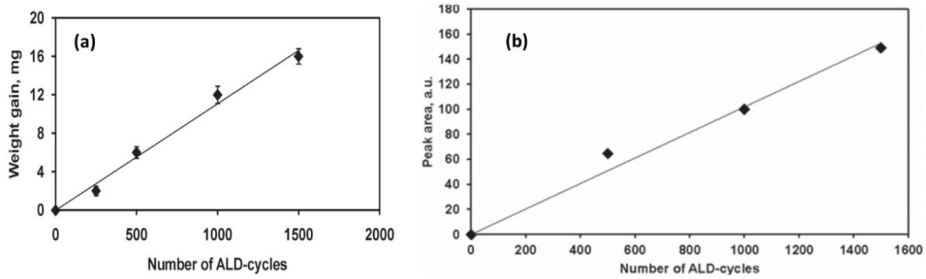

Figure 26. (a) Mass of TiO_2 deposited on porous substrates versus number of ALD-cycles obtained from weight gain measurements, (b) Area of anatase TiO_2 (101) XRD peak as a function of the number of ALD-cycles.

XRD analysis obtained from TiO_2 catalytic films on porous substrates is presented on Figure 27. These TiO_2 patterns exhibited mostly the anatase (101) reflection at $2\theta=25.3°$. A tiny rutile peak became visible on 1500 cycles of TiO_2 at $2\theta=27.4°$ and $2\theta=36.1°$.

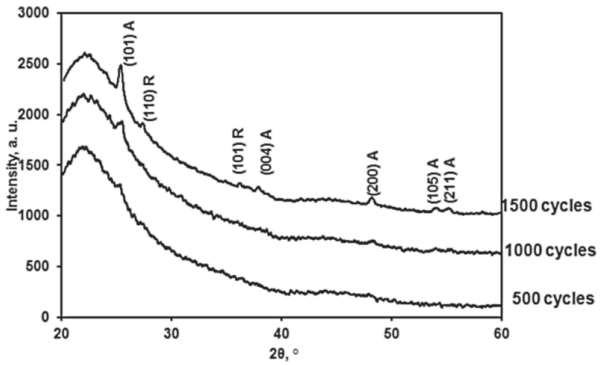

Figure 27. XRD patterns of TiO_2 films deposited at 350 °C on borosilicate porous discs with 500, 1000 and 1500 ALD-cycles.

SEM images of the internal surface of porous filters coated with different thickness of TiO_2 films are shown in Figure 28. The size of crystal grains detected with SEM was 27 nm, 55 nm and 75 nm for 500, 1000 and 1500 cycles of TiO_2. There is a tendency to increase the size of crystal grains from 27 nm up to 75 nm with increasing number of ALD cycles. These results have been compared in **Paper I** with the size of crystal grains calculated from Scherrer's equation and increased from 26 nm up to 44 nm with increasing number of ALD cycles.

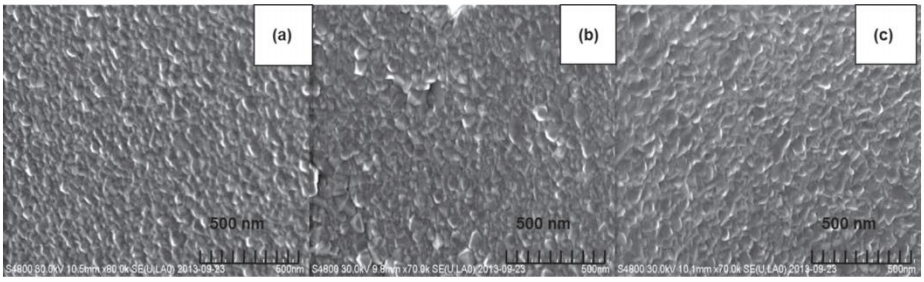

Figure 28. SEM of TiO_2 films on porous substrates with different numbers of ALD-cycles: (a) 500 cycles, (b) 1000 cycles, (c) 1500 cycles.

In addition to above mentioned characterization methods for TiO_2 catalytic thin films deposited on porous substrates, UV-visible transmittance spectroscopy was performed in the wavelength range 200–600 nm to show that the UV radiation can also activate the internal surfaces of coated porous substrates. Figure 29 clearly showed that UV radiation in the range of 350-389 nm can penetrate coated porous glass with 1 mm thickness.

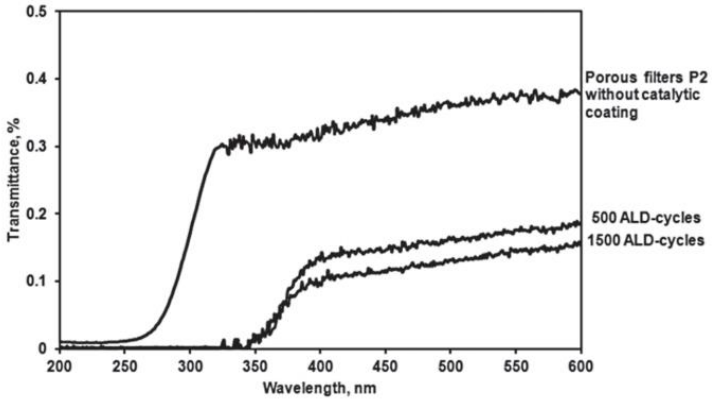

Figure 29. UV-Vis transmission spectra of uncoated porous glass substrate, and 500 and 1500 ALD-cycles of TiO_2 films deposited on porous glass.

6.1.3 Application of TiO_2 for toluene decomposition in DBD reactor

Toluene decomposition was recorded with on-line FTIR using TiO_2 catalyst coated on porous discs together with the DBD reactor. When the toluene concentration of 2450 ppm was stable, the plasma was turned on with applied specific input energy (SIE) values of 144, 240 and 336 J/l. Figure 30 shows that the concentration of toluene reduced in the exhaust from the reactor but at the same time signals of CO and CO_2 increased. In addition to the major reaction products, FTIR can also monitor reaction intermediates such as benzaldehyde and benzoic acid, which can be generated during toluene oxidation in the plasma (Figure 31). Those can influence the durability of catalysts, since they can accumulate on catalytically active sites. In addition, nitrogen oxides (NO_x) can be formed in the ambient air.

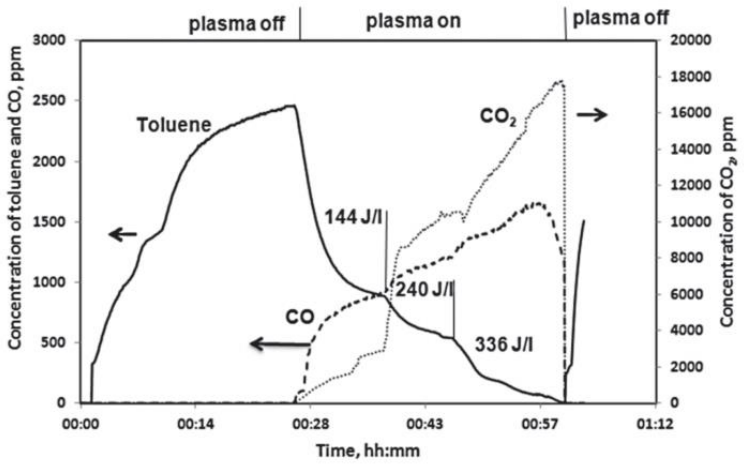

Figure 30. Toluene decomposition using TiO_2 catalyst with 1000 ALD cycles. SIEs are 144, 240 and 336 J/l.

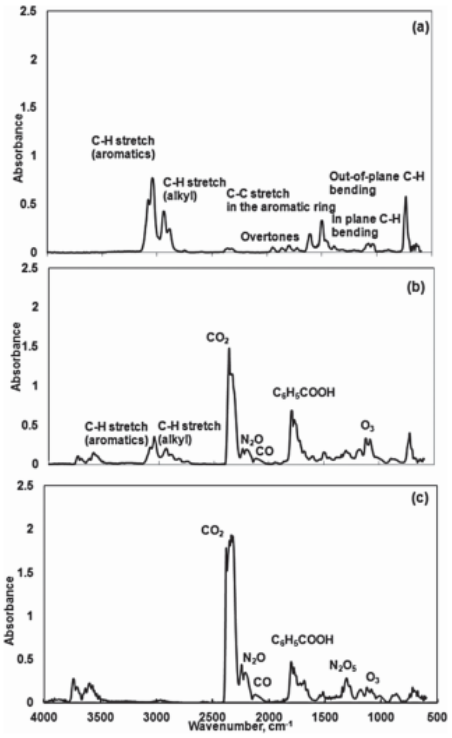

Figure 31. FTIR spectra of reaction by-products in the DBD reactor: (a) 0 J/l, (b) 336 J/l with uncoated porous glass supports and (c) 336 J/l with 1000 ALD-cycles of TiO_2 catalysts on porous glass supports.

Porous filters without any coatings were less effective and decomposed ~ 45% of toluene at SIE of 336 J/l (Figure 32). TiO_2 prepared with 500 cycles showed 75% decomposition of the toluene. It is worth noting that TiO_2 prepared with 1000 cycles coating showed the best performance and decomposed 100% of the toluene at SIE of 336 J/l compared with 1500 cycles. It can be define by a difference between the crystal phases of 500, 1000 and 1500 cycles of TiO_2. It was noted in previous reports [160,97,161] that the thicker TiO_2 films have a tendency to convert to the rutile phase, which is less catalytically active. The carbon balance was also higher with 1000 cycles (100%) and 1500 cycles (~ 97%) as compared to 500 cycles (43%) and non-covered filters (26%). The selectivity to CO_2 for uncoated filters, 500, 1000 and 1500 cycles of TiO_2 was 17%, 35%, 86% and 93%, respectively.

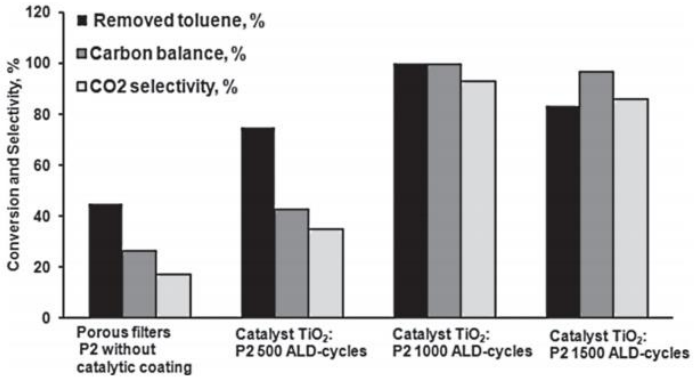

Figure 32. Activity of uncoated porous filters and TiO_2 coated filters with 500, 1000, 1500 ALD cycles during the destruction of 2450 ppm of toluene at SIE of 336 J/l.

6.2 ALD synthesis of CeO_2, Ag_2O and Ag-doped CeO_2 catalysts and their use for soot oxidation

6.2.1 CeO_2 catalyst grown by ALD

Cerium oxide was deposited at a temperature range of 180-350°C and the surface morphology was studied with SEM and AFM analysis, which showed that crystalline clusters were growing larger with increase of the deposition temperature. In addition to that, the shape of crystallites transformed from spherical to more facetted over the deposition temperature range (Figures 33 and 34).

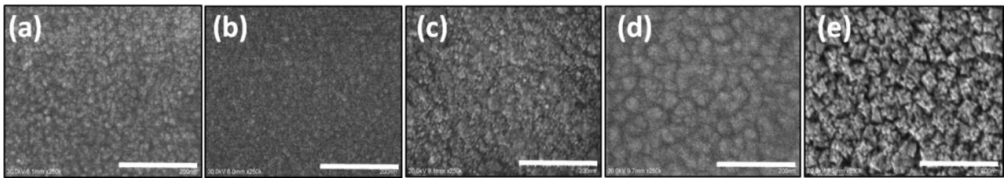

Figure 33. SEM images of cerium oxide coated silicon wafers deposited with 2000 cycles at temperatures of (a) 180 °C, (b) 200 °C, (c) 250 °C, (d) 300 °C, and (e) 350 °C. All scale bars are 200 nm.

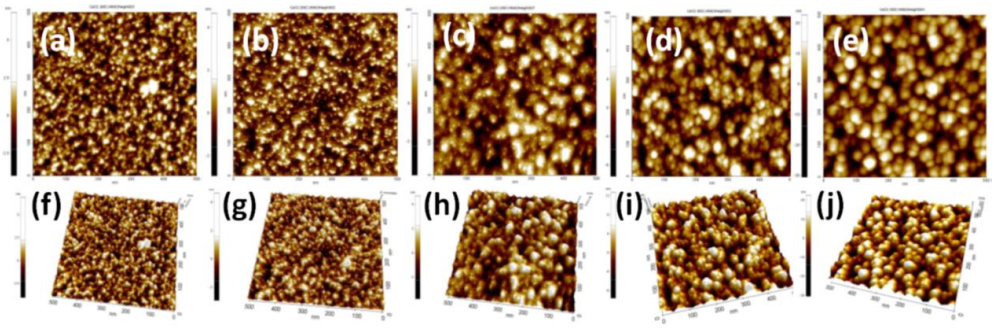

Figure 34. AFM images of cerium oxide deposited on silicon wafers with 2000 cycles at temperatures of [(a) and (f)] 180 °C, [(b) and (g)] 200 °C, [(c) and (h)] 250 °C, [(d) and (i)] 300 °C, and [(e) and (j)] 350 °C deposition temperatures. All scans are 0.5x0.5 µm.

The crystal structure of CeO_2 catalytic films was studied with XRD (Figure 35). The analysis showed that the films were polycrystalline with diffraction peaks attributed to the cubic fluorite structure of cerium oxide. The deposition temperature had a strong effect on the broadening and relative intensities of cerium oxide peaks due to the change of grain size and orientation, respectively. The grain sizes measured with AFM were between 10 nm and 20 nm up to 250°C deposition temperature. These results are in a good agreement with that calculated by Scherrer's equation from the reflections of (111) and (200) planes up to 250 °C deposition temperature. The interesting observation was noticed at 300 °C deposition temperature when the size of individual crystallites calculated with Scherrer's equation were smaller than that measured by AFM. It can be explained that AFM topography showed clusters of small multifacetted crystallites, which can give an increase in surface area and an enhancement in catalytic performance.

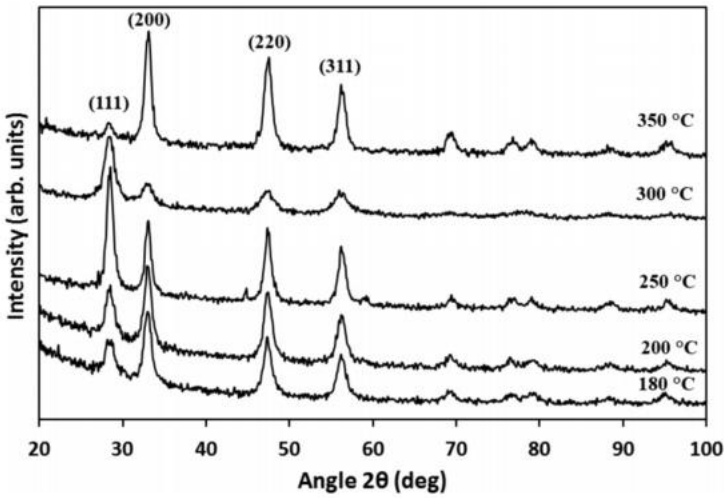

Figure 35. XRD patterns of cerium oxide films deposited with 2000 ALD cycles at 350, 300, 250, 200, and 180 ˚C.

The surface composition of CeO_2 catalytic thin films was analyzed with XPS, which showed the existence of two oxidation states of Ce^{4+} and Ce^{3+} in the film. The atomic proportions of Ce, O and C are summarized in Table 6. The XPS carbon data were obtained after removing the surface layer of the thin film by sputtering with Ar^+ ions. The atomic ratio of O/Ce showed that films primarily consist of CeO_2 with around 21 at. % of carbon impurities originating from the cerium precursor. A higher level of carbon incorporation was noted for CeO_2 deposited at 350 °C, which was above the ALD window.

The Ce 3d XPS spectra of CeO_2 deposited at different temperatures was deconvoluted and assigned to ten peaks, where U and V refer to the 3d3/2 and 3d5/2 spin–orbit components, respectively. In addition, U, U'', U''', V, V'', and V''' refer to Ce^{4+} final state, while U_0, U' and V_0, V' refer to Ce^{3+} final state. Shyu [162] proposed a method for the quantitative determinations of Ce^{3+} and Ce^{4+} concentrations, in which peak areas (A) of Ce^{4+} and Ce^{3+} components are used to estimate their relative concentrations in the films using the following equations:

$$Ce^{+3}(\%) = \frac{Ce^{3+}}{Ce^{3+}+Ce^{4+}} = \frac{A_{V_0}+A_{U_0}+A_{V'}+A_{U'}}{A_{V_0}+A_{U_0}+A_{V'}+A_{U'}+A_V+A_U+A_{V''}+A_{U''}+A_{V'''}+A_{U'''}} \times 100 \quad \text{(Eq. 7)}$$

The fraction of CeO_2 can be calculated by

$$Ce^{4+}(\%) = 100\% - Ce^{3+}(\%) \quad \text{(Eq. 8)}$$

Based on above-mentioned equations, Ce^{3+} and Ce^{4+} concentrations were estimated and summarized in Table 6. The amount of Ce^{3+} was higher (about 17.4%) in the film deposited at 300 °C in comparison to the films deposited at lower temperatures and can be explained by the reduction of Ce^{4+} with carbon originating from precursor decomposition. As XRD identified only CeO_2, we may assume that Ce_2O_3 exists in an amorphous phase that XRD cannot detect it. At the same time, the XRD pattern showed that CeO_2 films deposited at 300 °C had smaller grain size and broader XRD peaks. This can be explained by the growth of amorphous Ce_2O_3 at the grain boundaries, which in this case limits the growth of crystals.

Table 6. Surface elemental composition of cerium oxide films deposited with 2000 ALD cycles at 180, 200, 250, 300 and 350 °C.

Deposition temperature, °C	Surface composition (at.%)					Concentration of Ce^{4+}, at.% (excluding C)	Concentration of Ce^{3+}, at. % (excluding C)
	Ce3d	O1s	C1s	O/Ce (from survey)	O/Ce (Eq. 4 Paper III)		
180	25.7	53.2	21.1	2.1	1.94	87.2	12.8
200	25.9	52.9	21.3	2.0	1.94	87.1	12.9
250	26.7	52.1	21.2	2.0	1.93	86.9	13.1
300	24.8	50.3	20.2	2.0	1.91	82.6	17.4
350	23.5	49.7	26.9	2.1	1.90	79.7	20.3

6.2.2 Ag_2O and Ag-doped CeO_2 catalysts grown by ALD

Firstly, a silver oxide ALD process was established which found a self-limiting growth regime at 200 °C deposition temperature with GPC of 0.28 Å/cycle. This deposition temperature was chosen to avoid Ag_2O decomposition, which can happen above 200°C, and to match the deposition temperature of CeO_2. The growth mechanism of Ag_2O and the film morphology were studied with SEM (Figure 36). The nucleation region of Ag_2O occurs over 100 cycles, where Ag_2O films grow by the Volmer–Weber (VW) mechanism with further formation of islands or clusters.

CeO_2 films were doped with different Ag concentrations by ALD for the improvement of the catalytic properties. The surface morphology of Ag doped CeO_2 was studied with AFM and SEM. AFM results (Figure 37) showed that the nanocrystallites form nano-size clusters, whose size dramatically increases with the increase of Ag concentration in the CeO_2 films. We can assume that Ag prevents CeO_2 growth so that the Ag precursor reacts with previously deposited Ag layer more easily than with CeO_2 and therefore can form larger crystals/clusters of about 50 nm in size. The same behavior was observed on pure Ag_2O with 100 cycles. With decreasing of Ag doping concentration in CeO_2, no crystals/clusters larger than 25 nm were noticed.

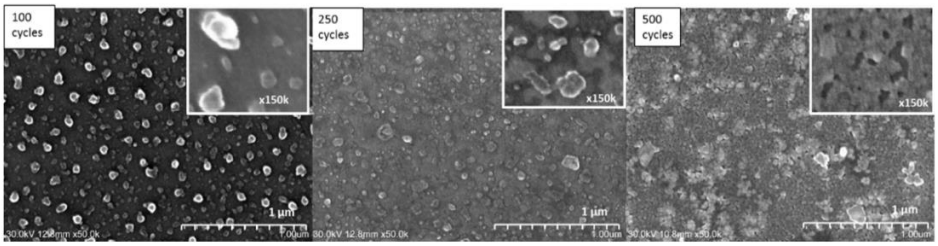

Figure 36. SEM images of Ag_2O thin films deposited with different number of cycles at 200 °C resulting in different thicknesses (5.8, 8.8, and 13.8 nm)

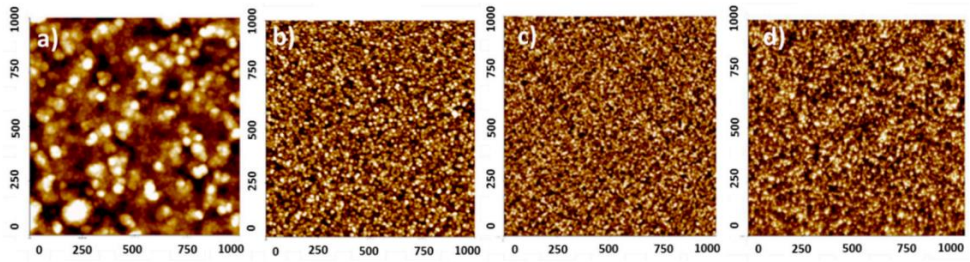

Figure 37. The AFM non-contact mode images of Ag doped CeO_2 in different CeO_2:Ag ratios deposited at 200 °C: (a) 10:1; (b) 20:1; (c) 30:1; and (d) CeO2. The scales are in nm.

Figure 38 illustrates the XRD patterns of Ag_2O, CeO_2 and Ag-doped CeO_2 thin films. For the case of a pure Ag_2O thin film, the crystalline phase is mostly the cubic phase. For Ag-doped CeO_2 in the ratio CeO_2:Ag 10:1, a small peak from the Ag_2O (200) plane was observed. The XRD analysis of Ag-doped CeO_2 samples demonstrated that the intensity and the shape of the

reflections of (111) and (200) planes of CeO_2 decreased and broadened, respectively, with increasing Ag doping concentration. This behavior relates to the deformation in the lattice structure of CeO_2 due to the presence of Ag dopant, which can cause the decreasing size of crystallites. On the other hand, the Ag^+ ion radius is larger than Ce^{4+} and no shift of CeO_2 planes was noticed from XRD patterns of Ag-doped CeO_2 thin films. Therefore, we can assume that Ag dopant grows as metal oxide and prevents the formation of CeO_2 crystallites.

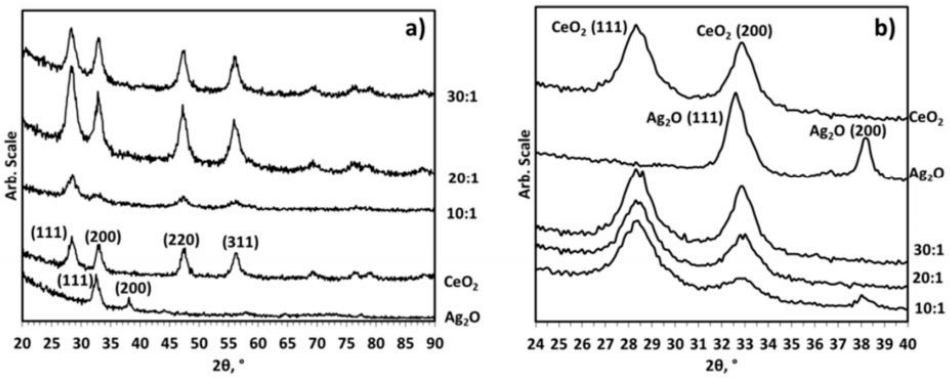

Figure 38. (a) X-ray diffraction (XRD) patterns of Ag_2O, CeO_2 and Ag doped CeO_2 with different Ce:Ag ratios 10:1, 20:1, and 30:1 deposited at 200 °C. (b) XRD patterns of slow scans of CeO_2, Ag_2O and Ag doped CeO_2 with different Ce:Ag ratios of 10:1, 20:1, and 30:1 in the 2θ range of 24°–40°.

The results from XPS spectra showed that the pure Ag_2O films had only one peak at 368.2 eV, which consists of the dominant oxidation state of Ag^+. In Ag doped CeO_2 films each Ag 3d level can be deconvoluted into three compounds of Ag^+ , Ag^0 , and Ag^{2+} (Table 7). It was noticed that with increasing the amount of Ag dopant, the concentration of Ag^+ species increased notably. Apparently, the silver oxide is reduced by CeO_2 at lower doping concentration. Sadanandam et al. [163] reported a similar reduction effect on silver in Ag_2O-doped TiO_2. In addition to that, stoichiometric CeO_2 can also be reduced to Ce^{3+} during Ag doping. This results in the stabilization of the Ag in the +1 oxidation state, which is in a good agreement with the published literature [164,165,166].

Table 7. Binding energies and integrated peak areas of Ag 3d spin-orbit doublets in Ag_2O, Ag doped CeO_2 and CeO_2 thin films.

Catalyst	Compound (BE, eV)			Concentration of Ce^{4+} (at.%) (Excluding C)	Concentration of Ce^{3+} (at.%) (Excluding C)	Ce^{3+}/Ce^{4+} (%)
	Ag^+ (368.2±0.1)	Ag^0 (369.2±0.1)	Ag^{2+} (367.2)			
Ag_2O	100	-	-	-	-	-
Ce:Ag 10:1	85	9.7	4.5	77	23	29.8
Ce:Ag 20:1	59	35	6	80	20	25.0
Ce:Ag 30:1	38.4	59	2.6	82	18	21.9
CeO_2	-	-	-	83	17	20.4

6.2.3 Application of CeO_2, Ag_2O and Ag-doped CeO_2 catalyst in diesel soot combustion

The soot conversion was defined as:

$$C(\%) = \frac{M_0 - M}{M_0} \times 100\% \quad (6.2)$$

where is M_0 is the initial soot mass, and M is the amount of soot left on the catalyst after burning by heating up to a given T value. Both values were obtained after weighing of samples before and after the annealing test.

Figures 39 and 41 show the dependence of the soot conversion versus the annealing temperature with the application of catalytic materials and with reference samples. All catalytic thin films started to combust soot with increasing annealing temperature far more than the reference samples without any coatings. From Figure 39 can be seen that CeO_2 films deposited at 300 °C showed the highest catalytic efficiency and decomposed 100% of soot at 450 °C. AFM measurements showed that CeO_2 deposited at 300 °C had a higher roughness in a comparison with films deposited at lower temperatures. Therefore, we can assume that these catalytic films had a higher surface area, providing more space for catalytic reactions. Another explanation can be related to the formation and regeneration of the Ce^{4+}/Ce^{3+} redox pair. XPS results presented above illustrated that CeO_2 deposited at 300 °C had slightly higher concentration of Ce^{3+}, promoting the increase of active oxygen species. For a better illustration of soot oxidation over CeO_2 catalysts deposited on stainless steel foil, the photos were taken and presented in Figure 40. CeO_2 catalysts deposited at 300 °C oxidized soot completely when rest of samples had a residual soot after annealing at 430 °C for 4 hours.

The Ag-doped CeO_2 catalytic films deposited at 200 °C showed lowered soot combustion temperature, especially CeO_2:Ag 10:1 catalyst (Figure 41). It oxidized 100% of soot at 390 °C. The catalysts with lower silver doping concentration of CeO_2:Ag 20:1 and 30:1 achieved 100% soot oxidation at higher annealing temperature of 490 °C. Zou et al. [167] proposed the mechanism when silver oxide decomposed and released oxygen, which migrates to soot surfaces to form carbon–oxygen intermediates. At the same time, the adsorbed oxygen on the silver facilitates the redox reaction and more active oxygen species are formed. In addition to that explanation, CeO_2:Ag 10:1 contains the highest concentration of Ce^{3+}, which can also form more oxygen vacancies. However, CeO_2:Ag 10:1 catalyst lost 10% of its activity in the third trial, whereas further trials showed stable results with 90% oxidized soot. We can assume that CeO_2 facilitates stabilization of Ag ions in the doped films and these catalysts remain stable after repeated tests. The catalysts with lower Ag concentration such as CeO_2:Ag 20:1, 30:1 and also pure CeO_2 did not lose activity during durability tests.

Although the pure Ag_2O catalytic films (Figure 41) showed one of the lowest 100% soot oxidation temperatures at 410 °C, it lost its catalytic activity after the first trial. The use of Ag_2O catalyst in further trials leads to film decomposition and total loss of catalytic properties. Because of this, pure Ag_2O thin films cannot be used as catalysts at temperature higher than 300°C.

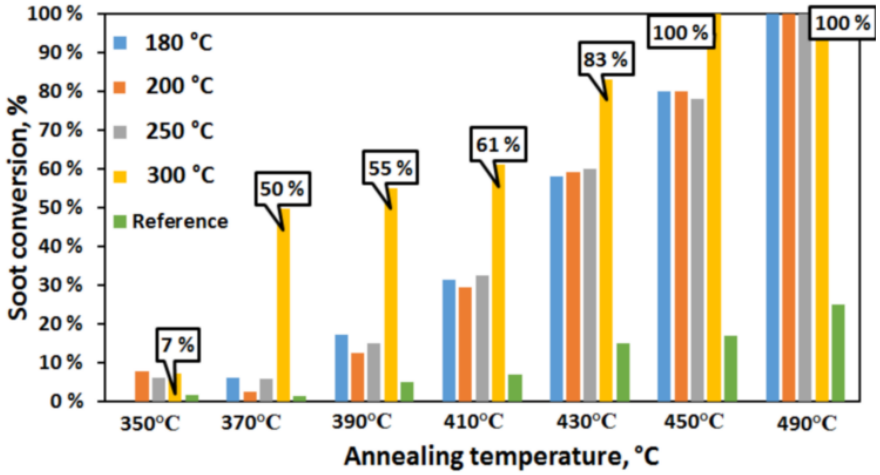

Figure 39. Conversion of oxidized soot by cerium oxide thin films deposited on stainless steel foil at 180, 200, 250 and 300 °C vs. annealing temperature during 4 hours. The measurement uncertainty is approximately 5%.

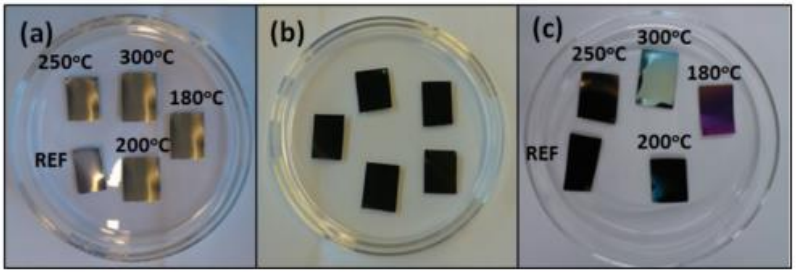

Figure 40. Annealing of soot on CeO_2 catalysts deposited at 180, 200, 150 and 300°C with 2000 ALD cycles on stainless steel foil: (a) after CeO_2 ALD coating, (b) covered by soot, (c) after annealing test at 430 °C for 4 hours.

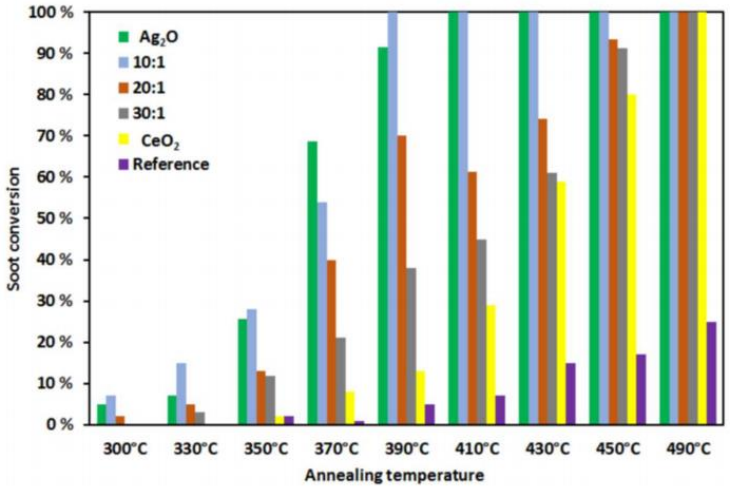

Figure 41. Conversion of oxidized soot on silver oxide, cerium oxide, and silver doped cerium oxide in ratio CeO_2 :Ag 10:1, 20:1, 30:1 thin films deposited on stainless steel foil at 200 °C vs. annealing temperature over 2 h. The measurement uncertainty is approximately 5%.

Summarizing the above described catalysts for soot oxidation, the characteristic temperatures of all catalysts are combined in Table 8. The catalysts with the lowest initiated temperature (T_i) and final temperature (T_f) were CeO_2:Ag 10:1 and bare Ag_2O. However, CeO_2:Ag 10:1 catalysts showed very good durability during repetitive trials, whereas the catalytic performance of bare Ag_2O significantly decreased.

Table 8. T_i and T_f of soot oxidation by CeO_2 and Ag-doped CeO_2 catalysts

Catalyst	T_i, °C	T_f, °C
None	410	600
CeO_2 180°C	350	490
CeO_2 200°C	350	490
CeO_2 250°C	350	490
CeO_2 300°C	350	450
CeO_2:Ag 10:1	300	390
CeO_2:Ag 20:1	300	490
CeO_2:Ag 30:1	330	490
Ag_2O	300	410

7 Conclusion and further research

The aim of this work was the development of catalysts for environmental protection. The focus was placed on the deposition of TiO_2 catalyst by ALD in combination with DBD for toluene decomposition and on the deposition of CeO_2, Ag_2O and Ag-doped CeO_2 catalysts by ALD for diesel soot combustion. Based on the results discussed in this thesis and the appended publications, the following conclusions can be drawn:

- The nucleation regime and growth of TiO_2 thin films deposited by ALD at 350 °C were studied on planar silicon substrates. The results showed that 50 cycles are required to start growing a continuous TiO_2 film on untreated silicon substrates and 80 cycles are needed for plasma treated silicon. The quantum confinement effect on optical bandgap can be used for the evaluation of the size of individual crystallites formed on silicon, and these results are compatible with AFM measurements. The ellipsometric modelling showed that the initial crystallite density of $\sim 3 \times 10^{17}$ m^{-3} decreases to $\sim 3 \times 10^{15}$ m^{-3} at the point where a continuous film is formed and can be explained by a process of Ostwald ripening. If the ripening process is taken into account, the growth rate of continues TiO_2 film is in a good agreement with the growth rate of crystallites calculated from the QC.

- TiO_2 thin films were successfully deposited on porous glass substrates by ALD at 350 °C and applied as photocatalyst in the DBD plasma for toluene removal. The presence of the anatase crystal phase of TiO_2 was observed to be the most critical factor in obtaining a highly active TiO_2 photocatalyst. The highest performance of 100% toluene removal with SIE of 336 J/l was observed with a thickness of 22 nm of TiO_2, which corresponds to 1000 ALD cycles. Further increase of TiO_2 thickness up to 1500 cycles on porous substrates showed the formation of tiny rutile reflection, which slightly decreased the photocatalytic properties. The major products of toluene decomposition were CO and CO_2 and no carbon ring-containing by-products were noted.

- CeO_2 thin films were deposited by ALD in the temperature range 180-350 °C and applied as catalysts for soot oxidation under loose contact mode. With an increase in the substrate temperature up to 300°C, the (111) reflection becomes dominant. The different deposition temperatures affect the broadening and the relative intensities of the various XRD peaks due to the variation of grain size and orientation, respectively. The smaller crystal size of CeO_2 catalyst deposited at 300°C together with comparatively large crystallite cluster size will result in clusters with multifaceted surfaces giving a larger surface area. This may play a part in enhancing catalytic activity. In addition, an increase in the concentration of Ce^{+3} species may increase oxygen vacancies. These film properties may effect on carbon oxidation behavior. It was found that the cerium oxide deposited at 300°C decomposed 100% of soot at annealing temperature of 450 °C, while CeO_2 deposited at lower temperatures required 490°C to oxidize 100% of the soot.

- Ag_2O thin films were successfully deposited by ALD at 200 °C with GPC of 0.28 Å/cycle and were applied as catalysts for soot oxidation. Ag_2O catalysts effectively promoted 100% soot oxidation at T_f = 410 °C for the first test. However, the second test

showed a decrease of 50% in Ag_2O catalytic performance. The performance continued to decrease with further tests.

- ALD was used for the preparation of Ag doped CeO_2 catalysts and the silver doping concentration was finely tuned by setting the CeO_2:Ag cycle ratio to 10:1, 20:1, and 30:1 at 200 ˚C. These catalysts were also tested for soot combustion applications. The GPC of Ag doped CeO_2 decreased from 0.32 Å/cycles down to 0.21 Å/cycles with increasing silver concentration. It can be explained that Ag nucleates more easily on the top of previous Ag layer than on CeO_2 and forms larger clusters, which were observed with SEM and AFM analysis on CeO_2:Ag 10:1. In addition, XRD and XPS analyses showed that the Ag^+ oxidation state dominated for CeO_2:Ag catalysts in the ratio of 10:1 and stoichiometric CeO_2 tended to be reduced from Ce^{4+} to Ce^{3+} ions. The soot annealing test showed 100% soot oxidation at T_f = 390 ˚C for samples with higher concentration of Ag^+, that is in CeO_2:Ag 10:1 catalytic films. The good performance can be explained by promotion of oxygen species from Ag^+ sites and the higher concentration of Ce^{3+} in the CeO_2:Ag 10:1 catalyst films. The Ag doped CeO_2 catalysts showed stable performance after durability tests.

Future research could focus on the development of doped TiO_2 and CeO_2 catalytic materials by other elements for improving the desirable properties of activity and durability. The challenge is to find the efficient low cost non-toxic catalytic materials, which can decrease the temperature and time needed for pollutant decomposition. Therefore, more research work should be done in order to acquire the fundamental knowledge of the properties of new materials. In addition, an accurate analytical methods such as temperature programmed oxidation (TPO) analysis could be applied for more extensive investigation of catalysts behavior.

References

1. R. E. Morabet, “Effects of Outdoor Air Pollution on Human Health”, in the book: *Reference Module in Earth Systems and Environmental Sciences*, 2018.

2. B. J. O’Neill, D. H. K. Jackson, J. Lee, C. Canlas, P. C. Stair, C. L. Marshal, J. W. Elam, T.F. Kuech, J. A. Dumesic, and G. W. Huber, “Catalyst Design with Atomic Layer Deposition”, *ACS Catalysis*, vol. 5 (3), pp 1804–1825, 2015.

3. T. Oda, “Non-thermal plasma processing for environmental protection: decomposition of dilute VOCs in air”, *Journal of Electrostatics* vol. 57, pp. 293-311, 2003.

4. R. Brandenburg, V. V. Kovacevic, M. Schmidt, R. Basner, M. Kettlitz, G. B. Sretenovic, B. M. Obradovic, M. M. Kuraica, and K.-D. Weltmann,” Plasma-Based Pollutant Degradation in Gas Streams: Status, Examples and Outlook”, *Contributions to Plasma Physics* . vol. 54, pp. 202-214, 2014.

5. H. Huang, D. Ye, “Combination of photocatalysis downstream the non-thermal plasma reactor for oxidation of gas-phase toluene”, *Journal of Hazardous Materials* vol. 171(1-3), pp. 535-541, 2009.

6. W. A. Majewski, M.K. Khair, “Diesel Emissions and Their Control”, SAE International, Warrendale, PA, 2006.

7. M. Primet, E. Garbowski, in “Catalysis by Ceria and Related Materials”, ed. A. Trovarelli, Imperial College Press, London, pp. 407-429, 2002

8. S. Liu, X. Wu, W. Liu, W. Chen, R. Ran, M. Li, D. Weng, “Soot oxidation over CeO2 and Ag/CeO2: Factors determining the catalyst activity and stability during reaction”, *Journal of Catalysis*, vol. 337, pp. 188-198, 2016.

9. M. Ritala, M. Leskelä, in: H.S. Nalwa (Ed.), Handbook of Thin Film Materials, vol. 1, Academic Press, New York, p. 103, 2002.

10. R.L. Puurunen et al., “On the Early History of ALD: Molecular Layering”, 14th International Conference on Atomic Layer Deposition, Kyoto, Japan, 2014.

11. V.B. Aleskovskii, S. I. Koltsov, “Some characteristics of molecular layering reactions”, Abstract of Scientific and Technical Conference, Goskhimizdat, Leningrad 67, 1965.

12. G.V. Sveshnikova, S. I. Koltsov, V. B. Aleskovskii, “Formation of a silica layer of predetermined thickness on silicon by the molecular-layering method”, *Russian Journal of Applied Chemistry* ., USSR, 43, pp. 1155-1157 in English, 1970.

13. T. Suntola and J. Antson, U.S. Patent No. 4,058,430 15 November 1977

14. T. Suntola, “Atomic layer epitaxy”, *Materials Science Reports*4, pp. 261-312, 1989.

15. T. Suntola, “Handbook of Thin Film Process Technology”, edited by D.A. Glocker and S. I. Shah, IOP, Bristol, United Kingdom, 1995

16. T. Suntola and J.Antson, Finland Patent No. 52,359 10 September 1977

17. R.L. Puurunen, “Surface chemistry of atomic layer deposition: A case study for the trimethylaluminum/water process”, *Journal of Applied Physics*97, 121301, 2005.

18. www.transparencymarketresearch.com/ global-refinery-catalyst-market.html (accessed on January 2, 2018)

19. Freedonia Group. World Catalysts, 2018, www.freedoniagroup. com/world-catalysts.html (accessed on January 2, 2018).

20. G. Ertl, G.; Knözinger, H.; Schüth, F.; Weitkamp, J. (Eds.) “Handbook of Heterogeneous Catalysis”, 2nd ed.; Wiley-VCH: Weinheim, Germany, 2008.

21. J.T. Wrobleski, M. Boudart, “Preparation of solid catalysts: an appraisal”, *Catalysis Today* vol. 15(3–4), pp. 349–60, 1992

22. T.J. Schwartz, B.J. O’Neill, B.H. Shanks, J.A. Dumesic, “Bridging the chemical and biological catalysis gap: challenges and outlooks for producing sustainable chemicals”, *ACS Catalysis* vol. 4(6), pp. 2060–69, 2014

23. S.L. Wegener, T. J. Marks, P.C. Stair, “Design strategies for the molecular level synthesis of supported catalysts”, *Accounts of Chemical Research* vol. 45(2), pp. 206–14, 2012

24. C. Detavernier, J. Dendooven, S.P. Sree, K.F. Ludwig, J.A. Martens, “Tailoring nanoporous materials by atomic layer deposition”, *Chemical Society Review*s vol. 40(11), pp. 5242–53, 2011

25. P. Munnik, P.E. de Jongh, K.P. de Jong, “Recent developments in the synthesis of supported catalysts”, *Chemical Reviews* vol. 115(14), pp. 6687–718, 2015

26. J. Lu, J.W. Elam, P.C. Stair, “Atomic layer deposition—sequential self-limiting surface reactions for advanced catalyst “bottom-up” synthesis”, Surface Science Reports . vol. 71(2), pp. 410–72, 2016

27. J. Dendooven, “Atomic Layer Deposition in Nanoporous Catalyst Materials” in Atomically-Precise Methods for Synthesis of Solid Catalysts, editors: S. Hermans, T. Visart de Bocarme chap.7, pp. 167–197, 2014.

28. J.C. Védrine (Ed.), “Heterogeneous Catalysis by Metal Oxides”; Elsevier: Amsterdam, The Netherlands, 2018

29. L.F. Liotta, “Catalytic oxidation of volatile organic compounds on supported noble metals”, *Applied Catalysis B: Environmental vol.* 100, pp. 403-412, 2010.

30. W. B. Li, J. X. Wang, H. Gong, “Catalytic combustion of VOCs on non-noble metal catalysts”, *Catalysis. Today*, vol. 148, pp. 81-87, 2009

31. A. M. Vandenbroucke, R. Morent, N. D. Geyter, and C. Leys, “Non-thermal plasmas for non-catalytic and catalytic VOC abatement”, *Journal of Hazardous Materials* vol. 195, pp. 30-54, 2011.

32. G. Xiao, W. Xu, R. Wu, M. Ni, C. Du, X. Gao, Z. Luo, K. Cen. “Non-Thermal Plasmas for VOCs Abatement”, *Plasma Chemistry and Plasma Processing* vol. 34, pp.1033-1065, 2014.

33. M. Bahri, F. Haghighat, “Plasma-Based Indoor Air Cleaning Technologies: The State of the Art-Review”, *Clean Soil Air Water* vol. 42, pp. 1667-1680, 2014

34. Y. S. Mok, D.H. Kim, “Treatment of toluene by using adsorption and nonthermal plasma oxidation process”, *Current Applied Physics* vol. 11, pp. S58-S62, 2011

35. F. Holzer, U. Roland, F.D. Kopinke, “Combination of non-thermal plasma and heterogeneous catalysis for oxidation of volatile organic compounds. part 1. accessibility of the intra-particle volume”, *Applied Catalysis B: Environmental* vol. 38, pp. 163-181, 2002

36. H. H. Kim, S.-M. Oh, A. Ogata, and S. Futamura, “Decomposition of gas-phase benzene using plasma-driven catalyst (PDC) reactor packed with Ag/TiO2 catalyst”, *Applied Catalysis B: Environmental* vol. 56, pp. 213-220, 2005.

37. S. Sultana, A. M. Vandenbroucke, C. Leys, N. De Geyter and R. Morent, “Abatement of VOCs with Alternate Adsorption and Plasma-Assisted Regeneration: A Review”, Catalysts, vol. 5, pp. 718-746, 2015.

38. H.H. Kim, “Nonthermal Plasma Processing for Air-Pollution Control: A Historical Review, Current Issues, and Future Prospects”, *Plasma Processes and Polymers* . vol. 1, pp. 91–110, 2004

39. U. Konelschatz, B. Eliasson and W. Egli, “Dielectric-Barrier Discharges. Principle and Applications”, Journal de Physique IV Colloque 7, pp. C4-47-C4-66, 1997.

40. R. Brandenburg, “Dielectric barrier discharges: progress on plasma sources and on the understanding of regimes and single filaments”, *Plasma Sources Science and Technology* . vol. 27, p. 079501, 2018.

41. H. Zhang, K. Li, T. Sun, J. Jia, Z.Y. Lou, S. Yao, G. Wang, “The combination effect of dielectric barrier discharge (DBD) and TiO2 catalytic process on styrene removal and the analysis of the by-products and intermediates”, *Research on Chemical Intermediates*, vol. 41, p. 175–189, 2015.

42. T. E. Corporation, "Locating and estimating air emissions from soruces of toluene ", U. E. P. Agency, Ed., ed. Chapel Hill, North Carolina, p. 207, 1994

43. (2019, January). Market Study: Toluene. Available: http://www.ceresana.com/en/marketstudies/chemicals/toluene/

44. (2018). Toluene Uses and Market Data. Available: http://www.icis.com/resources/news/2007/11/07/9076550/toluene-uses-and-market-data/

45. A. f. T. S. a. D. R. (ATSDR), "Toxicological Profile for Toluene," D. o. H. a. H. Services, Ed., ed. Atlanta, GA: U.S. Public Health Service, U.S. Department of Health and Human Services, 2000.

46. T. Hobara, H. Kobayashi, E. Higashihara, T. Kawamoto, T. Sakai, "Acute effects of 1,1,1-trichloroethane, trichloroethylene, and toluene on the hematologic parameters in dogs", *Archives of Environmental Contamination and Toxicology* vol. 13(5), pp. 589-93, 1984.

47. R. Ramdas, E. Nowicka, R. Jenkins, D. Sellick, C. Davies, S. Golunski, "Using real particulate matter to evaluate combustion catalysts fordirect regeneration of diesel soot filters", *Applied Catalysis B: Environmental*, vol. 176–177, pp. 436-443, 2015.

48. I. A. Reşitoğlu, K. Altinişik, A. Keskin, " The pollutant emissions from diesel-engine vehicles and exhaust aftertreatment systems", *Clean Technologies and Environmental Policy*, Vol. 17(1), pp. 15–27, 2015.

49. Diesel Fuels Technical Review - Chevron Corporation, 2007, https://www.chevron.com/-/media/chevron/operations/documents/diesel-fuel-tech-review.pdf

50. B. Frank, R. Schlögl, D.S. Su, "Diesel soot toxification", *Environmental Science & Technology*, vol. 47, pp. 3026-3027, 2013.

51. https://www.dieselnet.com 2018

52. J.-O. Müller, B. Frank, R. E. Jentoft, R.Schlögl, D. S. Su, "The oxidation of soot particulate in the presence of NO2", *Catalysis Today*, vol. 191, pp. 106-111, 2012.

53. J.P.A. Neeft, M. Makkee, J.A. Moulijn, "Diesel particulate emission control", *Fuel Processing Technology*, vol. 47, issue 1, pp. 1-69, 1996.

54. H. Bockhorn (ed.), "Soot Formation in Combustion: Mechanisms and Models", Springer Verlag, Heidelberg, p.4, 1994.

55. J.P.A. Neeft, T.X. Nijhuis, E. Smakman, M. Makkee, J. Moulijn, "Kinetics of the Oxidation of Diesel Soot", *Fuel*, vol. 76, pp. 1129–1136, 1997.

56. N. Zouaoui, M. Labaki, M. Jeguirim, “Diesel soot oxidation by nitrogen dioxide, oxygen and water under engine exhaust conditions: Kinetics data related to the reaction mechanism” *Comptes Rendus Chimie*, vol. 17, pp. 672-680, 2014.

57. M. Jeguirim, V. Tschamber, P. Ehrburger, “Catalytic effect of platinum on the kinetics of carbon oxidation by NO2 and O2”, *Applied Catalysis B: Environmental*, vol. 76, pp. 235-240, 2007.

58. K. O. Lee, H. Seong, S. M. Choi, “Detailed analysis of kinetic reactions in soot oxidation by simulated diesel exhaust emissions”, *Proceedings of the Combustion Institute*, vol. 34, Issue 2, pp. 3057-3065, 2013.

59. J.L. Figueiredo, M.F.R. Pereira, M.M.A. Freitas, and J.J.M. Órfão, “Modification of the surface chemistry of activated carbons”, *Carbon*, vol.37, issue 9, pp. 1379-1389, 1999.

60. B.R. Stanmore, J.F. Brilhac, P. Gilot, “The oxidation of soot: a review of experiments, mechanisms and models”, *Carbon*, vol. 39, issue 15, pp. 2247- 2268, 2001

61. A. Bueno-López, “Diesel soot combustion ceria catalysts”, *Applied Catalysis B: Environmental* vol. 146, pp. 1-11, 2014.

62. A. Russell, W.S. Epling, “Diesel Oxidation Catalysts”, *Catalysis Reviews Science and Engineering*, vol. 53, pp. 337-423, 2011.

63. J. Oi-Uchisawa, A. Obuchi, S. Wang, T. Nanba, A. Ohi, “Catalytic performance of Pt/MOx loaded over SiC-DPF for soot oxidation”, *Applied Catalysis B: Environmental*, vol. 43, pp. 117-129, 2003.

64. C.A. Neyertz, E.D. Banus, E.E. Miró, C.A. Querini, “Potassium-promoted Ce0.65Zr0.35O2 monolithic catalysts for diesel soot combustion”, *Chemical Engineering Journal.*, vol. 248, pp. 394-405, 2014.

65. R. Prasad, V.R. Bella, “A review on Diesel Soot Emission, its Effect and Control”, *Bulletin of Chemical Reaction Engineering & Catalysis*, vol. 5, issue 2, pp. 69-86, 2010.

66. J.P.A. Neeft, M. Makkee, J.A. Moulijn, “Catalysts for the oxidation of soot from diesel exhaust gases. I. An exploratory study”, *Applied Catalysis B: Environmental*, vol. 8, issue 1, pp. 57-78, 1996.

67. J.P.A. Neeft, M. Makkee, J.A. Moulijn, ”Metal oxides as catalysts for the oxidation of soot”, *The Chemical Engineering Journal*, vol. 64, issue 2, pp. 295-302, 1996.

68. M. Piumetti, S. Bensaid, N. Russo, D. Fino, “Nanostructured ceria-based catalysts for soot combustion: Investigations on the surface sensitivity”, *Applied Catalysis B: Environmental*, vol. 165, pp. 742-751, 2015.

69. B.A.A.L. van Setten, J.M. Schouten, M. Makkee, J.A. Moulijn, ”Realistic contact for soot with an oxidation catalyst for laboratory studies”, *Applied Catalysis B: Environmental*, vol. 28, issue 3-4, pp. 253-257, 2000.

70. N. Labhsetwar, R.B. Biniwale, R. Kumar, S. Devotta, "Application of supported perovskite-type catalysts for vehicular emission control", Catalysis Surveys from Asia, vol. 10, pp. 55-64, 2006

71. E. Aneggi, C. de Leitenburg, A. Trovarelli A. Trovarelli, P. Fornasiero (Eds.), Catalysis by Ceria and Related Materials (2nd ed.), Imperial College Press, London), pp. 565-621, 2013

72. E.S.J. Lox, G. Ertl, H. Knözinger, F. Schüth, J. Weitkamp (Eds.), Handbook of Heterogeneous Catalysis (2nd ed.), Wiley-VCH, Weinheim, pp. 2274-2344, 2008.

73. A. Bueno López, K. Krishna, M. Makkee, J.A. Moulijn, ”Active oxygen from CeO2 and its role in catalysed soot oxidation”, *Catalysis Letters*, vol. 99, pp. 203-205, 2005.

74. N. Labhsetwar, M. Dhakad, S.S. Rayalu, R. Kumar, J. Subrt, H. Haneda, S. Devotta, T. Mitsuhashi, “Thermally stable metal ruthenate based soot oxidation catalyst for diesel exhaust emission control”, *Topics in Catalysis*, vol. 42–43, pp. 299-302, 2007.

75. P. Doggali, H. Kusaba, S. Rayalu, Y. Teraoka, N. Labhsetwar, “Bench Scale Experiments of Diesel Soot Oxidation Using Pr0.7Sr0.2K0.1MnO3 Perovskite Type Catalyst Coated on Ceramic Foam Filters”, *Topics in Catalysis*, vol. 56, pp. 457-461, 2013.

76. J. Zhu, A. Thomas, “Perovskite-type mixed oxides as catalytic material for NO removal”, *Applied Catalysis B: Environmental*, vol. 92, pp. 225-233, 2009.

77. B.S. Sánchez, C.A. Querini, E.E. Miró, “NOx adsorption and diesel soot combustion over La2O3 supported catalysts containing K, Rh and Pt”, *Applied Catalysis A: General*, vol. 366, pp. 166-175, 2009.

78. N.E. Olong, K. Stöwe, W.F. Maier, “HT-search for alkaline- and noble-metal-free mixed oxide catalysts for soot oxidation”, *Catalysis Today*, vol. 137, pp. 110-118, 2008.

79. L. Castoldi, R. Matarrese, L. Lietti, P. Forzatti, “Intrinsic reactivity of alkaline and alkaline-earth metal oxide catalysts for oxidation of soot”, *Applied Catalysis B: Environmental*, vol. 90, pp. 278-285, 2009.

80. M. Dhakad, D. Fino, S.S. Rayalu, R. Kumar, A. Watanabe, H. Haneda, S. Devotta, T. Mitsuhashi, N. Labhsetwar, “Zirconia supported Ru-Co bimetallic catalysts for diesel soot oxidation”, *Topics in Catalysis*, vol.42-43, issue 1-4, pp. 273-276, 2007.

81. E. Aneggi, J. Llorca, C. de Leitenburg, G. Dolcetti, A. Trovarelli, “Soot combustion over silver-supported catalysts”, *Applied Catalysis B: Environmental*, vol. 91, issue 1-2, pp. 489-498, 2009.

82. I. Atribak, I. Such-Basánez, A. Bueno-López, A. García-García, “Comparison of the catalytic activity of MO2 (M = Ti, Zr, Ce) for soot oxidation under NOx/O2”, *Journal of Catalysis*, vol. 250, issue 1, pp. 75-84, 2007.

83. J. Oi-Uchisawa, A. Obuchi, Z. Zhao, S. Kushiyama, “Carbon oxidation with platinum supported catalysts”, *Applied Catalysis B: Environmental*, vol. 18, issue 3-4, pp. L183-L187, 1998.

84. H. Lin, Y. Li, W. Shangguan, Z. Huang, “Soot oxidation and NOx reduction over BaAl2O4 catalyst”, *Combustion and Flame*, vol.156, issue 1, pp. 2063-2070, 2009.

85. M. Fu, X. Yue, D. Ye, J. Oyang, B. Huang, J. Wu, H. Liang, “Soot oxidation via CuO doped CeO2 catalysts prepared using coprecipitation and citrate acid complex-combustion synthesis”, *Catalysis Today*, vol. 153, issue 3-4, pp. 125-132, 2010.

86. X. Wu, F. Lin, H. Xu, D. Weng, “Effects of adsorbed and gaseous NOx species on catalytic oxidation of diesel soot with MnOx-CeO2 mixed oxides”, *Applied Catalysis B: Environmental*, vol. 96, issue 1-2, pp. 101-109, 2010.

87. Q. Liang, X. Wu, D. Weng, Z. Lu, “Selective oxidation of soot over Cu doped ceria/ceria-zirconia catalysts”, *Catalysis Communications*, vol. 9, issue 2, p. 202-206, 2008.

88. X. Quan, S. Yang, X. Ruan, and H. Zhao, “Preparation of titania nanotubes and their environmental applications as electrode,” *Environmental Science & Technology*, vol. 39, no. 10, pp. 3770–3775, 2005

89. M.R. Hoffmann, S.T. Martin, W. Choi, D.W. Bahnemann, “Environmental Applications of Semiconductor Photocatalysis”, *Chemical Reviews*, vol. 95, pp. 69-96, 1995

90. A. L. Linsebigler, G. Q. Lu, and J. T. Yates, “Photocatalysis on TiO2 Surfaces: Principles, Mechanisms, and Selected Results”, *Journal of Chemical Reviews* vol. 95, pp. 735-758, 1995.

91. J. Herrmann, “Fundamentals and misconceptions in photocatalysis”, *Journal of Photochemistry and Photobiology A: Chemistry*, vol. 216, pp. 85-93, 2010.

92. A.W. Morawski, M. Janus, B. Tryba, M. Toyoda, T. Tsumura, M. Inagaki, “Carbon modified TiO2 photocatalysts for water purification”, *Polish Journal of Chemical Technology* vol. 11, pp. 46-50, 2009.

93. S. Auvinen, M. Alatalo, H. Haario, J.-P. Jalava, R.-J. Lamminmäki, “Size and shape dependence of the electronic and spectral properties in TiO2 nanoparticles”, *The Journal of Physical Chemistry C* vol. 115, pp. 8484–8493, 2011.

94. L. Lin, Y. Chai, B. Zhao, W. Wei, D. He1, B. He, Q. Tang “Photocatalytic oxidation for degradation of VOCs”, *Open Journal of Inorganic Chemistry* vol. 3, pp. 165-179, 2013.

95. M. Lazzeri, A. Vittadini, A. Selloni, ”Structure and energetics of stoichiometric TiO2 anatase surfaces”, *Physical Review B* vol. 63, p. 155409, 2001.

96. W. Hebenstreit, N. Ruzycki, G.S. Herman, Y. Gao, U. Diebold, “Scanning tunneling microscopy investigation of the TiO2 anatase (101) surface”, *Physical Review B* vol. 62, p. R16344, 2000

97. M.-L. Kääriäinen, T.O. Kääriäinen, D.C. Cameron, “Titanium dioxide thin films, their structure and its effect on their photoactivity and photocatalytic properties”, *Thin Solid Films* vol. 517, pp. 6666–6670, 2009.

98. M. Anpo, “Photocatalysis on titanium oxide catalysts: Approaches in achieving highly efficient reactions and realizing the use of visible light”, *Catalysis Surveys from Japan* vol. 1, pp. 169–179, 1997.

99. M. Ritala, M. Leskelä, E. Nykänen, P. Soininen, L. Niinistö, ” Growth of titanium dioxide thin films by atomic layer epitaxy”, *Thin Solid Films* vol. 225, p. 288, 1993.

100. M. Ritala, M. Leskelä, L. Niinistö, P. Haussalo, ” Titanium isopropoxide as a precursor in atomic layer epitaxy of titanium dioxide thin films”, *Chemistry of Materials* vol. 5, pp. 1174-1181, 1993.

101. J. Aarik, A. Aidla, T.Uustare, K. Kukli, V. Sammelselg, M. Ritala, M. Leskelä, “Atomic layer deposition of TiO2 thin films from TiI4 and H2O”, *Applied Surface Science*, vol. 193, pp. 277-286, 2002

102. K.S. Finnie, G. Triani, K.T. Short, D.R.G. Mitchell, D.J. Attard, J.R. Bartlett, C.J. Barbe, “Influence of Si(1 0 0) surface pretreatment on the morphology of TiO2 films grown by atomic layer deposition”, *Thin Solid Films* vol. 440, pp. 109-116, 2003.

103. R. Matero, A. Rahtu, and M. Ritala, “In Situ Quadrupole Mass Spectrometry and Quartz Crystal Microbalance Studies on the Atomic Layer Deposition of Titanium Dioxide from Titanium Tetrachloride and Water”, *Chemistry of Materials* vol. 13, pp. 4506-4511, 2001.

104. N. G. Kubala, C. A. Wolden, “Self-limiting growth of anatase TiO2: a comparison of two deposition techniques”, *Thin Solid Films* vol. 518, pp. 6733-6737, 2010.

105. V. Pore, T. Kivelä, M. Ritala, M. Leskelä, “Atomic layer deposition of photocatalytic TiO2 thin films from TiF4 and H2O”, *Dalton Transactions* vol.45, pp. 6467-74, 2008.

106. A. Niskanen, K. Arstila, M. Leskelä, M. Ritala, ” Radical Enhanced Atomic Layer Deposition of Titanium Dioxide”, *Chemical Vapor Deposition* vol. 13, pp. 152-157, 2007

107. Q. Xie, J. Musschoot, D. Deduytsche, R. L. Van Meirhaeghe, C. Detavernier, S.Van den Berghe, Y.-L. Jiang, G.-P. Ru, B.-Z. Li, X.-P. Qu, “Growth kinetics and crystallization behavior

of TiO2 films prepared by plasma enhanced atomic layer deposition", *Journal of The Electrochemical Society* vol. 155, pp. H688-H692, 2008.

108. T. M. Onn, R. Küngas, P. Fornasiero, K. Huang and R. J.Gorte, "Atomic Layer Deposition on Porous Materials: Problems with Conventional Approaches to Catalyst and Fuel Cell Electrode Preparation", *Inorganics* vol. 6, p. 34, 2018.

109. Y. Zhang, C. Guerra-Nuñez, I. Utke, J. Michler, M.D. Rossell, and R. Erni, "Understanding and Controlling Nucleation and Growth of TiO2 Deposited on Multiwalled Carbon Nanotubes by Atomic Layer Deposition", *The Journal of Physical Chemistry C*, vol. 119(6), pp. 3379–3387, 2015.

110. B.L. Abrams and J.P. Wilcoxon, "Nanosize semiconductors for photooxidation", *Critical Reviews in Solid State and Material Sciences* vol. 30, pp. 153-182, 2005.

111. X. Chen and S.S. Mao, "Titanium dioxide nanomaterials: synthesis, properties, modifications, and applications", *Chemical Reviews* vol. 107, pp. 2891-2959 , 2007

112. H. Tada, M. Tanaka, "Dependence of TiO2 photocatalytic activity upon its film thickness", *Langmuir* vol. 13, pp.360-364, 1997.

113. M. Tazawa, M. Okada, K. Yoshimura, I. Ikezawa, "Photo-catalytic heat mirror with a thick titanium dioxide layer", *Solar Energy Materials and Solar Cells*, vol. 84, pp. 159-170, 2004.

114. J. Aarik, A. Aidla, T. Uustare, V. Sammelselg, "Morphology and structure of TiO2 thin films grown by atomic layer deposition", *Journal of Crystal Growth*, vol. 148(3), pp. 268–275, 1995.

115. T. Luttrell, S. Halpegamage, J. Tao, A. Kramer, E. Sutter, M. Batzill, "Why is anatase a better photocatalyst than rutile? - Model studies on epitaxial TiO2 films", *Scientific Reports* vol. 4, p. 4043, 2014.

116. R.W. Johnson, A. Hultqvist, S.F. Bent, "A brief review of atomic layer deposition: from fundamentals to applications", *Materials Today*, vol. 17(5), pp. 236–46, 2014.

117. D.R. Lide (Editor), 'Handbook of Chemistry and Physics 84th Edition', CRC Press, 2003

118. L. Malavasi, C.A.J. Fisher, M.S. Islam, "Oxide-ion and proton conducting electrolyte materials for clean energy applications: structural and mechanistic features", *Chemical Society Reviews*, vol. 39, pp. 4370-4387, 2010.

119. Z.Y. Guo, F.F Jian, F.L. Du, "A simple method to controlled synthesis of CeO2 hollow microspheres", *Scripta Materialia*, vol. 61, pp. 48-51, 2009.

120. A. Trovarelli, "Catalytic Properties of Ceria and CeO2-Containing Materials", *Catalysis Reviews: Science and Engineering*, vol. 38, p. 439, 1996.

121. M.S. Gross, M.A. Ulla, C.A. Querini, “Diesel particulate matter combustion with CeO2 as catalyst. Part I: System characterization and reaction mechanism”, *Journal of Molecular Catalysis A: Chemical* vol. 352, pp. 86-94, 2012.

122. S. Imamura, A. Doi, and S. Ishida, “Wet oxidation of ammonia catalyzed by cerium-based composite oxides”, *Industrial & Engineering Chemistry Product Research and Development*, vol. 24, pp. 75-80, 1985.

123. P. Palmisano, N. Russo, P. Fino, D. Fino, and C. Badini, “High catalytic activity of SCS-synthesized ceria towards diesel soot combustion”, *Applied Catalysis B Environmental*, vol. 69, pp. 85-92, 2006.

124. K. Pollard, H. A. Jenkins, and R. J. Puddephatt, “Chemical Vapor Deposition of Cerium Oxide Using the Precursors [Ce(hfac)3(glyme)]”, *Chemistry of Materials*, vol. 12, pp. 701-710, 2000.

125 R. I. Walton, “Solvothermal synthesis of cerium oxides”, *Progress in Crystal Growth and Characterization of Materials*, vol. 57, pp. 93-108, 2011.

126. L. Yang, X. Pang, G. Fox-Rabinovich, S. Veldhuis, and I. Zhitomirsky, “Electrodeposition of cerium oxide films and composites”, *Surface & Coatings Technology*, vol. 206, pp. 1-7, 2011.

127. A. Turkovic, P. Dubcek and S. Bernstorff, “Grazing-incidence small-angle and wide-angle scattering of synchrotron radiation on nanosized CeO2 thin films”, *Materials Science & Engineering*, vol. B58, pp. 263-269, 1999.

128. J. Päiväsaari, M. Putkonen, and L. Niinistö, “Cerium dioxide buffer layers at low temperature by atomic layer deposition”, *Journal of Materials Chemistry*, vol. 12, pp. 1828-1832, 2002.

129. A. Marizy, P. Roussel, A. Ringuede, and M. Cassir, “Atomic layer deposition of epitaxial CeO2 thin layers for faster surface hydrogen oxidation and faster bulk ceria reduction/reoxidation”, *Journal of Materials Chemistry A*, vol. 3, pp. 10498-10503, 2015.

130. Z. Fan, J. An, A. Iancu, and F.B. Prinz, “Thickness effects of yttria-doped ceria interlayers on solid oxide fuel cells”, *J. Power Sources*, vol. 218, pp. 187-191, 2012.

131. M. Coll, A. Palau, J.C. Gonzalez-Rosillo, J. Gazquez, X. Obradors, and T. Puig, “Integration of atomic layer deposition CeO2 thin films with functional complex oxides and 3D patterns”, *Thin Solid Films* vol. 553, pp. 7-12, 2014.

132. H.C. Aspinall, J. Bacsa, A.C. Jones, J.S. Wrench, K. Black, P.R. Chalker, P.J. King, P. Marshall, M. Werner, H.O. Davies, R. Odedra, “Ce (IV) complexes with donor-functionalized alkoxide ligands: improved precursors for chemical vapor deposition of CeO2”, *Inorganic chemistry*, vol. 50 (22), pp. 11644–11652, 2011.

133. W.-H. Kim, M.-K. Kim, W. J. Maeng, J. Gatineau, V. Pallem, C. Dussarrat, A. Noori, D. Thompson, S. Chu and H. Kim, "Growth Characteristics and Film Properties of Cerium Dioxide Prepared by Plasma-Enhanced Atomic Layer Deposition", *Journal of The Electrochemical Society.*, vol. 158, issue 8, pp. G169-G172, 2011.

134. M. Golalikhani, T. James, P. Van Buskirk, W. Noh, J. Lee, Z. Wang, and J. F. Roeder, "Atomic layer deposition of CeO2 using a heteroleptic cyclopentadienyl-amidinate precursor", *Journal of Vacuum Science & Technology A,* vol. 36, p. 051502, 2018.

135. S. Vangelista, R.Piagge, S. Ek, T. Sarnet, G. Ghidini, C. Martella, A. Lamperti, " Structural, Chemical and Optical Properties of Cerium Dioxide Film Prepared by Atomic Layer Deposition on TiN and Si Substrates", *Thin Solid Films*, vol. 636, pp. 78-84, 2017.

136. J. S. Wrench, K. Black, H.C. Aspinall, A. C. Jones, J. Bacsa, P.R. Chalker, P.J. King, M. Werner, H.O. Davies, P. N. Heys, "MOCVD and ALD of CeO2 Thin Films using a Novel Monomeric CeIV Alkoxide Precursor", *Chemical Vapor Deposition*, vol. 15, issue 10-12, pp. 259-261, 2009.

137. W.-H. Kim, M.-K. Kim, I.-K. Oh, W.J. Maeng, T. Cheon, S.-H. Kim, A. Noori, D. Thompson, S. Chu, H. Kim, "Significant Enhancement of the Dielectric Constant through the Doping of CeO2 into HfO2 by Atomic Layer Deposition", *Journal of the American Ceramic Society*, vol. 97, Issue 4, pp. 1164-1169, 2014.

138. P.J. King, M. Werner, P.R. Chalker, A.C. Jones, H.C. Aspinall, J. Basca, J.S. Wrench, K. Black, H.O. Davies, P.N. Heys, "Effect of deposition temperature on the properties of CeO2 films grown by atomic layer deposition", *Thin Solid Films*, vol. 519, pp. 4192-4195, 2011.

139. M. Kouda, K. Ozawa, K. Kakushima, P. Ahmet, H. Iwai, Y. Urabe, and T. Yasuda, "Preparation and Electrical Characterization of CeO2 Films for Gate Dielectrics Application: Comparative Study of Chemical Vapor Deposition and Atomic Layer Deposition Processes", *Japanese Journal of Applied Physics*, vol. 50, p. 10PA06, 2011.

140. M. Machida, Y. Murata, K. Kishikawa, D. Zhang, K. Ikeue, "On the Reasons for High Activity of CeO2 Catalyst for Soot Oxidation", *Chemistry of Materials.*, vol. 20, pp. 4489-4494, 2008.

141. K. Yamazaki, T. Kayama, F. Dong, H. Shinjoh, "A mechanistic study on soot oxidation over CeO2-Ag catalyst with 'rice-ball' morphology", *Journal of Catalysis*, vol. 282(2), pp. 289-298, 2011.

142. K.I.Shimizu, H. Kawachi, A. Satsuma, "Study of active sites and mechanism for soot oxidation by silver-loaded ceria catalyst", *Applied Catalysis B Environmental*, vol. 96(1), pp. 169-175, 2010

143. G. Preda, G. Pacchioni, "Formation of oxygen active species in Ag-modified CeO2 catalyst for soot oxidation: A DFT study", *Catalysis Today*, vol. 177 (1), pp. 31-38, 2011.

144. K.I.Shimizu, H. Kawachi, S.I. Komai, K. Yoshida, Y. Sasaki, A. Satsuma, "Carbon oxidation with Ag/ceria prepared by self-dispersion of Ag powder into nano-particles", *Catalysis Today*, vol. 175(1), pp. 93-99, 2011

145. K. Yamazaki, Y. Sakakibara, F. Dong, H. Shinjoh, "The remote oxidation of soot separated by ash deposits via silver-ceria composite catalysts", *Applied Catalysis A: General*, vol. 476, pp. 113-120, 2014.

146. H. Wang, S. Liu, Z. Zhao, X. Zou, M. Liu, W. Liu, X. Wub, D, Weng, "Activation and deactivation of Ag/CeO2 during soot oxidation: influences of interfacial ceria reduction", *Catalysis Science & Technology*, vol. 7, pp. 2129-2139, 2017.

147. T. Kayama, K. Yamazaki, H. Shinjon, "Nanostructured Ceria−Silver Synthesized in a One-Pot Redox Reaction Catalyzes Carbon Oxidation", *Journal of the American Chemical Society*., vol. 132, pp. 13154-13155, 2010.

148. A. Rangaswamy, P. Sudarsanam, B.M. Reddy, "Rare earth metal doped CeO2-based catalytic materials for diesel soot oxidation at lower temperatures", *Journal of Rare Earths*, vol. 33, pp. 1162–1169, 2015.

149. L. Castoldi, E. Aneggi, R. Matarrese, R. Bonzi, J. Llorca, A. Trovarelli, L. Lietti, "Silver-based catalytic materials for the simultaneous removal of soot and NOx", *Catalysis Today*, vol. 258, pp. 405–415, 2015.

150. A. Niskanen, T. Hatanpää, K. Arstila, M. Leskelä and M. Ritala, "Radical-Enhanced Atomic Layer Deposition of Silver Thin Films Using Phosphine-Adducted Silver Carboxylates", *Chemical Vapour Deposition* vol. 13, pp. 408-413, 2007.

151. M. Kariniemi, J. Niinistö, T. Hatanpää, M. Kemell, T. Sajavaara, M. Ritala, M. Leskelä, " Plasma-Enhanced Atomic Layer Deposition of Silver Thin Films", *Chemistry of Materials* vol. 23, pp. 2901-2907, 2011.

152. A. Amusan, B. Kalkofen, H. Gargouri, K. Wandel, C. Pinnow, M. Lisker, E.P. Burte, "Ag Films Grown by Remote Plasma Enhanced Atomic Layer Deposition on Different Substrates", *Journal of Vacuum Science and Technology A*, vol. 34(01), p. 01A126, 2016.

153. M. M. Minjauw, E. Solano, S. P. Sree, R. Asapu, M. Van Daele, R. K. Ramachandran, G. Heremans, S. W. Verbruggen, S. Lenaerts, J. A. Martens, C. Detavernier, J. Dendooven, "Plasma-Enhanced Atomic Layer Deposition of Silver Using Ag(Fod)(PEt3) and NH3-Plasma", *Chemistry of Materials* vol. 29, pp. 7114-7121, 2017.

154. Z, Golrokhi, S. Chalker, C. J. Sutcliffe, R. Potter, "Self-limiting atomic layer deposition of conformal nanostructured silver films", *Applied Surface Science.*, vol. 364, pp. 789-797, 2016.

155. Z. Golrokhi, P. A. Marshall, S. Romani, S. Rushworth, P. R. Chalker, R. Potter, "The influence of tertiary butyl hydrazine as a co-reactant on the atomic layer deposition of silver", *Applied Surface Science* vol. 399, pp. 123-131, 2017.

156. S. S. Masango, L. Peng, L. D. Marks, R. P. Van Duyne, P. C. Stair, "Nucleation and Growth of Silver Nanoparticles by AB and ABC-Type Atomic Layer Deposition", *The Journal of Physical Chemistry C*, vol. 118, pp. 17655-17661, 2014.

157. M. Mäkelä, T. Hatanpää, K. Mizohata, K. Meinander, J. Niinistö, J. Räisänen, M. Ritala, M. Leskelä, " Studies on Thermal Atomic Layer Deposition of Silver Thin Films", *Chemistry of Materials* vol. 29, pp. 2040-2045, 2017

158. N.H. Dryden, J.J. Vittal, and R.J. Puddephatt, "New precursors for chemical vapor deposition of silver", *Chemistry of Materials* vol. 5, pp. 765-766, 1993.

159. Z. Fang, X. Qiu, Y. Qiu, E. Kuffel, "Dielectric barrier discharge in atmospheric air for glass-surface treatment to enhance hydrophobicity", *IEEE Xplore: IEEE Transactions on Plasma Science* vol. 34, pp. 1216-1222, 2006.

160. J. Aarik, A. Aidla, V. Sammelselg, and T. Uustare, "Effect of growth conditions on formation of TiO2-II thin films in atomic layer deposition process", *Journal of Crystal Growth*, vol. 181, pp. 259-264, 1997.

161. Y.-J. Shi, R.-J. Zhang, H. Zheng, D.-H. Li, W. Wei, X. Chen, Y. Sun, Y.-F. Wei, H.-L. Lu, N. Dai, L.-Y. Chen, "Optical Constants and Band Gap Evolution with Phase Transition in Sub-20-nm-Thick TiO2 Films Prepared by ALD", *Nanoscale Research Letters*, vol. 12, p. 243, 2017.

162. J. Z. Shyu, K. Otto, and W. L. Watkins, "Characterization of Pd/γ-alumina catalysts containing ceria", *Journal of Catalysis*, vol. 114, pp. 23-33, 1988.

163. G. Sadanandam, V.D. Kumari, M.S. Scurrell, "Highly stabilized Ag2O-loaded nano TiO2 for hydrogen production from glycerol: Water mixtures under solar light irradiation", *International Journal of Hydrogen Energy*, vol. 42, pp. 807–820, 2017.

164. A.A. Ansari, J.P. Labis, M. Alam, S.M. Ramay, N. Ahmed, A. Mahmood, "Preparation and spectroscopic, microscopic, thermogravimetric, and electrochemical characterization of silver-doped cerium(IV) oxide nanoparticles", *Analytical Letters* vol. 50, pp. 1360–1371, 2017.

165. S.S. Deshpande, S.V.N. Patil, T. Kuchibhatla, S. Seal, "Size dependency variation in lattice parameter and valency states in nanocrystalline cerium oxide", *Applied Physics Letters* vol. 87, p. 133113, 2005.

166. S. Cai, D. Zhang, L. Zhang, L. Huang, H. Li, R. Gao, L. Shi, J. Zhang, "Comparative study of 3D ordered macroporous Ce0.75Zr0.2M0.05O2−δ (M = Fe, Cu, Mn, Co) for selective catalytic reduction of NO with NH3", *Catalysis Science & Technology* vol. 4, pp. 93–101, 2014.

167. G. Zou, Z. Fan, X. Yao, Y. Zhang, Z. Zhang, M. Chen, W. Shangguan, “Catalytic performance of Ag/Co-Ce composite oxides during soot combustion in O2 and NOx: Insights into the effects of silver”, *Chinese Journal of Catalysis* vol. 38, pp. 564–572, 2017.

Publication I

Ivanova T.V., Hoder T., Kääriäinen M.-L., Komlev A., Brandenburg R., and Cameron D.C.
Enhancement of Atmospheric Plasma Decomposition of Toluene Using Porous Dielectric Conformally Coated with Titanium Dioxide by Atomic Layer Deposition

Reprinted with permission from
Science of Advanced Materials
Vol. 6, pp. 2098-2105(8), 2014
© 2014, American Scientific Publishers

Copyright © 2014 by American Scientific Publishers
All rights reserved.
Printed in the United States of America

AMERICAN SCIENTIFIC PUBLISHERS

Science of Advanced Materials
Vol. 6, pp. 1–8, 2014
(www.aspbs.com/sam)

ARTICLE

Enhancement of Atmospheric Plasma Decomposition of Toluene Using Porous Dielectric Conformally Coated with Titanium Dioxide by Atomic Layer Deposition

Tatiana V. Ivanova[1,*], Tomáš Hoder[2], Marja-Leena Kääriäinen[1], Andrei Komlev[3], Ronny Brandenburg[2], and David C. Cameron[1,†]

[1]*ASTRaL, Lappeenranta University of Technology, Sammonkatu 12, 50130 Mikkeli, Finland*
[2]*Leibniz Institute for Plasma Science and Technology, INP Greifswald e.V., Felix-Hausdorff-Str. 2 17489 Greifswald, Germany*
[3]*Saint-Petersburg State Institute of Technology (Technical University), Moskovskiy Prospect 26, 190013 Saint-Petersburg, Russia*

ABSTRACT

The use of atmospheric pressure plasmas together with catalysts for removal of organic volatile compounds (VOCs) from the atmosphere is an area of current research. Dielectric barrier discharge (DBD) systems are widely used to produce non-thermal atmospheric pressure plasmas. For the most effective use of catalysts, it is necessary to maximize the surface area which is exposed to the contaminant and to the active species from the plasma. In this work, we have used atomic layer deposition (ALD) to deposit titanium dioxide catalytic thin films in porous glass labyrinths. ALD is known to produce effective photocatalytic TiO_2 layers and one of its characteristics is the ability to deposit on the internal surfaces within a complex porous material. The performance of a parallel plate DBD system has been tested for the decomposition of toluene. DBD systems with interelectrode material of (a) uncoated porous glass and (b) TiO_2 coated porous glass have been studied. Porous glass has been used to increase the flow path of the gases and to maximize the surface area of the interelectrode medium. The effects of the thickness of TiO_2 and specific input energy (SIE) on the conversion efficiency of the VOCs to CO_2 and CO were measured. The breakdown products of the decomposition were determined by using FTIR absorption measurements for the exhaust gases. Based on these measurements, the carbon balance was close to 100%. The contribution of catalytic reactions to the decomposition became increasingly dominant as specific input energy was increased. The incorporation of the ALD TiO_2 enabled the complete destruction of toluene at a concentration of 2450 ppm in air with an SIE of 336 J/l.

KEYWORDS: Titanium Dioxide, Dielectric Barrier Discharge, Atomic Layer Deposition.

1. INTRODUCTION

The emission of volatile organic compounds (VOCs) by industrial sources endangers human health and is harmful to the environment. Several methods have been investigated for removing VOCs, such as adsorption and thermal orthermocatalytic oxidation. However, these are not optimal due to high energy consumption.[1] Among other methods, nonthermal plasma (NTP) has been used for the removal of VOC, SO_2 and NO_x without preheating the fuel gas.[2,3]

Enhancement of efficiency of VOC removal can be achieved by combination of NTP with catalysts.[4] In practice, a heterogeneous catalyst can be combined with NTP in two ways: by introducing the catalyst in the discharge zone or by placing the catalyst after the discharge zone. When the catalyst is packed in the plasma reactor and can be directly activated by the plasma it is called single-stage plasma or in-plasma catalysis.[5] In the case of in-plasma catalysis, the activation mechanisms include local heating, changes in work function, activation of lattice oxygen, as well as enhanced adsorption/desorption of molecules, enhanced ozone decomposition to form active oxygen

*Author to whom correspondence should be addressed.
Email: tatiana.ivanova@lut.fi
†Present address: MiktechOy, Sammonkatu 12, 50130 Mikkeli, Finland.
Received: xx xx xxxx
Accepted: xx xx xxxx

radicals and direct interaction of gas-phase radicals with adsorbed pollutants.[6,7]

Comparative assessment of different types of NTP reactors in toluene decomposition has shown that the dielectric barrier discharge (DBD)[8] reactor combined with catalyst is the most effective in terms of energy efficiency and carbon balance.[9–12] If the ultraviolet (UV) radiation from the plasma can be used by a photocatalyst to create electron–hole pairs, the efficiency could be enhanced. Titanium dioxide TiO_2 is the most widely used semiconductor photocatalyst for the decomposition of organic material because of its high photosensitivity, photochemical stability, strong oxidizing power and non-toxic nature.[13] Under irradiation with photons of energy greater or equal to the bandgap energy ($E_g = 3.2$ eV for the anatase phase[14]) of semiconductors, electron–hole pairs are formed which enable oxidation–reduction reactions to take place at the surface of semiconductor. In the oxidative reaction, the positive holes oxidize water molecules on the surface to create a hydroxyl radicals $^{\bullet}OH$ and electrons reduce oxygen in the air-containing system into triplet oxygen O_2^-.[15] These radicals can decompose VOCs to non-toxic molecules such as CO_2 and H_2O.

The efficiency of the catalyst is very much dependent on the structure and composition of the TiO_2. Doping of metals such as Ag and Fe in TiO_2 structure can enhance absorption of visible light, thereby enhancing photocatalytic activity[16,17] and co-doping with $Zr^{+4}$and F^- in the anatase lattice can increase the stability of TiO_2.[18] The photocatalytic efficiency of TiO_2 can be enhanced by careful control of the film thickness and structure.[14,19] This to be done in a form suitable for a catalytic reactor, therefore TiO_2 needs to be deposited uniformly on a large surface area material, such as a labyrinthine porous material.

Uniformly deposited layers on porous labyrinths cannot be achieved by typical chemical vapor deposition (CVD) processes since the long diffusion paths for reactant molecules to reach the inner surfaces affect the uniformity of the film thickness. Atomic layer deposition (ALD) enables precise deposition of ultra-thin and highly conformal coatings on substrates with high complexity. In ALD, the uniformity of film thickness is decoupled from the rate of arrival of the reactant molecules. A reaction cycle consists of two reaction steps where the precursors are each supplied to the surface during different time slots. Each precursor reacts in turn with the surface to form a monolayer of chemisorbed molecules. There is no mixing of the precursors in the gas phase and the only reactions take place on the substrate surface. Consequently, the thickness is not dependent on the arrival rate of molecules at the surface, only on the presence of a saturated layer of chemisorbed molecules. The thickness of the films can be controlled by the number of deposition cycles. The ALD process allows the growth of uniform films even on complex shapes such as the internal surfaces of porous materials provided the pores are bigger than the precursor molecules.[20–22]

Previous studies have used simple glass and TiO_2 pellets as packed materials.[23] Chang[11] et al. measured decomposition efficiency for toluene with concentration 1100 ppm up to 78%, achieved with packed TiO_2 coated pellets in the plasma zone compare to 35% with a non-packed zone. In a study by Li[24] et al. a DC streamer corona discharge was employed in combination of TiO_2 pellets and showed the best performance for toluene decomposition of 76% and energy efficiency 7.2 g/kW. Kang[25] et al. showed the conversion of 1000 ppm toluene of nearly 70% which has been achieved at pulse voltage of 13 kV after 120 min with aTiO_2/O_2 plasma system.

In the work reported here, a single-stage DBD reactor with photocatalytic material inside the plasma zone was studied. TiO_2 catalytic thin films were uniformly deposited by ALD on borosilicate porous filter discs with high surface area. Their performance during VOC abatement was tested by the destruction of toluene with a relatively high concentration of 2450 ppm in air and it was found that effectively complete destruction could be achieved. The effects of the thickness of TiO_2 and specific input energy (SIE) were measured on the conversion efficiency of the VOCs.

2. EXPERIMENTAL DETAILS

2.1. Experimental Setup

A schematic diagram of the experimental setup is illustrated in Figure 1. The experimental apparatus includes of syringe pump, gas generation unit, a plasma reactor and a gas analysis unit. Toluene was introduced with a motor-driven syringe pump (1) and was diluted by a stream of synthetic air (20% oxygen and 80% nitrogen) with the flow rate adjustable by a mixture system (2). The organic-air gas mixture flow was directed using a two-way solenoid valve (3) into the plasma DBD reactor (4) or to the exhaust. The operating condition was fixed at an airflow rate of 1250 ml/min and a toluene concentration at 2450 ppm. The experiments were carried out at room temperature and atmospheric pressure. For detection of organic compounds and the formation of oxides an on-line Fourier transform infrared spectroscopy (FTIR) (Gasmet CR-2000, Ansyco, Germany) was used. Gas measurements

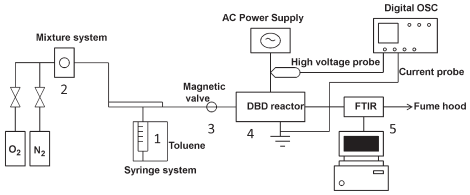

Fig. 1. Experimental setup.

were made at 5 sec intervals. The gas cell was heated to 60 °C to prevent any possible condensation. The CO_2 and CO selectivities were calculated as follows:

$$S_{CO_2}(\%) = \frac{[CO_2]}{[CO_2]+[CO]} \times 100 \quad (1)$$

$$S_{CO}(\%) = \frac{[CO]}{[CO_2]+[CO]} \times 100 \quad (2)$$

The carbon balance was obtained from the sum of two products:

$$\text{Carbon balance } (\%) = \frac{[CO]+[CO_2]}{7 \times ([VOC]_0 - [VOC])} \times 100 \quad (3)$$

2.2. Catalyst Preparation

Borosilicate porous glassfilter discs (ROBU glasfiltergerate GMBH, Germany) 30 mm in diameter and 1 mm in thickness were used as a substrate for the TiO_2 film. The specifications are shown in Table I. The titanium dioxide films were grown in a TFS 500 ALD reactor (BeneqOy, Finland). The precursors used were titanium tetrachloride (99.0% Fluka) and deionised water. These were held at 23 °C in external reservoirs and were led into the reactor through needle and solenoid valves. Nitrogen (99.999%) was used as a carrier gas and for purging between precursor pulses.

Before the reaction, the filter discs were kept overnight at 350 °C in the reactor chamber under vacuum to remove moisture from the porous labyrinths. One cycle of the ALD process was carried out according to the following steps: $TiCl_4$ pulse-N_2 purging-H_2O pulse-N_2 purging. The mean thickness of deposited TiO_2 film on porous filters was controlled by the number of ALD cycles. Four thicknesses of titanium dioxide corresponding to 250, 500, 1000 and 1500 cycles were deposited on the porous substrates at a reaction temperature of 350 °C. The pulse-exposure times of $TiCl_4$ and H_2O were 10 s and 8 s in the reactor, respectively. The purge time was 4 s after each precursor. The pressure of the ALD reactor was $5 \times 10^2 - 1 \times 10^3$ Pa.

2.3. Catalyst Characterization Methods

The characterization of the structure and crystalline phases of the films was made by X-ray diffractometry (XRD) (ShimadzuXRD-7000) using CuKα ($\lambda = 1.54$ Å) as the X-ray source, operated at 35 kV and 30 mA. The scanning rate was 2 °/min in the 2Θ range 20–60°. The crystal structure and crystal size of titanium dioxide film were studied by field emission scanning electron microscope (FESEM) (Hitachi S4800) equipped with an EDAX EDX detector unit for elemental analysis while imaging. The UV transmittance studies of porous discs with and without ALD coating were carried out using the UV-VIS spectrophotometer NICOLET 500. The amount of TiO_2 deposited on the porous filter discs was measured by weighing.

Table I. Pore volumes and inner surface of porous filter discs.

Filter type	Pore size, (μm)	Pore volume, (%)	Specific surface area, Brunauer–Emmett–Teller (BET), (m^2/gr)
P2	40–100	36	0.13

2.4. Electrical Measurements

Flow-type experiments were carried out using a single-stage parallel-plate dielectric barrier discharge (DBD) reactor. Before every experiment, the discharge was driven for 10 min without VOC addition in order to have a stable temperature in the system. The reactor (Fig. 2) was made of two plates of borosilicate glass. Copper tape glued on the outer surface of the borosilicate glass plates acted as a high voltage electrode. A Teflon spacer was used to provide the gas-phase discharge zone of 1 mm thickness in which the TiO_2 coated porous glass discs were situated. The length and width of the discharge zone was 100 mm and 50 mm, respectively. The non-thermal plasma was generated by applying 1 kHz AC voltage to the reactor. The voltage was measured by a 1000:1 high-voltage probe (Tektronix probe P6015A). The reactor current (I) was measured across an appropriate resistor. The power (W) (current–voltage multiplication) was computed and simultaneously shown by the oscilloscope (Tektronix TDS 3052). The current–voltage product values were calibrated by a Lissajous figure method for the exact power estimation to assure accurate data. The specific input energy (SIE) was varied by changing the applied voltage and was calculated as:

$$\text{SIE}\left(\frac{J}{l}\right) = \frac{\text{Power (W)}}{\text{Gas flow rate (l/s)}} \quad (4)$$

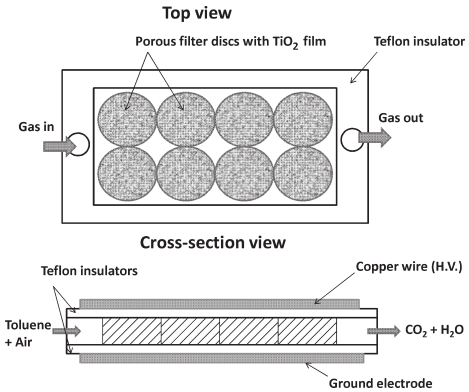

Fig. 2. Schematic diagram of the DBD reactor packed with porous discs covered by TiO_2 catalysts (top and cross-section views).

ARTICLE

3. RESULTS AND DISCUSSION

3.1. Characterization of Catalysts

Measurement of nm-scale film thickness inside a labyrinth is difficult, therefore the quantity of TiO_2 deposited on the porous glass filters was determined by weight measurements performed before and after the ALD coating using an analytical balance. In ALD it is important that the precursor pulses are long enough to ensure that the substrate surface is saturated with reactive species and that the thickness of coating is not dependent on the precursor exposure time. The necessary exposure time to achieve saturation for the TiO_2 ALD on filters P2is shown in Figure 3 for a 500 cycle process. The time sequence is x-8s-4s-4s ($TiCl_4$-purge-H_2O-purge) where the $TiCl_4$ exposure time, x, was varied between 0 and 15 s. Figure 3 shows that the weight gain increases with exposure time below 10 s after which the weight gain was constant. Additional weight gain measurements varying the H_2O exposure time (not shown) verified that the 4 s H_2O exposure was sufficient to ensure saturation. It was also confirmed that the purge pulses were long enough to ensure that there was no CVD element in the film deposition.

Theoretically, for a certain mass of TiO_2 on a porous substrate, the thickness of TiO_2 can be estimated by the mass and the surface area of the filter discs before and after ALD coatings. For example, the TiO_2 masson substrate P2 after 500 ALD-cycles is approximately 7 mg. Assuming the density of TiO_2 is the bulk density of 4.23 g/cm^3,[26] the thickness of the TiO_2 film is approximately 10.8 nm. This corresponds to a growth rate of 0.22 Å/cycle. The TiO_2 thickness measurements were also made by ellipsometry on silicon substrates and indicated 19 nm after 500 ALD coatings. The difference between the calculated and the measured thickness is probably due to the density of the TiO_2 films being less than that of bulk material, a commonly observed feature.

The ALD TiO_2 timing sequence was held constant at 10-8-4-4 s and the number of exposures was varied between 250 and 1500 cycles for porous substrates P2. The results of weight gain measurements of TiO_2 deposited versus number of ALD cycles are shown in Figure 4. This figure indicates a linear dependence between the film thickness and the number of growth cycles.

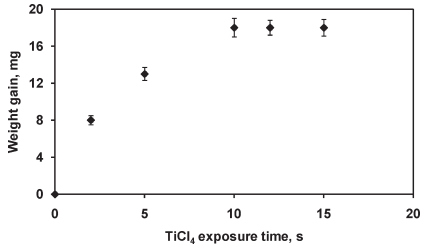

Fig. 3. Mass of ALD deposited TiO_2 versus $TiCl_4$ exposure pulse time performed on porous substrates P2, obtained from weight-gain measurements.

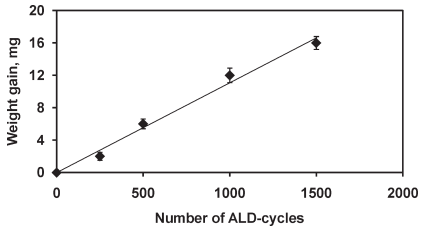

Fig. 4. Mass of TiO_2 deposited versus number of ALD-cycles performed on porous substrates P2 obtained from weight gain measurements.

Scanning electron micrographs of TiO_2 films on the internal surfaces of the porous glass filters are shown in Figure 5. As the film thickness increases the grain growth also increases. The average grain size can be evaluated from the SEM images. The average lateral grain sizes for different number of process cycles are shown in Table II.

The X-ray diffraction (XRD) pattern of TiO_2 films on substrates P2 is shown in Figure 6. The XRD patterns of TiO_2-coated porous glass exhibited strong diffraction peaks at 25.3° indicating the existence of the (101) anatase peak. The intensity of this peak increased with increasing number of ALD cycles as expected from the increasing film thickness. In the case of 1500 ALD-cycles of TiO_2 tiny rutile peaks become visible at $2\theta = 27.4°$ and $2\theta = 36.1°$.

Peak profile analysis of the (101) reflection was performed in order to find the full width at half maximum (FWHM) and the crystal size was estimated using Scherrer's equation:[27]

$$\varepsilon = \frac{K\lambda}{b\cos\theta} \tag{5}$$

where ε is the apparent crystallite size, K is Scherrer's constant, λ is the wavelength of the radiation, b is the additional broadening due to the crystal size, and θ is the Bragg angle. Instrumental broadening effects were not taken into account since these were significantly smaller than the broadening due to the crystal size. It is important to remember that Scherrer's equation is not optimal for asymmetric crystallites because the Scherrer's constant K depends on the alignment of the reflection planes with the long or short dimensions of the crystallites.[28] The changes in crystal size are shown in Table II (assuming spherical shaped crystals). These show a similar behavior to the values derived from the SEM analysis for 500 ALD-cycled film. In other cases (for 1000 and 1500 ALD-cycles) the values obtained by XRD give a smaller value indicating plate-like crystallite shapes.

The areas of the (101) anatase peaks were calculated by fitting with Gaussian peaks. Figure 7 shows the increase in area with the number of cycles. This should

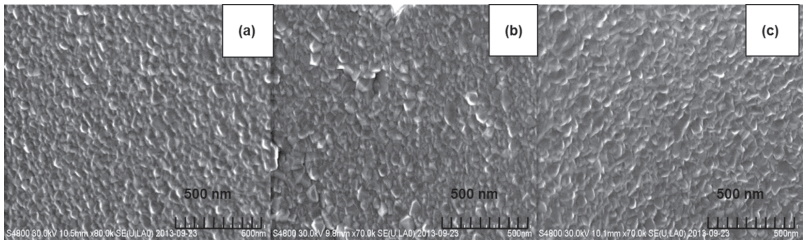

Fig. 5. Scanning electron micrographs of TiO_2 films on P2 substrates with different numbers of ALD-cycles: (a) 500 cycles, (b) 1000 cycles, (c) 1500 cycles.

Table II. Relation between number of ALD-cycles and grain size of the crystals based on SEM measurements and on Scherrer's equation.

Number of ALD-cycles	Grain size, nm (SEM)	Grain size, nm (Scherrer's equation)
500	27	26
1000	55	30
1500	75	44

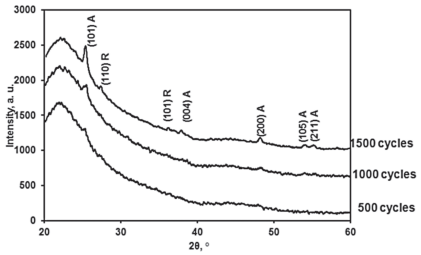

Fig. 6. XRD patterns of TiO_2 films coated at 350 °C on borosilicate porous discs P2 with different numbers of ALD-cycles (500, 1000, 1500 cycles).

be proportional to the film thickness and it shows a linear trend, similar to that obtained from the mass gain in Figure 4.

Chemical analysis of the TiO_2 thin films was performed by energy dispersive X-ray spectroscopy (EDX) across the cross-section of the filters. The EDX spectra indicated that all surfaces of the porous glass filters were covered with TiO_2. Exact determination of the Ti:O ratio is not possible since the oxygen signal comes largely from the borosilicate substrate.[29] The intensities of Ti Kα peaks increased linearly with increasing number of ALD-cycles confirming the data of Figures 4 and 7.

Figure 8 shows EDX measurements at 100 μm intervals along the cross-section of a P2 filter after coating for 1500 cycles. This demonstrates the uniform thickness of the film inside the porous material. Positions 0 and 1000 μm approximate to the outer surfaces of the filter.

It is expected that micro discharges will occur within the pores of the glass ensuring that all surfaces are activated. However, even in the absence of micro discharges, UV radiation can reach the internal surfaces. To illustrate this, the UV-visible transmittance spectra of TiO_2 thin film coated on porous glass filters were recorded in the wavelength range 200–600 nm. The optical transmittance spectra of bare porous borosilicate glass and coated by TiO_2 thin films with 500 and 1500 ALD-layers are shown in Figure 9. It can be seen that even with the 1500 cycle films, the UV radiation in the range 350–380 nm can penetrate at least 1 mm of coated porous glass therefore UV light generated on either side of the glass will penetrate 0.5 mm to the middle layers. It is also evident, as will be shown in Figure 12, that the uncoated porous glass is considerably less effective in removing toluene.

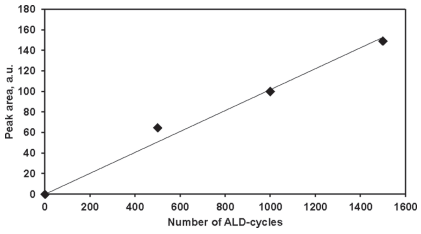

Fig. 7. Area of anatase TiO_2 (101) XRD peak as a function of the number of ALD-cycles.

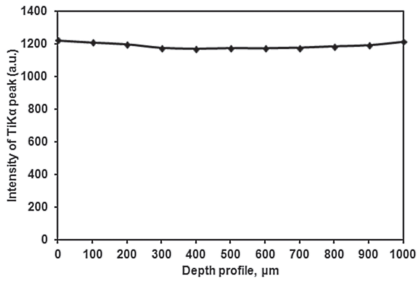

Fig. 8. Intensity of the TiKα peak along the cross-section of a P2 substrate after 1500 ALD-cycles.

ARTICLE

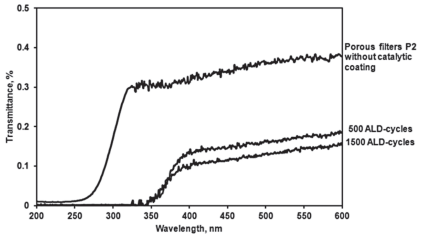

Fig. 9. UV-VIS transmission spectra of 500 and 1500 ALD-cycles of TiO_2 films deposited on porous glass substrates P2 and an uncoated porous glass substrate P2.

3.2. Time-Dependent Characteristics of Toluene Decomposition

Figure 10 shows ananalysis of toluene decomposition using the DBD reactor with 1000 ALD-cycles of TiO_2 catalyst at room temperature. Plasma was applied after adjustment of the toluene concentration to 2450 ppm. No decomposition of toluene occurred during the period without plasma, as shown by the increase and then saturation of the toluene concentration and the absence of decomposition products CO and CO_2. Therefore the TiO_2 does not operate as a catalyst in the absence of plasma. After the plasma was turned on, the concentration of toluene decreased and that of CO and CO_2 was increased. When the plasma was turned off, the concentration of toluene rapidly went up to its initial value and the formation of CO_2 and CO stopped.

3.3. Product Analysis Using FTIR

Figure 11 shows the FTIR spectra with and without plasma application. With photocatalytic coating on porous filters, the toluene was totally oxidized tothe major reaction products CO_2 and CO (Fig. 11(c)). However, plasmas can generate reaction intermediates, such as benzaldehyde and benzoic acid, in toluene oxidation, which can accumulate on the active sites of the photocatalyst surface. This effect can result in a decrease in photocatalytic activity with time. This effect was observed in Refs. [30–32]. In contrast,

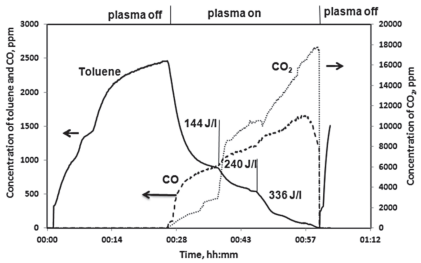

Fig. 10. Toluene decomposition using TiO_2 catalyst with 1000 ALD-cycles. SIEs are 144, 240 and 336 J/l.

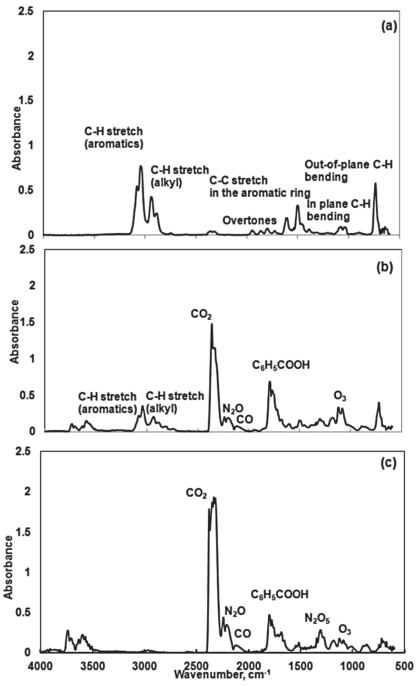

Fig. 11. FTIR spectra of reaction products in the DBD reactor: (a) 0 J/l, (b) 336 J/l with uncoated porous glass supports P2 and (c) 336 J/l with 1000 ALD-cycles of TiO_2 catalysts on porous glass supports P2.

ring-retaining products of toluene were observed in the DBD reactor with porous substrates without TiO_2 catalytic coating. The formation of nitrogen oxides (N_2O_5, NO, N_2O) is also unavoidable in air-like mixtures.

3.4. Effect of SIE on Toluene Removal Efficiency in the Catalytic DBD Reactor

Decomposition of toluene in air was measured using SIE values of 144, 240 and 336 J/l. Obviously, increase

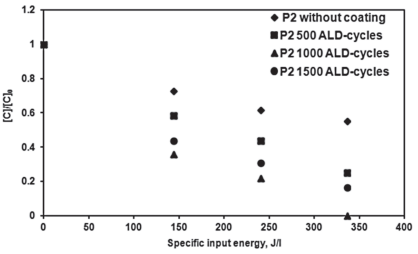

Fig. 12. Amounts of toluene decomposition as a function of the specific input energy for different TiO_2 catalyst thickness: bare filters P2, 500, 1000, 1500 ALD-cycles.

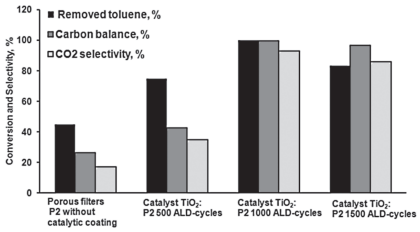

Fig. 13. Activity of TiO_2 catalysts (uncoated, 500, 1000, 1500 ALD-cycled filters) during the destruction of 2450 ppm of toluene at 336 J/l.

(decrease) of the input power could increase (decrease) increase the amount of toluene decomposed. In order to examine the influence of input power, SIE and number of TiO_2 ALD layers, the appropriate inlet toluene concentration was fixed at 2450 ppm. Samples with 500, 1000 and 1500 ALD-cycles of TiO_2 were used for the measurement. Filters with only 250 coating cycles showed results similar to uncoated discs. Figure 12 shows the toluene decomposition for uncoated porous glass and for coatings of different thicknesses as a function of SIE. The concentration of exhausted toluene decreased with the SIE in all cases. Toluene was completely converted to gaseous products with 1000 ALD-cycles films at SIE 336 J/l. It is noteworthy that the 1000 cycle films were more reactive than 1500 cycle films in the plasma decomposition of toluene. The reason for this is due to thicker films having a tendency to start to convert to the less catalytically active rutile phase.[33] The exact point of onset of transition to rutile was dependent on the precursor doses and pulse times. In addition, Kääriäinen et al.[14, 22] using TiO_2 deposited under similar conditions to here, observed that the best photocatalytic performance was obtained with films having the anatase phase of TiO_2 with approximately 15 nm film thickness which also contained a very small number of rutile crystallites, barely visible by XRD.

The decomposition and selectivity is further detailed in Figure 13. With uncoated porous filters at 336 J/l, the conversion of toluene is only ~45%. With 500 cycles of catalyst, ~75% of the toluene was decomposed. Approximately 100% decomposition of toluene was obtained with 1000 cycles. The carbon balance was also higher with 1000 cycles (100%) and 1500 cycles (~97%) as compared to 500 cycles (43%) and non-covered discs (26%). The selectivity to CO_2 increased to 93% with 1000 cycles coatings and 86% with 1500 cycles as compared to 35% with 500 cycles and 17% for uncoated filters.

4. CONCLUSIONS

The results show that the efficiency of VOC removal in a dielectric barrier discharge plasma decomposition system can be greatly increased by the use of a porous dielectric system internally coated with titanium dioxide as a catalyst activated by the plasma. They also show that anatase titanium dioxide can be uniformly coated inside a porous labyrinth material in a controllable manner by atomic layer deposition. It is demonstrated that titanium dioxide coatings of approximately 22 nm thickness are sufficient to remove approximately 100% of high concentrations of VOCs (2450 ppm toluene in this case) with high selectivity to CO_2 using a specific input energy of 336 J/l. The major reaction products are CO and CO_2 and the process is effective in removing all carbon ring-containing by-products. Atomic layer deposition is a process applicable to much larger sample sizes therefore this is a technique which could find application in large-scale practical systems.

Acknowledgments: The authors acknowledge the financial support of the European Regional Development Fund-supported Baltic Sea Region "PlasTEP" project. The authors are grateful to Michael Schmidt (INP Greifswald) for useful consultation.

References and Notes

1. C. Subrahmanyam, A. Renken, and L. Kiwi-Minsker, *Appl. Cat. B: Environmental* 65, 157 **(2006)**.
2. T. Oda, *J. Electrostatics* 57, 293 **(2003)**.
3. R. Brandenburg, V. V. Kovacevic, M. Schmidt, R. Basner, M. Kettlitz, G. B. Sretenovic, B. M. Obradovic, M. M. Kuraica, and K.-D. Weltmann, *Contrib. Plasma Phys.* 54, 202 **(2014)**.
4. A. M. Vandenbroucke, R. Morent, N. D. Geyter, and C. Leys, *J. Hazard. Mater.* 195, 30 **(2011)**.
5. H. H. Kim, S.-M. Oh, A. Ogata, and S. Futamura, *Appl. Catal., B: Environmental* 56, 213 **(2005)**.
6. H. H. Kim, A. Ogata, and S. Futamura, *Appl. Catal., B: Enviromental* 79, 356 **(2008)**.
7. U. Roland, F. Holzer, A. Poppl, and F.-D. Kopinke, *Appl. Catal., B: Enviromental* 58, 227 **(2005)**.
8. H.-E. Wagner, R. Brandenburg, K. V. Kozlov, A. Sonnenfeld, P. Michel, and J. F. Behnke, *Vacuum* 71, 417 **(2003)**.
9. C. Subrahmanyam, A. Renken, and L. Kiwi-Minsker, *Chemichal Engineering Journal* 134, 78 **(2007)**.
10. H. Huang and D. Ye, *J. Hazard. Mater.* 171, 535 **(2009)**.
11. C.-L. Chang and T.-S. Lin, *Plasma Chem. Plasma Process.* 25, 227 **(2004)**.
12. J. Y. Ban, Y. H. Son, M. Kang, and S. J. Choung, *Appl. Surf. Sci.* 253, 535 **(2006)**.
13. X. B. Chen, L. Liu, P. Y. Yu, and S. S. Mao, *Science* 331, 746 **(2011)**.
14. M.-L. Kääriäinen, T. O. Kääriäinen, and D. C. Cameron, *Thin Solid Films* 517, 6666 **(2009)**.
15. A. L. Linsebigler, G. Q. Lu, and J. T. Yates, *J. Chem. Rev.* 95, 735 **(1995)**.
16. M. K. Seery, R. George, P. Floris, and S. C. Pillai, *J. Photochem. Photobiol., A: Chemistry* 189, 258 **(2007)**.
17. Q. Jin, M. Fujishima, and H. Tada, *The Journal of Physical Chemistry C* 115, 6478 **(2011)**.
18. S. W. Liu, J. G. Yu, and S. Mann, *The Journal of Physical Chemistry C* 113, 10712 **(2009)**.
19. M.-L. Kääriäinen and D. C. Cameron, *Surf. Sci.* 606, 22 **(2011)**.
20. M. Ritala and M. Leskelä, Handbook of Thin Film Materials, edited by H. S. Nalwa, Academic Press, New York **(2002)**, Vol. 1, pp. 103–153.

ARTICLE

21. S. M. George, *Chem. Rev.* 110, 111 (**2010**).
22. X. Jiang, T. N. Gur, F. B. Prinz, and S. F. Bent, *Chem. Mater.* 22, 3024 (**2010**).
23. L. Zou, Y. Luo, M. Hooper, and E. Hu, *Chem. Eng. Process.* 45, 959 (**2006**).
24. D. Li, D. Yakushiji, S. Kanazawa, T. Ohkubo, and Y. Nomoto, *Journal Electrost* 55, 311 (**2002**).
25. M. Kang, B. J. Kim, S. M. Cho, C. H. Chung, B. W. Kim, G. Y. Han, and K. J. Yoon, *J. Mol. Catal. A: Chem.* 180, 125 (**2002**).
26. J. D. Ferguson, A. R. Yoder, A. W. Weimer, and S. M. George, *Appl. Surf. Sci.* 226, 393 (**2004**).
27. J. I. Langford and A. J. C. Wilson, *J. Appl. Crystallogr.* 11, 102 (**1978**).
28. M. Heikkilä, E. Puukilainen, M. Ritala, and M. Leskelä, *J. Photochem. Photobiol., A: Chemistry* 204, 200 (**2009**).
29. I. Hotovy, A. Pullmannova, M. Predanocy, J. Hotovy, V. Rehacek, T. Kups, and L. Spiess, *Journal of Electrical Engineering* 60, 354 (**2009**).
30. R. Mendez-Roman and N. Cardona-Martinez, *Catal. Today* 40, 353 (**1998**).
31. G. Marci, M. Addamo, V. Augugliaro, S. Coluccia, E. Garcia-Lopez, V. Loddo, G. Martra, L. Palmisano, and M. Schiavello, *J. Photochem. Photobiol. A* 160, 105 (**2003**).
32. F. L. Cao, J. G. Wang, F. J. Lv, D. Q. Zhang, Y. N. Huo, G. S. Li, H. X. Li, and J. Zhu, *Catal. Commun.* 12, 946 (**2011**).
33. J. Aarik, A. Aidla, V. Sammelselg, and T. Uustare, *J. Cryst. Growth* 181, 259 (**1997**).

ARTICLE

Publication II

Cameron D.C., Krumpolec R., Ivanova T.V., Homola T., Cernák M.
Nucleation and initial growth of atomic layer deposited titanium oxide determined by spectroscopic ellipsometry and the effect of pretreatment by surface barrier discharge

Reprinted with permission from
Applied Surface Science
Vol. 345, pp. 216–222, 2015
© 2015, Elsevier

Applied Surface Science 345 (2015) 216–222

Contents lists available at ScienceDirect

Applied Surface Science

journal homepage: www.elsevier.com/locate/apsusc

Nucleation and initial growth of atomic layer deposited titanium oxide determined by spectroscopic ellipsometry and the effect of pretreatment by surface barrier discharge

David C. Cameron[a,*], Richard Krumpolec[b], Tatiana V. Ivanova[c], Tomáš Homola[a], Mirko Černák[a]

[a] R&D Centre for Low-Cost Plasma and Nanotechnology Surface Modification, Masaryk University, Kotlářská 267/2, 611 37 Brno, Czech Republic
[b] Department of Experimental Physics, Faculty of Mathematics, Physics and Informatics, Comenius University, Mlynská dolina, 842 4 Bratislava, Slovakia
[c] ASTRaL team, Laboratory of Green Chemistry, Lappeenranta University of Technology, Sammonkatu 12, 50130 Mikkeli, Finland

ARTICLE INFO

Article history:
Received 9 January 2015
Received in revised form 18 March 2015
Accepted 21 March 2015
Available online 28 March 2015

Keywords:
Atomic layer deposition
Spectroscopic ellipsometry
Quantum confinement effects
Nucleation density

ABSTRACT

This paper reports on the use of spectroscopic ellipsometry to characterise the initial nucleation stage of the atomic layer deposition of the anatase phase of titanium dioxide on silicon substrates. Careful control and analysis of the ellipsometric measurements enables the determination of the evolution of crystallite diameter and surface density in the nucleation stage before a continuous film is formed. This growth behaviour is in line with atomic force microscopy measurements of the crystallite size. The crystallite diameter is a linear function of the number of ALD cycles with a slope of approximately 1.7 Å cycle^{-1} which is equivalent to a layer growth rate of 0.85 Å cycle^{-1} consistent with a ripening process which increases the crystallite size while reducing their density. The crystallite density decreases from $\sim 3 \times 10^{17}$ m^{-3} in the initial nucleation stages to $\sim 3 \times 10^{15}$ m^{-3} before the film becomes continuous. The effect of exposing the substrate to a diffuse coplanar surface barrier discharge in an air atmosphere before deposition was measured and only small differences were found: the plasma treated samples were slightly rougher in the initial stages and required a greater number of cycles to form a continuous film (~80) compared to the untreated films (~50). A thicker layer of native oxide was found after plasma treatment.

© 2015 Elsevier B.V. All rights reserved.

1. Introduction

Dielectric barrier discharges (DBDs) are widely used for modification of various surfaces in order to passivate them, change their surface energy or modify the deposition behaviour of layers deposited on them [1–3]. DBD plasma sources have good process controllability, excellent treatment uniformity and high efficiency. Plasma treatment of substrates can generate various functional groups on the surface of materials such as hydroxyl-, carbonyl-, carboxyl-, amino-groups, etc.

Atomic layer deposition (ALD) is a thin film deposition process known for its ability to controllably deposit ultrathin layers with extreme uniformity. In ALD, the substrates are exposed to sequential pulses of reactant gases or vapours and each pulse forms an additional chemisorbed molecular layer. Between the reactant pulses, an inert gas (e.g. nitrogen) is used as a purge gas for removing all the excess precursor molecules which have not chemisorbed or undergone exchange reactions with the surface groups, and the reaction by-products [4]. It is widely accepted [5–8] that during ALD growth, the high density of active surface groups generated by plasma oxidation of a precursor monolayer can play an important role since during the subsequent precursor exposure these groups react with the incoming compounds which thereby become anchored. However, during the initial nucleation stage, where a precursor must react with the oxidised silicon substrate rather than a monolayer of the previous precursor, the action of the plasma on the silicon may not have such a significant effect.

Once the deposition process has reached a stable condition, the thickness of the films deposited by ALD is normally assumed to be strictly proportional to the number of ALD cycles applied. However, this requires that the film is dense and uniform and clearly

* Corresponding author.
E-mail addresses: dccameron@mail.muni.cz (D.C. Cameron), richard.krumpolec@fmph.uniba.sk (R. Krumpolec), tatiana.ivanova@lut.fi (T.V. Ivanova), tomas.homola@mail.muni.cz (T. Homola), cernak@physics.muni.cz (M. Černák).

http://dx.doi.org/10.1016/j.apsusc.2015.03.135
0169-4332/© 2015 Elsevier B.V. All rights reserved.

cannot hold for the period from the initial nucleation until a coherent film is formed. During this time, growth typically proceeds by the formation of a certain surface density of nuclei followed by their expansion and eventual coalescence into a continuous film in a Volmer-Weber process [9]. The amount of material deposited during growth can be measured by deposition on a quartz crystal microbalance but this only gives the mass of material deposited. It does not give any information about the nucleation density or the continuity of the film. Ellipsometry can also be used to measure film thickness but, again, this works best for thicker, continuous films. In order to determine the growth rate of crystallites and the number of cycles necessary to form a continuous film, transmission electron microscopy can be used. This needs careful and time-consuming sample preparation and cannot be done on large samples.

Nanocrystalline films exhibit optical behaviour which differs from that of the bulk macrocrystalline material. This is predominantly due to quantum confinement (QC) effects [10] which come into play for crystallite diameters less than the Bohr radius. These effects have been reviewed by Trindade for a variety of semiconductors [11]. The optical absorption edge provides a simple way of observing these effects since QC causes it to be shifted to shorter wavelengths. Previous work [12] has shown that in thin titanium dioxide layers grown by ALD, the film thickness could be correlated with the effective quantum dimension calculated from the bandgap shift caused by QC. The band edge was estimated using the extinction coefficient data obtained by spectroscopic ellipsometry (SE). The current paper shows that measurement of the combination of thin film thickness and surface roughness by SE can not only measure the parameters of continuous films but can also detect the presence of discontinuous films composed of nanocrystallites. It identifies the number of ALD cycles at which the isolated crystallites combine into a continuous film and shows that the crystallite size and surface density can be obtained in this initial growth regime. The optical bandgap is estimated from the increase in extinction factor at short wavelengths and, once the bandgap is known, the crystallite diameter can be estimated from theoretical considerations. Using this calculated diameter, in a process explained below, we can estimate the crystallite density on the substrate and find how it varies with the number of ALD cycles.

This technique is applied to the nucleation and growth of ALD titanium dioxide on as-received silicon covered with a native oxide layer or on silicon which has been subject to a DBD treatment in air. The crystallite size and density and the number of cycles necessary to create a continuous film are compared between the two surface treatments.

2. Materials and methods

The substrates were Czochralski-grown boron-doped, single-side polished wafers of ⟨1 0 0⟩ silicon, obtained from Si-Mat (Germany). The silicon wafers were cut into approximately 15×15 mm samples and cleaned using an ultrasonic bath with acetone, isopropanol and deionized water consecutively, each with a time of 300 s. After cleaning, the substrates were dried using compressed air. Some were subject to a dielectric barrier discharge treatment in an ambient air atmosphere. In this case, a Diffuse Coplanar Surface Barrier Discharge (DCSBD) [13] type of dielectric barrier discharge was used. The DCSBD consists of many parallel stripline electrodes (1.5 mm in width; 1 mm in interelectrode gap) embedded in 96% alumina and is powered with peak to peak voltage up to 20 kV at frequencies from 14 kHz up to 18 kHz. The unique properties of DCSBD are based on generation of a visually diffuse low-temperature, nonthermal plasma with high power density up to 100 W cm^{-3} [14]. The plasma is generated in an approximately 0.3 mm thick layer on the surface of the dielectric ceramic. The DCSBD plasma source is described in more detail in Ref. [2]. The treatment of the silicon samples by DCSBD plasma was performed in a dynamic treatment mode, where the sample was moved through the plasma layer above the dielectric surface with defined speed and distance from the ceramic. The dynamic regime should provide homogeneous and uniform plasma treatment. The dynamic treatment system used is shown in Fig. 1. The power supplied to the DCSBD plasma system was 300–310 W equivalent to approximately 1.5 W cm^{-2}. The silicon samples were plasma treated for 5 s while the distance between the sample surface and the top of the ceramic surface was approximately 0.3 mm. The plasma treatment of silicon samples was carried out directly before they were loaded into the ALD system. These samples are identified in this paper as 'plasma treated' samples. The other samples without plasma treatment are labelled as 'untreated'. There are no other differences between these two types of samples.

The ellipsometry was carried out using a J.A. Woollam M-2000UI spectroscopic ellipsometer in the wavelength range of 210–1500 nm at angles of incidence of 65°, 70° and 75°. The data were analysed using WVASE software. The ellipsometric properties of the plasma treated and untreated silicon were measured after subjecting them to the same conditions as they would undergo before the start of the ALD process. That is, they experienced the same thermal history. They were also exposed to one cycle of the ALD process to ensure as far as possible that they replicated the properties of the substrate before any significant film growth. The ellipsometric properties of the substrates were then carefully measured to obtain accurate parameters for film thickness, optical parameters, etc. This is necessary if reliable measurements of deposited film thickness, roughness and optical constants are to be obtained. The process is described in more detail in Appendix A.

The titanium dioxide films were deposited using $TiCl_4$ (99.0% Fluka) and deionized water precursors in a Beneq TFS 500 ALD reactor. The reaction temperature was 350 °C and the pulse lengths of $TiCl_4$ and H_2O were 0.6 s and 0.25 s, respectively. Nitrogen (99.999%) was used as a carrier and purge gas with purging time 1 s after $TiCl_4$ exposure and 0.5 s after H_2O exposure. The chamber pressure was $\sim 2 \times 10^2$ Pa.

3. Results and discussion

The thickness of the ALD TiO_2 films appears to be a linear function of the number of ALD cycles, as expected. This is shown in Fig. 2a and b for the plasma treated and untreated samples, respectively. The roughness of the samples is also approximately a linear function of the number of cycles and is approximately 10% of the film thickness. However, if the graphs are expanded to look in more detail at the initial growth region there are some interesting features. Fig. 3a and b show the initial growth region.

No film growth can be detected for 3 (5) cycles for plasma treated (untreated) substrates. After growth begins, the ellipsometric modelling shows that the film thickness is zero and the roughness is greater than zero. This is consistent with there being no complete film formation on the substrate and growth taking place in isolated islands. The roughness increases with the number of cycles as would be expected if the islands were growing larger. An alternative explanation would be that there were a larger number of isolated islands being formed. The model for the surface roughness layer cannot distinguish between these two situations since it is based on an effective medium approximation which is 50% void and 50% film material. It is not possible to decouple the thickness and void content of this layer since they are correlated in the model fitting. It is clear, however, that there is no coherent film formation until between 50 and 100 ALD cycles have taken place. After this period, when the islands have coalesced to form a continuous

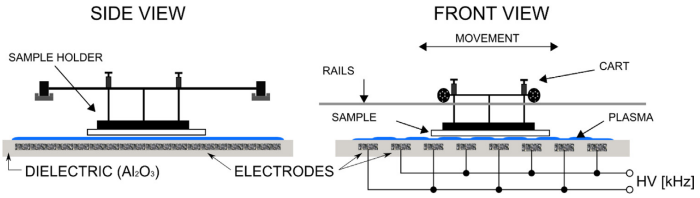

Fig. 1. Scheme of experimental apparatus for plasma treatment of silicon substrates.

layer, the thickness and roughness grow linearly (Frank–van der Merwe growth). There are only minor differences in the growth behaviour between the plasma treated and untreated samples. The plasma treated samples appear to take rather longer to achieve continuity in the film than the untreated with the roughness growing to larger values. This may perhaps be due to the fact that more material is needed to cover a rougher surface but there are insufficient data to come to any firm conclusion. There is also a difference between the thicknesses of the native oxide on the untreated and the plasma treated silicon. In the untreated samples, the native oxide has a thickness of ~2.1 nm whereas in the plasma treated samples it is thicker at ~3.5 nm. This is to be expected since exposure to an energetic oxidising atmosphere will cause an increase in native oxide thickness. The thickness of native oxide on silicon for different plasma treatment times in the range 1–60 s is plotted in Fig. 4. Plasma treatment parameters (except for time) were the same as for the ALD experiment.

The existence of isolated islands can also be detected from the parameters of the ellipsometric model for the TiO_2 film. The absorption edge, obtained as detailed in the Appendix A, for the TiO_2 measured for the thicker films was 3.31 eV which is in the range typically found for anatase films [15]. XRD measurements revealed all TiO_2 films grown on silicon at 350 °C with thickness >5 nm had the anatase phase. With thinner films, the intensity of the reflections was too low to indicate their crystallinity. However, measurements on TiO2 nanoparticles have shown that the anatase structure is maintained down to diameters of <2 nm [16,17] The absorption

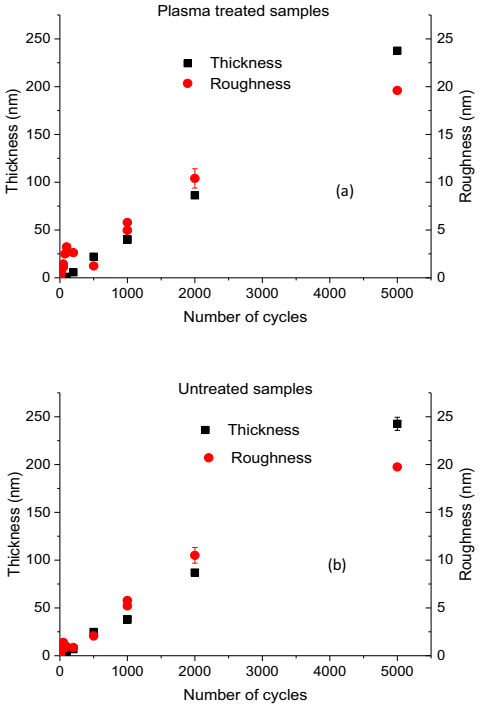

Fig. 2. Film thickness and roughness v. no. of ALD cycles, (a) plasma treated, (b) untreated samples. Note: Some error bars are not visible because the range is smaller than the data symbol.

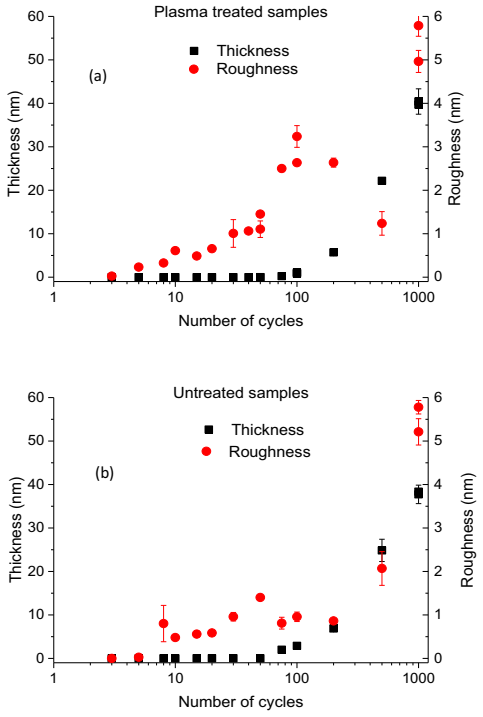

Fig. 3. Initial growth region, (a) plasma treated (b) untreated. Note: Some error bars are not visible because the range is smaller than the data symbol.

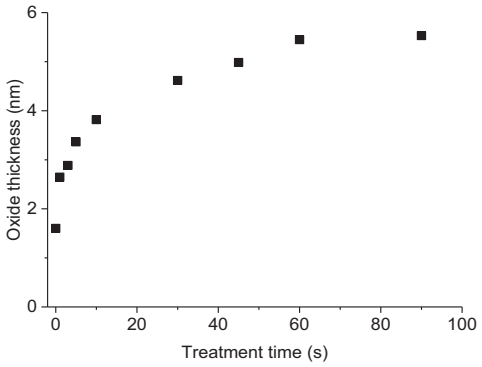

Fig. 4. The thickness of native oxide on silicon after the plasma treatment for different plasma exposure times.

edge of the TiO_2 increased in energy for the films where the growth occurred in isolated islands with no continuous film thickness, that is, for films grown with less than ~50 ALD cycles. This is shown in Fig. 5 for both plasma treated and untreated substrates. This is consistent with the effects of quantum confinement (QC) in the isolated islands. Initially, the islands will be very small giving a very large blue shift in bandgap due to the QC. This effect has previously been studied in TiO_2 [17]. The dependence of the absorption edge shift on the size of the nanocrystals is given by the effective mass model [18,19]. The increase in bandgap due to finite crystallite size is given by equation (1) [15] [20], adjusted for SI units and crystallite diameter rather than radius.

$$\Delta E_g = \frac{h^2}{2D^2 m_o}\left[\frac{1}{m_e^*} + \frac{1}{m_h^*}\right] - \frac{3.6e^2}{4\pi\varepsilon_o\varepsilon_r D} \quad (1)$$

where h is Planck's constant, m_o is the electron mass, $m_e{}^*$, $m_h{}^*$ are the effective electron and hole masses, respectively, e is the electronic charge, ε_o is the permittivity of free space, ε_r is the relative permittivity and D is the crystallite diameter. Pellegrini et al. have shown that the effective mass model corresponds well to experimental observations [21]. Yoffe [22] has stated that it is valid to use the bulk parameters in modelling even for crystallite diameters as small as 7 Å therefore taking the values given by Kormann [23] for

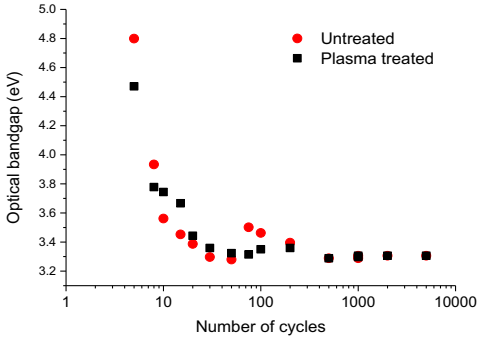

Fig. 5. Optical bandgap of the TiO_2 films as a function of the number of ALD cycles. Note: The estimated error bars are smaller than the data symbols.

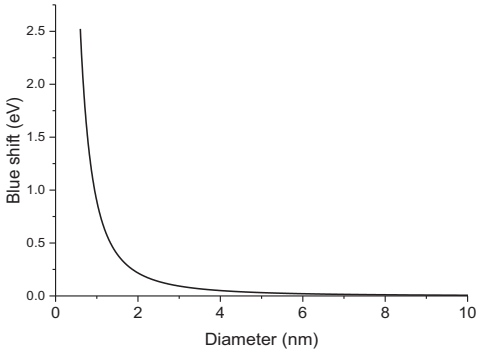

Fig. 6. Calculated bandgap blue shift as a function of the crystallite radius.

the reduced effective mass of the exciton in TiO_2 of 1.6 m_o and the optical dielectric constant of anatase of 5.6 [24], the relationship between the bandgap shift and the effective crystallite diameter can be obtained. This calculation holds for spherical crystallites. In the case of nuclei growing on a flat substrate, the shape will be hemispherical or hemi-ellipsoidal. The bandgap shift will depend on the shape and also the surface curvature, e.g. [25]. There are conflicting conclusions on this. For hemi-ellipsoids of constant volume, in some cases, the more nonspherical the shape, the greater the bandgap shift predicted [10,26]. In contrast other calculations have shown essentially no difference in behaviour between constant-volume crystallites of spherical, cubical and rectangular shape [22]. Therefore, in this case, for simplicity, we have ignored any possible effects of the crystallite shape and used the equivalent sphere model [10] where the sphere has the same volume as the hemispherical nucleus. The radius of the equivalent sphere is $1/\sqrt[3]{2}$ times the radius of the hemispherical crystal. The value of dielectric constant to be used in equation (1) is not clear since several authors have suggested that it decreases as the diameter is reduced [22]. However, this variation has been ignored since it is very difficult to quantify and the changes in magnitude of the blue shift are not excessively sensitive to the dielectric constant. Experimental observations of bandgap shift have also shown very good agreement with pseudopotential calculations [27].

The relation between the optical gap and the spherical crystallite diameter calculated from equation (1) is plotted in Fig. 6. From this curve, the hemispherical crystallite size as a function of the number of ALD cycles can be plotted (Fig. 7). This shows that the island size increases linearly until a coherent film starts to form on the substrate. Above ~75 cycles, the difference between the bulk bandgap and the crystallite bandgap taking QC into account is very small which leads to excessive uncertainty in the calculated size. The calculations of crystal size from quantum confinement effects is compared with those estimated from AFM measurements, shown in Fig. 8. The sizes of the crystallites from the AFM measurements were calculated by taking the maximum width of individual crystallites from line scans across the sample. The values of crystallite width obtained by simply drawing a constant height line across the profile can give an underestimate of the size if the top surface does not reach an even height all across the film. The larger diameter of the crystallites measured by AFM compared with the diameters calculated from the blue shift indicates that the crystallites are not strictly hemispherical and their height is less than their radius. Thus their effective diameter is smaller and they give the blue shift corresponding to smaller crystallites.

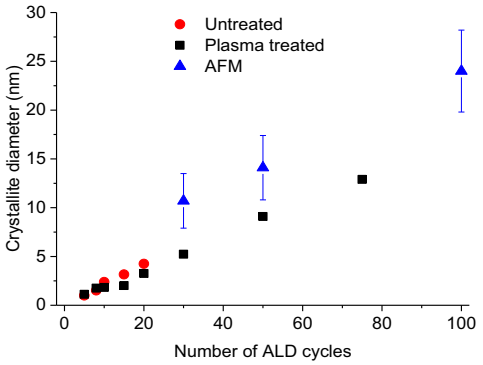

Fig. 7. Crystallite diameter as a function of number of ALD cycles. The error bars shown on the AFM data points are estimates from the AFM image.

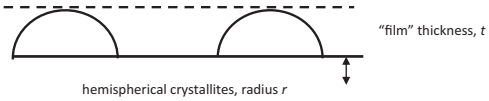

Fig. 9. Model of surface 'film' thickness equal to crystallite radius.

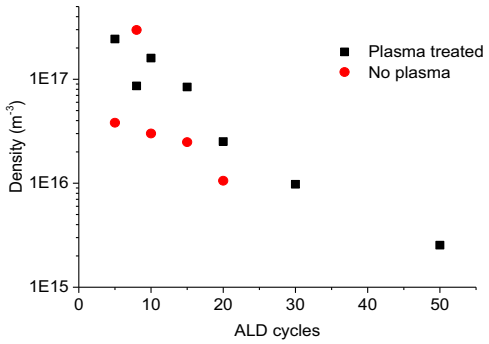

Fig. 10. Surface density of crystallites as a function of the number of ALD cycles. See note in text regarding error bars.

The surface roughness as measured by ellipsometry is also influenced by the crystallite size. However, as mentioned previously, the roughness values obtained from the fitting cannot be used directly. The surface roughness layer material model (srough.mat) assumes a mixed layer with 50% film material and 50% void. The roughness and void fraction are totally correlated so they cannot be separated without further information. However, if it is assumed that the crystallites are hemispherical, the diameter of the crystallites can be calculated from the optical extinction coefficient. The analysis assumes that the crystallites form a 'film' whose thickness is the height of the hemispheres as shown in Fig. 9. The void fraction can then be allowed to vary to give the best fit, everything else being held constant. If the crystallite diameter and void fraction are known, the density of crystallites on the surface of the substrate can be calculated as described in Appendix B. The plot of crystallite density v. number of ALD cycles is shown in Fig. 10. There is little difference between the densities on plasma treated and untreated substrate. The density as the crystallites grow appears to fall from an initial value of around $3–4 \times 10^{17}$ m^{-3} to approximately $2–3 \times 10^{15}$ m^{-3} as growth proceeds. The errors in these data are hard to estimate since the values are a consequence of the modelling process and their accuracy depends on both the ellipsometric measurements and the robustness of the model, therefore, no error bars are shown. Nevertheless, the data show a consistent trend. This reduction in density is probably due to the preferential growth of larger crystallites at the expense of the smaller due to Ostwald or similar ripening or diffusion [28,29]. These values are comparable with the density of crystallites in the range of 10^{16} m^{-3} seen in ALD deposited Pt films [30]. The density on plasma treated substrates appears to be somewhat higher. This follows the slightly lower crystallite size seen in Fig. 7.

The growth rate of the crystallite diameter from Fig. 7 is approximately 1.7 Å cycle^{-1}. If each successive layer can be considered to uniformly coat the crystallite, this corresponds to a film growth rate of 0.85 Å cycle^{-1}. This contrasts with a growth rate of ~0.5 Å cycle^{-1} measured from the thicker films in Fig. 2. The difference can be explained by the decrease in crystallite density as growth proceeds. The crystallites are growing not only by direct deposition on the surface but also by accumulation of material from smaller crystallites by the ripening process.

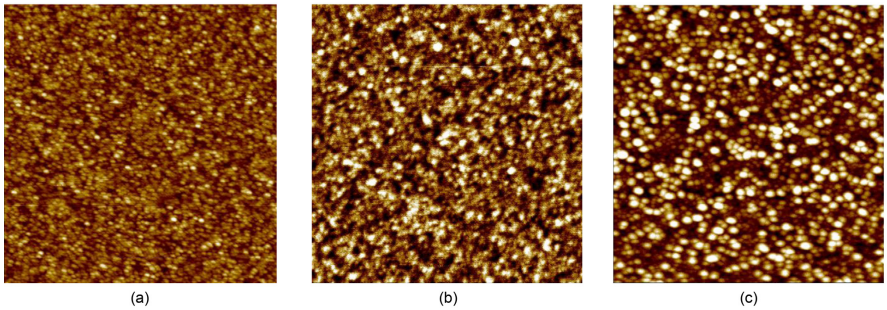

Fig. 8. AFM images of films grown for (a) 30 cycles, (b) 50 cycles and (c) 100 cycles. All scans are 0.5×0.5 μm.

4. Conclusions

We have shown that spectroscopic ellipsometry is an effective means of measuring the initial growth process in ALD layers of titanium dioxide on silicon substrates. By careful measurement of the parameters of the substrate material and the combined substrate–film combination, the point where a continuous film is formed can be determined. Approximately, 50 cycles are needed for untreated silicon and 80 cycles for plasma treated silicon. Fitting of the optical parameters of the ALD layer shows that in the region before the formation of a continuous film, the evolution of the size of the individual crystallites on the substrate can be determined by the quantum confinement effect on their optical absorption. This gives values consistent with AFM measurements. The density of crystallites on the surface can be determined if the ellipsometric modelling includes a surface layer with a thickness equal to the radius of the hemispheres and with adjustable void fraction. This shows that the initial crystallite density of $\sim 3 \times 10^{17}\,m^{-3}$ reducing to $\sim 3 \times 10^{15}\,m^{-3}$ at the point where a continuous film is formed. This is probably due to competitive growth with the larger crystallites growing at the expense of the smaller by a process of Ostwald ripening. The growth rate of crystallites calculated from the QC is consistent with the expected growth rate by the addition of ALD layers on their surface with additional crystallite growth by ripening.

Treatment of the silicon substrates in a diffuse coplanar dielectric barrier discharge with an air atmosphere increases the thickness of the native oxide from ~2 nm for the untreated silicon to up to ~6 nm depending on the treatment time but has only a minor effect on the subsequent atomic layer deposition of titanium oxide films.

Acknowledgements

This work was supported by the programme "Employment of Newly Graduated Doctors of Science for Scientific Excellence" (CZ.1.07/2.3.00/30.0009) co-financed from the European Social Fund and the state budget of the Czech Republic, by the project CZ.1.05/2.1.00/03.0086 funded by European Regional Development Fund and project LO1411 (NPU I) funded by the Ministry of Education, Youth and Sports of Czech Republic.

Appendix A.

Ellipsometric modelling has to be done very carefully, particularly where small differences and subtle changes take place. The process used here was designed to minimise any uncertainties and errors in the fitting and to eliminate artefacts in the results, as far as possible. All results were obtained by coupled fitting of generally six measurements over two different samples for each category of film. Occasionally, only four or five measurements were used. The thickness and roughness measurements were averages taken over the six measurements. Films of different thickness were deposited in separate runs with the appropriate number of cycles and in some cases repeat depositions were carried out to confirm the results. Measurements were taken from a total of 64 samples. The error bars are the standard deviations of the measurements. The procedure was as follows:

1. Initial ellipsometric measurements were carried out on the silicon substrates after they were cleaned. The Si_jaw.mat and thermal_SiO2.mat ellipsometric models from the WVASE software models were used to get the best thickness fit for the native oxide. The oxide thickness was then fixed and the n and k values of the Si were allowed to vary to obtain the best fit. These new Si parameters were saved as a new silicon material model.
2. Using the untreated sample, with the new Si material model substrate parameters, the n and k of the oxide were varied to get the best fit. The oxide parameters were saved as a new material model for oxide on untreated Si.
3. A similar procedure was carried out for the plasma treated sample to give a material model for the oxide on plasma treated Si.
4. Using both the plasma treated and untreated substrates and their appropriate oxide parameters, the 5000 cycle TiO_2 films were simulated using the TiO2_tl.mat Tauc-Lorentz material model, with the appropriate silicon oxide values for plasma treated or untreated samples and the thickness of the TiO_2 layer was varied for the best fit.
5. The Tauc-Lorentz parameters of the TiO_2 were then also varied to get the best fit and these were used as the basis material for further TiO_2 modelling. The TiO_2 thickness was also allowed to vary simultaneously with its n and k values.
6. The substrates were heated up in the reaction chamber. To allow for any changes which the predeposition process might make to the native oxide thickness, samples with only one ALD cycle were grown and used as a baseline with the assumption that there was effectively minimal growth.
7. The samples had TiO_2 deposited with various numbers of ALD cycles. To obtain the best fitting of the TiO_2 parameters, the modelling was done as follows. A layer stack was used comprising Si substrate, native silicon oxide layer (using the model for plasma treated or untreated oxide as appropriate), TiO_2 layer and surface roughness layer. The surface roughness layer was 50% TiO_2 and 50% void. This composition had to be kept fixed since it is completely correlated with the roughness value. The Si, the native oxide parameters and the TiO_2 parameters were kept fixed but the thicknesses of the native oxide, TiO_2 and surface roughness layers were allowed to vary. Once the best fit had been obtained, the parameters of the absorption peaks in the Tauc-Lorentz model for the TiO_2 were then also allowed to vary to refine the fitting.
8. The optical band edge of the TiO_2 film was taken as the energy at which its k value reached the arbitrary value of 0.005. The absorption rose very steeply for energies above this value of k, therefore, the value of band edge energy obtained from this was not very sensitive to the exact choice of absorption level chosen

Appendix B.

If the hemispherical crystallites are evenly distributed across the surface of the substrate as shown in Fig. 11, their surface density is given by $\sigma = \frac{2}{d^2\sqrt{3}}$. d can be calculated as follows:

The volume of one hemisphere is given by $V_h = \frac{2}{3}\pi t^3$. If we consider that a square substrate with sides l and effective thickness t represents the thin film (which may have a certain void content), the effective volume of the film $V_f = l^2 t$. The number of hemispheres covering the substrate surface is given by $n_h = \frac{l^2 2}{d^2\sqrt{3}}$. The total volume of hemispheres contained in the volume of the film is

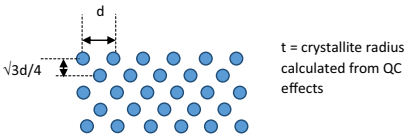

Fig. 11. Regular arrangement of crystallites on the surface of the substrate.

$V_T = n_h V_h = \frac{4\pi}{3\sqrt{3}} \cdot \frac{l^2 t^3}{d^2}$. Therefore, the fill factor $f = \frac{V_T}{V_f} = \frac{4\pi}{3\sqrt{3}} \frac{t^2}{d^2}$. Therefore, $d^2 = \frac{4\pi}{3\sqrt{3}} \frac{t^2}{f}$ and the hemisphere areal density, σ, is then given by $\sigma = \frac{3}{2\pi} \frac{f}{t^2}$.

References

[1] O. Goosens, E. Dekempeneer, D. Vangeneugden, R. Van de Leest, C. Leys, Application of atmospheric pressure dielectric barrier discharges in deposition, cleaning and activation, Surf. Coat. Technol. 142–144 (2001) 474.

[2] Z. Fang, X. Qiu, Y. Qiu, E. Kuffel, Dielectric barrier discharge in atmospheric air for glass-surface treatment to enhance hydrophobicity, IEEE Trans. Plasma Sci. 34 (2006) 1216.

[3] U. Kogelschatz, Dielectric-barrier discharges: their history, discharge physics, and industrial applications, Plasma Chem. Plasma Process. 23 (2003) 1.

[4] S.M. George, A.W. Ott, J.W. Klaus, Surface chemistry for atomic layer growth, J. Phys. Chem. 100 (1996) 13121.

[5] E.S. Brandt, J.M. Grace, Initiation of atomic layer deposition of metal oxides on polymer substrates by water plasma pretreatment, J. Vac. Sci. Technol. A 30 (2012) 01A137.

[6] S.B.S. Heil, P. Kudlacek, E. Langereis, R. Engeln, M.C.M. van de Sanden, W.M.M. Kessels, *In situ* reaction mechanism studies of plasma-assisted atomic layer deposition of Al2O3, Appl. Phys. Lett. 89 (2006) 131505.

[7] Y. Lu, A. Kobayashi, H. Kondo, K. Ishikawa, M. Sekine, M. Hori, Chemical reactions during plasma-enhanced atomic layer deposition of SiO_2 films employing aminosilane and O_2/Ar plasma at 50 C, Jpn. J. Appl. Phys. 53 (2014) 010305.

[8] H.B. Profijt, S.E. Potts, M.C.M. van de Sanden, W.M.M. Kessels, Plasma-assisted atomic layer deposition: basics, opportunities, and challenges, J. Vac. Sci. Technol. A 29 (2011) 050801.

[9] R. Puurunen, W. Vandervorst, Island growth as a growth mode in atomic layer deposition: a phenomenological model, J. Appl. Phys. 96 (2004) 7686.

[10] G. Cantele, D. Ninno, G. Iadonisi, Confined states in ellipsoidal quantum dots, J. Phys.: Condens. Matter 12 (2000) 9019.

[11] T. Trindade, P. O'Brien, N. Picket, Nanocrystalline semiconductors: synthesis, properties, and perspectives, Chem. Mater. 13 (2001) 3843.

[12] D.M. King, X. Du, A.S. Cavanagh, A.W. Weimer, Quantum confinement in amorphous TiO_2 films studied via atomic layer deposition, Nanotechnology 19 (2008) 445401.

[13] M. Černák, Apparatus and method for cleaning, etching, activation and subsequent treatment of glass surfaces, glass surfaces coated by metal oxides, and surfaces of other SiO-coated materials, Patent WO 2007142612 (2007).

[14] M. Černák, D. Kováčik, J. Rahel, P. St'ahel, A. Zahoranová, J. Kubincová, A. Tóth, L. Černáková, Generation of a high-density highly non-equilibrium air plasma for high-speed large-area flat surface processing, Plasma Phys. Cntr. F 53 (2011) 124031.

[15] T. Bak, J. Nowotny, M. Rekas, C. Sorrell, Defect chemistry and semiconducting properties of titanium dioxide: I. Intrinsic electronic equilibrium, J. Phys. Chem. Solids 64 (2003) 1043.

[16] N. Satoh, T. Nakashima, K. Kamikura, K. Yamamoto, Quantum size effect in TiO_2 nanoparticles prepared by finely controlled metal assembly on dendrimer templates, Nature Nanotechnol. 3 (2008) 106.

[17] V. Luca, Comparison of size-dependent structural and electronic properties of anatase and rutile nanoparticles, J. Phys. Chem. C 113 (2009) 6367.

[18] L. Brus, Electronic wave functions in semiconductor clusters: experiment and theory, J. Phys. Chem. 90 (1986) 2555.

[19] C.J. Sandroff, S.P. Kelty, D.M. Hwang, Clusters in solution: Growth and optical properties of layered semiconductors with hexagonal and honeycombed structures, J. Chem. Phys. 85 (1986) 5337.

[20] L. Schoonman, Nanoionics, Sol. State Ionics 157 (2003) 319.

[21] G. Pellegrini, G. Mattei, P. Mazzoldi, Finite depth square well model: applicability and limitations, J. Appl. Phys. 97 (2005) 073706.

[22] A.D. Yoffe, Semiconductor quantum dots and related systems: electronic, optical, luminescence and related properties of low dimensional systems, Adv. Phys. 50 (2001) 1.

[23] C. Kormann, D.W. Bahnemann, M.R. Hoffmann, Preparation and characterization of quantum-sized titanium dioxide, J. Phys. Chem. 92 (1988) 5196.

[24] H. Wemple, Optical oscillator strengths and excitation energies in solids, liquids, and molecules, J. Chem. Phys. 67 (1977) 2151, cited in S. Mo and W. Y. Ching, Phys. Rev. B, 51, p.13023, 1995.

[25] M.A. Cusack, P.R. Briddon, M. Jaros, Absorption spectra and optical transitions in InAs/GaAs self-assembled quantum dots, Phys. Rev. B 56 (1997) 4047.

[26] H. Leon, J. Marın, R. Riera, Excitonic and electronic states in ellipsoidal and semiellipsoidal quantum dots, Physica E 27 (2005) 385.

[27] A. Tomasulo, M.V. Ramakrishna, Quantum confinement effects in semiconductor clusters II, J. Chem. Phys. 105 (1996) 3612.

[28] Z. Zhang, M.G. Lagally, Atomistic processes in the early stages of thin-film growth, Science 276 (1997) 377.

[29] W. Ostwald, Stoichiometrie und verwandtschaftslehre, Z. Phys. Chem. 34 (1900) 495.

[30] M.J. Weber, A.J.M. Mackus, M.A. Verheijen, V. Longo, A.A. Bol, W.M.M. Kessels, Atomic layer deposition of high-purity palladium films from Pd(hfac)2 and H2 and O2 plasmas, J. Phys. Chem. C 118 (2014) 8702.

Publication III

Ivanova T.V., Toivonen J., Homola T., Maydannik P.S., Kääriäinen T., Sillanpää M., Cameron D.C.
Atomic Layer Deposition of Cerium Oxide for Potential Use in Diesel Soot Combustion

Reprinted with permission from
Journal of Vacuum Science & Technology A
Vol. 34, p. 031506, 2016
© 2016, AIP Publishing

Atomic layer deposition of cerium oxide for potential use in diesel soot combustion

Tatiana V. Ivanova,[a] Jenni Toivonen, Philipp S. Maydannik, Tommi Kääriäinen, and Mika Sillanpää
ASTRaL Team, Laboratory of Green Chemistry, School of Engineering Science, Lappeenranta University of Technology, Sammonkatu 12, FI-50130 Mikkeli, Finland

Tomáš Homola and David C. Cameron
R&D Centre for Low-Cost Plasma and Nanotechnology Surface Modification, Masaryk University, Kotlářská 267/2, 611 37 Brno, Czech Republic

(Received 14 October 2015; accepted 8 March 2016; published 24 March 2016)

The particulate soot emission from diesel motors has a severe impact on the environment and people's health. The use of catalytic convertors is one of the ways to minimize the emission and decrease the hazard level. In this paper, the activity of cerium oxide for catalytic combustion of diesel soot was studied. Thin films of cerium dioxide were synthesized by atomic layer deposition using tetrakis(2,2,6,6-tetramethyl-3,5-heptanedionato)cerium [$Ce(thd)_4$] and ozone as precursors. The characteristics of the films were studied as a function of deposition conditions within the reaction temperature range of 180–350 °C. Thickness, crystallinity, elemental composition, and morphology of the CeO_2 films deposited on Si (100) were characterized by ellipsometry, x-ray diffraction, x-ray photoelectron spectroscopy, atomic force microscopy, and field emission scanning electron microscopy, respectively. The growth rate of CeO_2 was observed to be 0.30 Å/cycle at temperatures up to 250 °C with a slight increase to 0.37 Å/cycle at 300 °C. The effect of CeO_2 films grown on stainless steel foil supports on soot combustion was measured with annealing tests. Based on the analysis of these, in catalytic applications, CeO_2 has been shown to be effective in lowering the soot combustion temperature from 600 °C for the uncoated substrates to 370 °C for the CeO_2 coated ones. It was found that the higher deposition temperatures had a positive effect on the catalyst performance. © *2016 American Vacuum Society*. [http://dx.doi.org/10.1116/1.4944589]

I. INTRODUCTION

The rising number of cars has resulted in a dramatic increase in air pollutants such as volatile organic compounds, nitrogen oxides, and particulate matter. This fact has led to the increased interest in the research on automotive exhaust catalysts.[1] Particulate matter is one of major contributors to environmental pollution mainly emitted by diesel engines. The hazardous nature of the diesel soot has led researchers to develop devices that can reduce soot emission and remedy the problem. The conventional approach involves a two-stage soot removal process: the use of diesel particulate filters for separation of carbonaceous particles from the gas phase is the first step; the second step is regeneration by means of burning the soot particles inside the filter. To achieve the regeneration of the filter by combustion of the collected particles, the soot must reach a minimum temperature of 600–650 °C in order to autoignite and sustain the combustion.[2] The typical exhaust gas temperature varies between 250 and 450 °C,[3] and it is not high enough for spontaneous regeneration. One way to reduce combustion temperature is using catalysts, which should be thermally stable for regeneration purposes.[4]

Various alkaline and alkaline earth metals or transition metals (Mn, Cu, V, Fe, and Co), noble metals (mainly Pt), and rare earth metals can function as catalysts and perform redox cycles during the soot combustion process.[5] The redox process disturbs the charge balance of the mixed-valence binary oxides, and electroneutrality is ensured by creation of oxygen vacancies.[6] Among various rare earth metal oxides, cerium oxide (CeO_2) has attracted much interest for soot oxidation application due to its favorable properties.[7]

Cerium oxide has a high oxygen storage capacity (OSC) value, which explains its choice for oxidation applications.[1] The OSC of cerium oxide is linked to the formation of a continuum of oxygen-deficient nonstoichiometric CeO_{2-x} oxides (with $0 < x \leq 0.5$). The capabilities of the redox couple Ce^{+3}/Ce^{+4} are strongly enhanced if other elements are introduced into the CeO_2 lattice, and also depend on the gas composition, temperature, and pressure.[7,8] The redox properties of CeO_2 provide the good catalytic performance of cerium oxide as a soot combustion catalyst in the exhaust filter and has been shown to reduce the temperature of the burn-off of soot down to 450–400 °C.[9–12]

Various techniques such as precipitation,[13] solution combustion synthesis,[14] chemical vapor deposition,[15] solvothermal synthesis,[16] electrodeposition,[17] sol–gel techniques,[18] and atomic layer deposition (ALD)[19–22] have been reported for the synthesis of CeO_2 material. Among these methods, ALD is a technology able to produce ultrathin and highly conformal catalytic coatings on high-aspect ratio structures.[23] The thickness of the films can be easily controlled by controlling the number of deposition cycles. Because of its ability to coat 3D structures, ALD can be easily used to

[a]Electronic addresses: tatiana.ivanova@lut.fi; ivanova.tatyana.v@gmail.com

RIGHTSLINK

deposit catalytic coatings on geometrically complex particulate filters and traps in diesel engine exhaust systems and may open the possibility of new filter designs, which are not possible with the existing technologies.

ALD has been employed previously to deposit CeO_2 thin films as a buffer layer using $Ce(thd)_4$ and $Ce(thd)_3$phen precursors with O_3 as a source of oxygen.[19] Our research work reports the synthesis of CeO_2 ALD thin films, which were applied for catalytic application. A series of CeO_2 catalysts has been prepared by ALD and characterized by means of scanning electron microscope (SEM), AFM, XPS, and XRD. The studies have mainly focused on the pursuit of the optimal ALD parameters for cerium oxide deposition, such as deposition temperature, and on exploring the influence of the structural properties of CeO_2 on soot decomposition. The catalytic activity of CeO_2 has been studied with annealing tests on soot-covered surfaces.

II. EXPERIMENT

A. Catalyst preparation

The deposition of cerium oxide was carried out using an F-120 ALCVD reactor (ASM Microchemistry, Ltd., Espoo). $Ce(thd)_4$ [2,2,6,6-tetramethyl-3,5-heptadionatecerium $Ce(C_{11}H_{19}O_2)_4$] provided by Volatec (Porvoo) and ozone (O_3) were used as precursors. Ozone was generated by an ozone generator (Wedeco Modular 4HC Lab, Herford, Germany) from a pure oxygen (>99.999%) source with a concentration of ~120 g/m^3. The pressure in the reactor was approximately 1 mbar. $Ce(thd)_4$ was evaporated at 160 °C and delivered to the reactor by N_2 carrier gas (>99.999%). N_2 was also used as the purge gas between precursor pulses. The pulse time for $Ce(thd)_4$ was varied from 0.5 to 4 s in 0.5 s steps while keeping the O_3 pulse time constant at 2.5 s. After finding the optimal pulse time for $Ce(thd)_4$, the pulse time for O_3 was determined with the same method. The purge time was 2.5 s after each precursor pulse. The deposition temperatures 180, 200, 250, 300, and 350 °C were studied with films deposited with 2000 ALD cycles.

Silicon substrates ⟨100⟩ (Si-Mat, Germany) were used for process development while stainless steel foil AISI 316 with a thickness of 0.025 mm (Goodfellow Cambridge, Ltd., London, UK) was applied for soot burning tests. The substrates were cut into pieces of 30 × 10 mm and cleaned using an ultrasonic bath with acetone, isopropanol, and deionized water consecutively, each with a time of 5 min. After cleaning, the substrates were dried using compressed air.

B. Soot deposition system

A schematic diagram of the soot deposition system is presented in Fig. 1. Soot was generated with a custom-made system, which uses diesel Webasto engine preheater to generate particulate matter. This approach should fairly closely simulate the soot formation process that occurs in the diesel engine and its build up in the exhaust system. Diesel fuel and air were injected into the combustion chamber of the Webasto with an internal blower. Once the fuel was burned

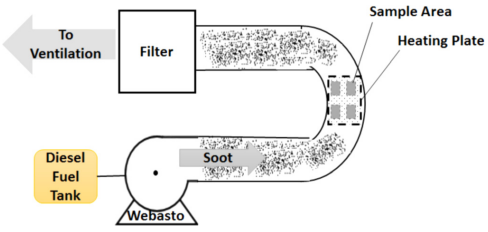

FIG. 1. (Color online) Schematic diagram of the soot deposition system.

in the chamber, its exhaust gases flowed through the pipe connected to the filter unit. The pipeline has a U-shape with a hole in the middle where samples are placed. The sample in turn sits on a heating plate with the temperature of 100–120 °C in order to prevent water condensation on the sample surface during the soot deposition process. The samples were exposed to exhaust gases for 1.5 min and the amount of accumulated soot was measured by weighing the samples prior and after the soot deposition.

C. Catalyst characterization

CeO_2 film thickness was measured by J.A. Woollam M-2000UI spectroscopic ellipsometer (J.A. Woollam Co., Lincoln, USA). A Cauchy model was used to fit the experimental data.

The microstructure of the cerium oxide thin films was evaluated with field emission SEM Hitachi S-4800 (Hitachi, Tokyo, Japan). The film morphological features such as roughness and cluster size were measured by AFM using a Park NX10 (Park Systems, Suwon, South Korea) in noncontact mode with a cantilever force constant of 42 N/m.

The crystal structure of the coatings was studied by a Rigaku SmartLab® Type F XRD (Cu-K_α radiation, $\lambda = 1.5418$ Å). The grazing incidence x-ray diffraction scan was collected with a grazing incidence angle of 0.5°. Scan speed of 1.5°/min and 2θ values from 20° to 90° were used.

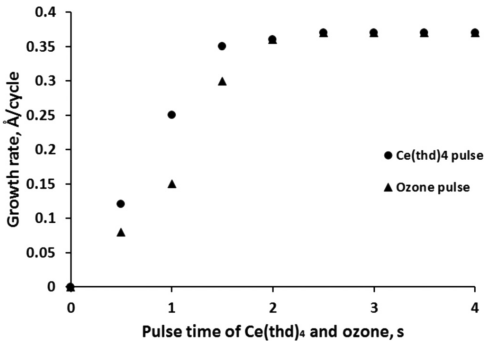

FIG. 2. Effect of $Ce(thd)_4$ and ozone pulse time on the growth rate of cerium oxide at 300 °C of reactor temperature.

RIGHTSLINK

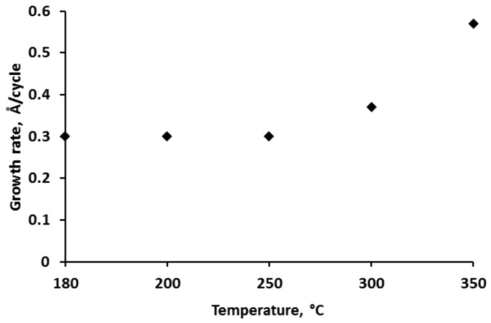

FIG. 3. Growth rate of cerium oxide film as a function of deposition temperature (2000 cycles).

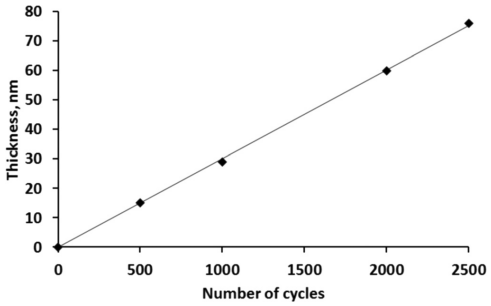

FIG. 4. Thickness of the cerium oxide film as a function of the number of deposition cycles at the deposition temperature of 200 °C.

The chemical bonding properties and impurity concentration in the synthesized films were investigated by XPS using an ESCALAB 250Xi (Thermo Scientific, UK) with a monochromated Al-K_α (energy of 1486.7 eV) x-ray source in the constant pass energy mode with a value of 50 eV. For high resolution spectra of Ce 3d, a pass energy of 20 eV with a resolution 0.1 eV was used. Compensation of charging by an electron flood source was used in all measurements to minimize binding energy shifts. The binding energy of C1s (284.5 eV) was taken as an internal standard for calibration. The XPS carbon data were obtained after removing the surface layer of the thin film by sputtering with Ar^+ ions at 2 kV for 20 s. The AVANTAGE software was used for deconvolution and curve fitting using 70:30 Gaussian–Lorentzian peaks with Smart type background.

D. Catalytic activity

In order to evaluate catalytic activity, five samples with CeO_2 catalytic coating were separately prepared using stainless steel foil as substrates for each deposition temperature. The catalyst/soot mass ratio was approximately 1:6, which corresponds to a CeO_2:C molar ratio of approximately 1:86. The average mass of soot was approximately 0.5 mg on each sample. Annealing tests were performed by placing the samples into an oven and measuring the weight loss of the samples. The overall test duration was 4 h with intermediate weight loss measurement 2 h after the beginning of the test. Catalytic activity of the films was evaluated in the temperature range of 350–490 °C in ambient atmosphere. The catalytic response of all CeO_2 samples was recorded three times in succession to evaluate the soot decomposition mechanism and the reproducibility of the prepared catalysts.

III. RESULTS AND DISCUSSION

A. Cerium oxide deposition

In order to benefit from the unique advantages of the ALD technique, the deposition process must show self-limiting growth behavior. This can be assessed by measuring the growth rate as a function of the amount of precursor delivered into the reactor. The amount of $Ce(thd)_4$ fed into the reactor volume was adjusted by varying the pulsing time within the range of 0.5–4 s while the O_3 pulse was fixed at 2.5 s. During these experiments, the reactor temperature was kept at 300 °C. The saturation curve is shown in Fig. 2. The CeO_2 growth rate reached a constant value of 0.37 Å/cycle at 1.5 s of pulsing and did not exhibit any further increase up to 4 s of pulsing time. The same approach was used to find the optimal ozone pulsing time. Measuring the growth rate over the series of depositions revealed that film growth saturated at 2.5 s of O_3 pulsing time.

Reactor temperature is a parameter that has a great effect both on film properties and process behavior. It should be chosen so that neither condensation of the precursor nor its decomposition happens during the process. Since the Ce precursor temperature was 160 °C, reactor temperatures between 180 and 350 °C were studied and the resulting film thicknesses for 2000 ALD cycles are plotted in Fig. 3. The process provides constant growth of 0.30 Å/cycle at temperatures up to 250 °C with slight increase to 0.37 Å/cycle at

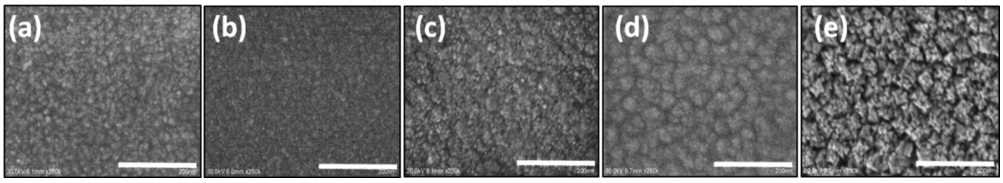

FIG. 5. SEM images of cerium oxide coated silicon wafers deposited with 2000 cycles at temperatures of (a) 180 °C, (b) 200 °C, (c) 250 °C, (d) 300 °C, and (e) 350 °C. All scale bars are 200 nm.

RIGHTSLINK

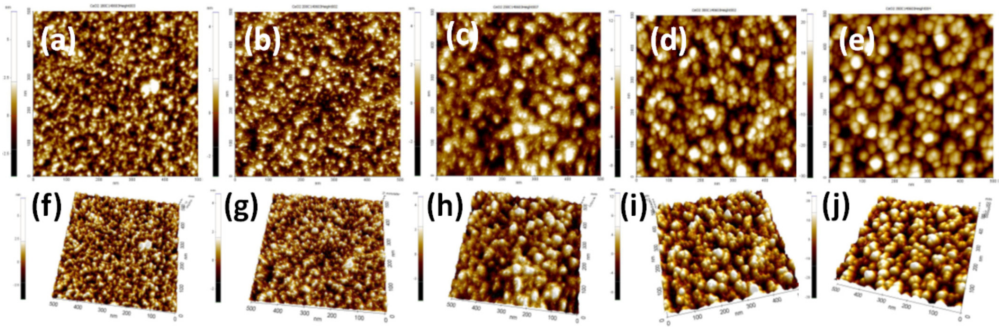

FIG. 6. (Color online) AFM images of cerium oxide deposited on silicon wafers with 2000 cycles at temperatures of [(a) and (f)] 180 °C, [(b) and (g)] 200 °C, [(c) and (h)] 250 °C, [(d) and (i)] 300 °C, and [(e) and (j)] 350 °C deposition temperatures. All scans are 0.5 × 0.5 μm.

300 °C. Further increase in temperature up to 350 °C results in almost doubling the growth rate value to 0.57 Å/cycle and can be attributed to thermal decomposition of $Ce(thd)_4$ precursor.

Figure 4 shows the CeO_2 film thickness versus the number of ALD cycles from 500 to 2500 for deposition at 200 °C. From Fig. 4, it can be seen that the thickness increases linearly. The measured growth rate of 0.30 Å/cycle is consistent with the previously reported growth rate of 0.32 Å/cycle for the $Ce(thd)_4$ and O_3 process.[19]

B. CeO_2 catalyst characterization

SEM was used to study the surface morphology of the cerium oxide film. SEM images of samples deposited at different temperatures are shown in Fig. 5.

The cerium oxide thin films comprise small crystalline clusters that change in size with the temperature. It was observed that the structure of the cerium oxide thin film deposited at 350 °C differed from the others. The deposition temperature of 350 °C was outside the ALD window, which will affect the ALD growth conditions. This phenomenon was confirmed by AFM studies (shown below).

AFM images were taken in order to study the surface morphology of the CeO_2 films. Figure 6 shows the AFM images of cerium dioxide films deposited at 180, 200, 250, 300, and 350 °C. It appears that the shape and size of the crystallites changed from an initial spherical appearance to larger and more facetted with temperature and this effect became more pronounced above 300 °C.

TABLE I. Average RMS roughness and average thickness of the cerium oxide films deposited with 2000 ALD cycles at 180, 200, 250, and 300 °C and with 1000 ALD cycles at 350 °C.

Deposition temperature (°C)	Average RMS roughness (nm)	Average thickness (nm)
180	0.98	62
200	0.8	63
250	1.4	61
300	2.5	76
350 (1000 ALD cycles)	4.3	73

Table I shows average thickness and respective surface roughness for each deposition temperature taken from the AFM measurements. Due to the fact that CeO_2 deposited at 350 °C was outside the ALD window and film thickness was as twice as much compared to lower deposition temperatures, average RMS roughness was measured at 1000 ALD cycles. This number of cycles produced the same thickness as in case of lower deposition temperatures. The roughness values are in agreement with the crystallite size seen in the SEM micrographs. It stays fairly constant at temperatures up to 250 °C with a noticeable increase at 300 °C and a sharp rise at 350 °C up to 4.3 nm. These increases happen along with the film growth rate increases as deposition temperature is raised.

XRD analysis was performed to identify the crystal structure of the cerium oxide films deposited in the temperature range of 180–350 °C. For this purpose, 2000 ALD cycles were deposited onto Si substrates, and the resulting XRD patterns are shown in Fig. 7. It can be seen that the films deposited over the entire temperature range are polycrystalline and are characteristic of the cubic fluorite structure. The

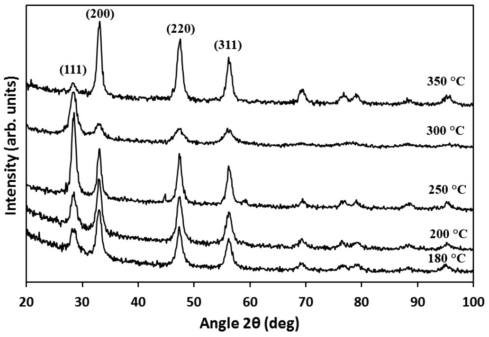

FIG. 7. XRD patterns of cerium oxide films deposited with 2000 ALD cycles at 350, 300, 250, 200, and 180 °C.

RIGHTSLINK

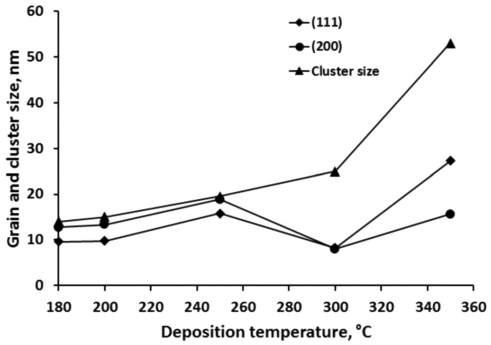

FIG. 8. Crystallite and cluster sizes of the cerium oxide film deposited with 2000 ALD cycles at 180, 200, 250, 300, and 350 °C.

diffractions peaks at 28.6°, 33.6°, 47.6°, and 56.3° of 2θ can be identified for all the samples and attributed to (111), (200), (220), and (311) planes of cubic cerium oxide, respectively (COD database, card no. 9009008). With an increase in the substrate temperature up to 300 °C, the (111) reflection becomes dominant. The different deposition temperatures affect the broadening and the relative intensities of the various XRD peaks due to the variation of grain size and orientation, respectively. No sign of crystalline Ce_2O_3 was detected by XRD in contrast to the XPS results (see below), and there is no sign of a shift in the peak positions, which might occur due to lattice strain caused by a high density of oxygen vacancies.

The mean grain size, assuming spherical grains, of CeO_2 can be determined from the full width at half maximum (FWHM) of the (111) and (200) XRD peaks, through Scherrer's equation[24]

$$\varepsilon = \frac{K\lambda}{b\cos\theta}, \tag{1}$$

where ε is the apparent grain diameter, $K = 0.9$ is Scherrer's shape factor,[25] λ is the wavelength of the radiation, b is the FWHM of the sample peak, and θ is the Bragg angle of the peak considered.

It is important to remember that Scherrer's equation is not optimal for asymmetric crystallites because the Scherrer's constant K depends on the alignment of the reflection planes with the long or short dimensions of the crystallites[26] and also on the geometric shape: cube, tetrahedron, parallelepiped, etc.[27] However, since the exact shape of the crystallites was not determined, we have assumed for simplicity that they were approximately spherical. This will not affect the general conclusions.

The grain sizes calculated from the (111) and (200) plane reflections and cluster size estimated from AFM images were plotted against the respective deposition temperatures (Fig. 8). AFM data confirm that clusters grew with temperature in a monotonic manner. The AFM data and the Scherrer's formula estimations are in good agreement up to 250 °C. Above 250 °C, the AFM measurements give a larger crystallite size, suggesting that the topographic features measured by AFM are not individual crystallites, but clusters of crystallites. The size of individual crystallites as estimated by the Scherrer equation showed a minimum at 300 °C. This smaller crystal size together with comparatively large crystallite cluster size will result in clusters with multifacetted surfaces giving a larger surface area. This may play a part in enhancing catalytic activity.

XPS analyses were made to determine the surface composition of the cerium oxide film and to verify the existence of Ce^{+4} and Ce^{+3} in the film. Ar^+ bombardment produces a considerable change in the chemical structure of the sample layer by XPS.[28] Therefore, the information about Ce^{+3} and Ce^{+4} content was obtained from the high resolution Ce 3d spectra before Ar^+ etching. C 1s and O 1s were measured after Ar^+ bombardment to exclude surface contaminations. The XPS results are summarized in Table II and demonstrate that Ce, O, and C were present in all samples. Using the values of surface atomic composition, an estimation of the O/Ce atomic ratio can be obtained. The ratio O/Ce for the cerium oxide deposited at 180, 200, 250, 300, and 350 °C is around 2, which indicates that the film primarily consists of CeO_2. The carbon impurity level is around 21 at. %, which originated from the cerium precursor.

The cerium oxide deposited at 350 °C has a higher percentage of carbon impurities, as can be seen from Table II. The ALD of cerium oxide at 350 °C is above the ALD window as determined earlier. The excess incorporation of carbon into the film indicates that during the ALD process the cerium oxide precursor $Ce(thd)_4$ decomposes at this temperature. Thus, the ALD process does not behave ideally, and this will lead to lack of accurate thickness control and sensitivity of the structure to small changes in the reactor temperature. Since the ALD behavior above the ALD window

TABLE II. Surface elemental composition of cerium oxide films deposited with 2000 ALD cycles at 180, 200, 250, 300, and 350 °C.

Deposition temperature (°C)	Surface composition (at. %)					Concentration of Ce^{4+} (at. %) (excluding C)	Concentration of Ce^{3+} (at. %) (excluding C)
	Ce3d	O1s	C1s	O/Ce (from survey)	O/Ce [Eq. (4)]		
180	25.7	53.2	21.1	2.1	1.94	87.2	12.8
200	25.9	52.9	21.3	2.0	1.94	87.1	12.9
250	26.7	52.1	21.2	2.0	1.93	86.9	13.1
300	24.8	50.3	20.2	2.0	1.91	82.6	17.4
350	23.5	49.7	26.9	2.1	1.90	79.7	20.3

RIGHTSLINK

cannot be fully predicted, the deposition temperature at 350 °C was excluded from consideration of its catalytic properties.

Figure 9 shows deconvoluted Ce 3d XPS spectra of CeO_2 deposited on Si at 250 °C. As can be seen from Fig. 9, there are ten peaks assignments within the Ce3d spectra, where U and V refer to the $3d_{3/2}$ and $3d_{5/2}$ spin–orbit components, respectively. The ratio of the U peak intensities to the V peak intensities was fixed at 2/3. The widths of the corresponding U and V peaks were fixed to be the same, and the energy separation between the corresponding U and V peaks was 18.3 (±0.15) eV.

In addition, U, U″, U‴, V, V″, and V‴ refer to Ce^{+4} final state, while U^0, U′ and V^0, V′ refer to Ce^{+3} final state. Spin–orbit peaks of U‴ and V‴ at 916.3 and 897.85 eV with 18.3 eV separation are attributed to primary photoionization from Ce^{4+} with the $Ce3d^94f^0$ $O2p^6$ final state. Lower binding energy states of U″/V″ at 906.74 and at 888.29 eV and U/V at 900.53 and 882.18 eV have been assigned to the $Ce3d^94f^1$ $O2p^5$ and $Ce3d^94f^2$ $O2p^4$ final states shake-down satellite features, respectively. Satellites are caused by the facilitation of ligand (O2p) to metal (Ce4f) charge transfer by the primary photoionization process. For Ce^{3+} peaks, the doublet U′/V′ at 902.95 and 884.73 eV corresponds to the main photoionization to the $Ce3d^94f^2$ $O2p^6$ final states; U^0/V^0 peaks at 898.45 and 880.3 eV relate to the $Ce^{3+}3d^94f^1$ $O2p^5$ final states shake-down satellites.[29] All the measured binding energies and relative integrated peak areas of Ce3d spin–orbit doublets in CeO_2 films are summarized in Table III.

For the quantitative determinations of Ce^{+3} and Ce^{+4} concentrations, we used the method that proposed by Shyu,[30] in which peak areas (A) of Ce^{+4} and Ce^{+3} components are used to estimate their relative concentrations in the films using the following equations:

$$Ce^{+3}(\%) = \frac{Ce^{+3}}{Ce^{+3} + Ce^{+4}} = \frac{A_{V_0} + A_{U_0} + A_{V'} + A_{U'}}{A_{V_0} + A_{U_0} + A_{V'} + A_{U'} + A_V + A_U + A_{V''} + A_{U''} + A_{V'''} + A_{U'''}} \times 100. \quad (2)$$

The fraction of CeO_2 can be calculated by

$$Ce^{+4}(\%) = 100\% - Ce^{+3}(\%). \quad (3)$$

The concentration of Ce^{+3} in CeO_2 deposited at different temperatures was estimated according to Eq. (2) and summarized in Table II. As can be seen, Ce in oxidation state +3 is present in the deposited films. The amount of Ce^{+3} is less in the films deposited at 180, 200, and 250 °C (about 13%) in comparison to the coatings deposited at 300 °C (17.4%). Ce^{+3} formation can be explained by reduction of Ce^{+4} by carbon which originate from precursor ligands. A correlation between the carbon and Ce^{+3} concentrations (see Table II) favors this hypothesis. XPS provides evidence that Ce_2O_3 exists in the CeO_2 films, while XRD identifies only CeO_2. Therefore, we may consider that Ce^{+3} may either exist as a Ce_2O_3 amorphous phase or because of O vacancies in CeO_2. Neto and Schmal[31] showed that Ce^{3+} species can be presented at the surface and in the bulk structure of CeO_2 prepared by the precipitation and hydrothermal methods. Increases in the calcination temperature, as well as in the synthesis condition, lead to an increase in the concentration of Ce^{+3} species and therefore an increase in oxygen vacancies.

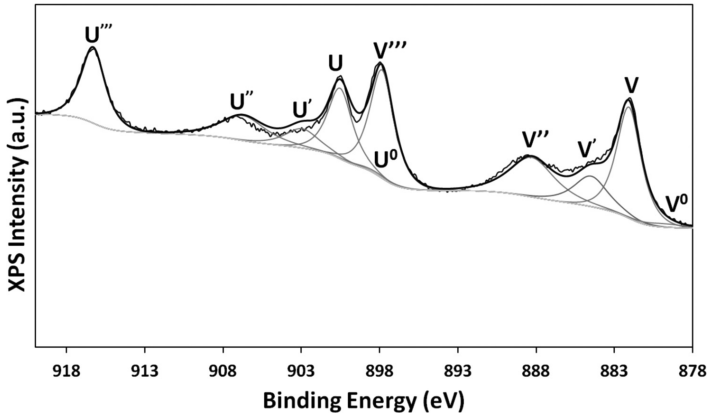

FIG. 9. Deconvoluted XPS spectra of the Ce3d core level.

RIGHTSLINK

TABLE III. Binding energies and integrated peak areas of Ce3d spin–orbit doublets in CeO_2 film deposited on Si.

Peak assignment	Cerium contribution	Peak (eV)	Relative area (%)
Ce $3d_{5/2}$			
U^0	3+	898.45	1.54
U	4+	900.53	12.4
U′	3+	902.95	5.3
U″	4+	906.74	8.13
U‴	4+	916.3	12.74
Ce $3d_{3/2}$			
V^0	3+	880.30	2.37
V	4+	882.18	19.1
V′	3+	884.73	8.16
V″	4+	888.29	12.53
V‴	4+	897.85	17.74

We calculated the O content in the film required to fully oxidize the Ce^{+3} and Ce^{+4} to form Ce_2O_3 and CeO_2, respectively. Taking into account that the stoichiometry O/Ce is equal to 2 for CeO_2 and 1.5 for Ce_2O_3, the ratio of the required oxygen to fully oxidize Ce^{+3} and Ce^{+4} to the sum $[Ce^{+3}] + [Ce^{+4}]$ is determined according to the following equation:

$$\frac{[O]}{[Ce]} = \frac{\frac{3}{2} \times [Ce^{+3}] + 2 \times [Ce^{+4}]}{[Ce^{+3}] + [Ce^{+4}]}. \quad (4)$$

The calculated stoichiometry from Eq. (4) has been compared with the stoichiometry determined directly from the intensities of the O1s and Ce3d XPS peaks. Table II shows the stoichiometry variations of O/Ce determined these two methods. From this calculation, we observed a slight excess of oxygen in the films above that required for CeO_2 and Ce_2O_3 stoichiometry. This excess may be due to some oxygen in residual hydrocarbons in the film. However, the difference is quite small so it has not been considered further here.

Considering the absence of any peak shift in the CeO_2 XRD patterns, formation of an amorphous phase, e.g., at the grain surface and boundaries, is more probable than the formation of a large number of oxygen vacancies which would be likely to cause a significant lattice strain. The formation of amorphous Ce_2O_3 at the grain boundaries was observed previously by Park *et al.*[32] where they deposited CeO_2 films by a pulse dc magnetron sputtering and by Patsalas *et al.*[33] using electron-beam evaporation and ion-beam-assisted deposition techniques for CeO_2 deposition. This increase in amorphous material at the grain boundaries will impede the growth of crystals, which is consistent with smaller grain size and broader XRD peaks for films grown at 300 °C, which have a higher Ce^{3+} content.

C. Catalytic activity of the cerium oxide

This section describes the evaluation of the catalytic activity of CeO_2 thin films deposited at 180, 200, 250, and 300 °C for soot combustion applications. Carbon soot was deposited by burning diesel fuel in the combustion chamber as discussed in Sec. II. Soot was deposited on CeO_2 coated stainless steel foil and also bare stainless steel foil for reference purposes. The annealing test was carried out under ambient air environment inside the oven at the temperature range of 350–490 °C for 4 h.

Figure 10 shows curves of soot conversion versus annealing temperature for catalytic and noncatalytic combustion. The conversion is defined as

$$C(\%) = \frac{M_0 - M}{M_0} \times 100\%, \quad (5)$$

where is M_0 is the initial soot mass, and M is the amount of soot left on the catalyst after burning by heating up to a given T value. Both values were obtained after weighing of samples prior to and after the annealing test.

In Fig. 10, it can be seen that with increase in the annealing temperature all cerium oxide samples started to oxidize soot rather efficiently in contrast to the reference uncoated sample. CeO_2 samples deposited at 180, 200, and 250 °C

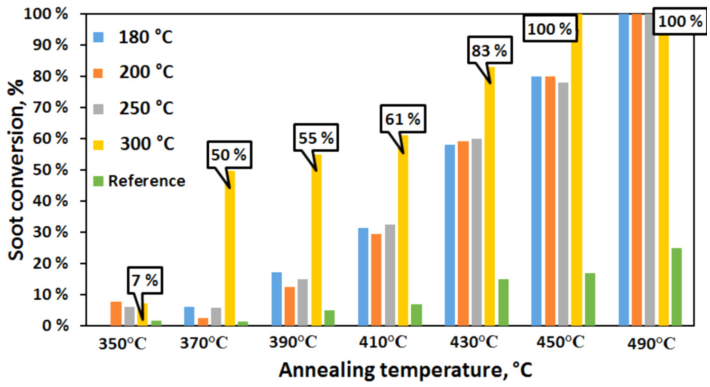

FIG. 10. (Color online) Conversion of oxidized soot on cerium oxide thin films deposited on stainless steel foil at 180, 200, 250, and 300 °C vs annealing temperature during 4 h. The measurement uncertainty is approximately 5%.

RIGHTSLINK

TABLE IV. Catalytic performance for soot oxidation.

Catalyst	T_i (°C)	T_f (°C)
None	410	600
CeO_2 180 °C	350	490
CeO_2 200 °C	350	490
CeO_2 250 °C	350	490
CeO_2 300 °C	350	450

started to oxidize soot at 350–370 °C and had a similar activity during the soot combustion test. The performance of these catalysts increased monotonically with the increase in the annealing temperature. Further increase in the temperature up to 490 °C led to complete soot conversion on all CeO_2 samples. The highest catalytic activity was observed for CeO_2 thin films deposited at 300 °C, which oxidized almost 50% of the soot at 370 °C temperature at a given time, while the rest of the catalysts burnt only 6% of the soot under the same conditions. In addition, CeO_2 deposited at 300 °C decomposed 100% of the soot at the lowest temperature of 450 °C. As expected, complete soot conversion on the uncoated reference sample was only achieved at 600 °C.

The reason for the higher catalytic activity of CeO_2 catalyst deposited at 300 °C may be partly attributed to a higher surface area of the film. Based on XRD and AFM results we can see that CeO_2 catalyst deposited at 300 °C has smaller grain size and larger cluster size compared to CeO_2 thin films deposited at lower temperatures. However, the fact that there is a lower catalyst activation temperature rather than just a difference in magnitude of the catalytic effect shows that this is not the main reason. Another important parameter related to the kinetics of soot oxidation is the oxygen mobility. The oxygen mobility facilitates the mechanism of soot oxidation via formation and regeneration of the Ce^{+4}/Ce^{+3} redox pair. XPS analysis showed that CeO_2 thin film deposited at 300 °C contains higher concentration of Ce^{+3} than other catalysts. Such an effect promotes the increase in active oxygen species and helps to increase the rate of the transfer of oxygen species from the catalyst to the carbon surface.

In Table IV, the characteristic temperatures are listed. T_i is the temperature at which the combustion begins, and T_f is the temperature at which the soot is completely converted. We can propose that the combustion of soot takes place mainly by the oxygen supplied by the cerium oxide but the presence of molecular oxygen in the gaseous phase is necessary to regenerate the catalyst. Mul *et al.*[34] suggested that molecular oxygen is necessary to maintain a chemical potential gradient to "push the chain of surface oxygen atoms."

Photos of soot combustion behavior in ambient air over CeO_2 catalysts deposited at 180, 200, 250, and 300 °C on stainless steel foil are shown in Fig. 11. After the annealing of these soot covered catalysts at 430 °C for 4 h, a carbon black area was completely oxidized by the CeO_2 catalyst deposited at 300 °C. The rest of CeO_2 catalysts showed only partial soot decomposition. These results are consistent with Fig. 10. As mentioned above, soot is oxidized by oxygen species on the CeO_2 catalyst surface and the reduced ceria component subsequently incorporates oxygen from the gas phase.

Finally, reproducibility is one of the parameters for the evaluation of performance, and for these experiments, five CeO_2 catalytic coatings were separately prepared for each deposition temperature, and the observed results have shown the acceptable reproducibility with a relative standard deviation of less than 5%. Figure 12 displays the results of three consecutive combustion cycles for CeO_2 catalyst deposited at 300 °C. After the first annealing test, the CeO_2 catalyst was recovered with soot for the second and third annealing. It can be seen that the catalyst does not lose activity, since the combustion curves obtained in the first, in the second, and in the third tests were very similar. The consistency of the performance in repeated combustion tests also shows that significant restructuring of the film due to annealing at the combustion temperature does not occur.

IV. SUMMARY AND CONCLUSIONS

Cerium oxide thin films were deposited by ALD at a range of substrate temperatures within the ALD growth window with $Ce(thd)_4$ and O_3 as precursors. The growth rates of CeO_2 thin films were 0.3 Å/cycle and 0.37 Å/cycle at 180–250 °C and at 300 °C, respectively. CeO_2 thin films deposited at high temperature (350 °C), which were above the ALD window, contained higher impurity level of carbon due to $Ce(thd)_4$ decomposition and the ALD process could not be fully predicted. An XRD analysis showed that the CeO_2 films were polycrystalline. The structure of the CeO_2

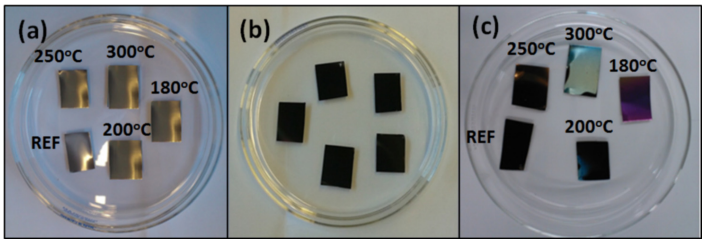

FIG. 11. (Color online) Annealing of soot on CeO_2 catalysts deposited at 180, 200, 150, and 300 °C with 2000 ALD cycles on stainless steel foil: (a) after CeO_2 ALD coating, (b) covered by soot, and (c) after annealing test at 430 °C for 4 h.

RIGHTSLINK

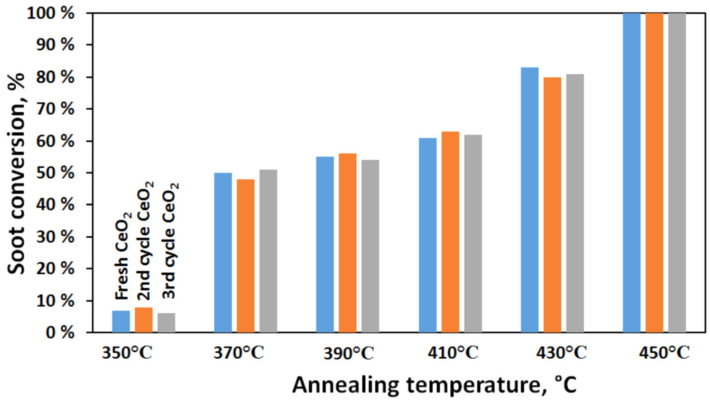

FIG. 12. (Color online) Multiple reuse of CeO_2 catalyst deposited at 300 °C on stainless steel foil vs annealing temperature during 4 h.

deposited at 300 °C differed from the films deposited at lower temperatures. The grain size calculated from x-ray reflections from the (111) and (200) planes were smaller than on the others samples and the cluster size estimated from AFM images were bigger. Small crystallites and large clusters will lead to a large surface area of the film. In addition, an XPS analysis showed multiple Ce oxidation states mostly consist of Ce^{+4} but with a significant amount of Ce^{3+}. Furthermore, the concentration of Ce^{+3} in ceria film deposited at 300 °C was higher than in the others. As no Ce_2O_3 reflection was seen in the XRD pattern, and no peak shifts due to lattice strain were seen in the CeO_2 reflections, we conclude that the Ce_2O_3 exists in an amorphous phase.

The CeO_2 coatings deposited by ALD were investigated as catalysts for soot oxidation. The difference in carbon oxidation behavior in CeO_2 deposited at different temperatures was observed. It was found that the cerium oxide deposited at 300 °C had a better activity than CeO_2 deposited at lower temperatures. CeO_2 deposited at 300 °C decomposed 100% of soot at an annealing temperature of 450 °C while CeO_2 deposited at lower temperatures required 490 °C to oxidize 100% of the soot. The temperature of onset of significant levels of soot combustion was lower for the 300 °C films, showing that this was not merely a surface are effect but due to the higher Ce^{3+} concentration in these films which can form more active oxygen which then reacts with soot to yield carbon dioxide.

ACKNOWLEDGMENTS

Acknowledgment is given to TEKES (Project No. 70006/13), the Finnish Agency for Technology and Innovation, for its financial support for this work; to the European Regional Development Fund (Project No. CZ.1.05/2.1.00/03.0086); and to the Ministry of Education Youth and Sports of Czech Republic [Project No. LO1411 (NPU I)].

[1]A. Trovarelli, C. de Leitenburg, M. Boaro, and G. Dolcetti, Catal. Today **50**, 353 (1999).
[2]E. Aneggi, C. de Leitenburg, and A. Trovarelli, *Catalysis by Ceria and Related Materials*, 2nd ed., edited by A. Trovarelli (ICP, London, 2013), Vol. 12, pp. 565–622.
[3]M. Jeguirim, V. Tschamber, and P. Ehrburger, Appl. Catal. B **76**, 235 (2007).
[4]R. Prasad and V. R. Bella, Bull. Chem. React. Eng. Catal. **5**, 69 (2010).
[5]J. P. A. Neeft, M. Makkee, and J. A. Moulijn, Appl. Catal. B **8**, 57 (1996).
[6]L. F. Nascimento, R. F. Martins, and O. A. Serra, J. Rare Earth **32**, 610 (2014).
[7]A. Bueno-López, Appl. Catal. B **146**, 1 (2014).
[8]S. Sugiyama, Y. Iizuka, E. Nitta, H. Hayashi, and J. B. Moffat, J. Catal. **189**, 233 (2000).
[9]E. Aneggi, C. de Leitenburg, G. Dolcetti, and A. Trovarelli, Catal. Today **136**, 3 (2008).
[10]M. Machida, Y. Murata, K. Kishikawa, D. Zhang, and K. Ikeue, Chem. Mater. **20**, 4489 (2008).
[11]A. Setiabudi, J. Chen, G. Mul, M. Makkee, and J. A. Moulijn, Appl. Catal. B **51**, 9 (2004).
[12]X. Wu, F. Lin, H. Xu, and D. Weng, Appl. Catal. B **96**, 101 (2010).
[13]S. Imamura, A. Doi, and S. Ishida, Ind. Eng. Chem. Prod. Res. Dev. **24**, 75 (1985).
[14]P. Palmisano, N. Russo, P. Fino, D. Fino, and C. Badini, Appl. Catal. B **69**, 85 (2006).
[15]K. Pollard, H. A. Jenkins, and R. J. Puddephatt, Chem. Mater. **12**, 701 (2000).
[16]R. I. Walton, Prog. Cryst. Growth Charact. **57**, 93 (2011).
[17]L. Yang, X. Pang, G. Fox-Rabinovich, S. Veldhuis, and I. Zhitomirsky, Surf. Coat. Technol. **206**, 1 (2011).
[18]A. Turkovic, P. Dubcek, and S. Bernstorff, Mater. Sci. Eng. B **58**, 263 (1999).
[19]J. Päiväsaari, M. Putkonen, and L. Niinistö, J. Mater. Chem. **12**, 1828 (2002).
[20]A. Marizy, P. Roussel, A. Ringuede, and M. Cassir, J. Mater. Chem. A **3**, 10498 (2015).
[21]Z. Fan, J. An, A. Iancu, and F. B. Prinz, J. Power Sources **218**, 187 (2012).
[22]M. Coll, A. Palau, J. C. Gonzalez-Rosillo, J. Gazquez, X. Obradors, and T. Puig, Thin Solid Films **553**, 7 (2014).
[23]B. J. O'Neill *et al.*, ACS Catal. **5**, 1804 (2015).
[24]J. I. Langford and A. J. C. Wilson, J. Appl. Crystallogr. **11**, 102 (1978).
[25]R. Jenkins and R. L. Snyder, *Introduction to X-ray Powder Diffractometry* (Wiley, NJ, 1996).
[26]M. Heikkilä, E. Puukilainen, M. Ritala, and M. Leskelä, J. Photochem. Photobiol. A **204**, 200 (2009).
[27]J. C. Wilson, P. Phys. Soc. **80**, 286 (1962).

RIGHTSLINK

[28]J. P. Holgano, R. Alvarez, and G. Munuera, Appl. Surf. Sci. **161**, 301 (2000).
[29]Y. Zhu, N. Jain, M. K. Hudait, D. Maurya, R. Varghese, and S. Priya, J. Vac. Sci. Technol., B **32**, 011217 (2014).
[30]J. Z. Shyu, K. Otto, and W. L. Watkins, J. Catal. **114**, 23 (1988).
[31]R. C. R. Neto and M. Schmal, Appl. Catal. A **450**, 131 (2013).
[32]I. W. Park, J. Lin, J. J. Moore, M. Khafizov, D. Hurley, M. V. Manuel, and T. Allen, Surf. Coat. Technol. **217**, 34 (2013).
[33]P. Patsalas, S. Logothetidis, L. Sygellou, and S. Kennou, Phys. Rev. B **68**, 035104 (2003).
[34]G. Mul, F. Kapteijn, C. Doornkamp, and J. A. Moulijn, J. Catal. **179**, 258 (1998).

RIGHTSLINK

Publication IV

Ivanova T.V., Homola T., Bryukvin A. and Cameron D.C.

Catalytic Performance of Ag_2O and Ag Doped CeO_2 Prepared by Atomic Layer Deposition for Diesel Soot Oxidation

Reprinted with permission from
Coatings
Vol. 8 (7), p. 237, 2018
© 2018, MDPI

coatings

MDPI

Article

Catalytic Performance of Ag_2O and Ag Doped CeO_2 Prepared by Atomic Layer Deposition for Diesel Soot Oxidation

Tatiana V. Ivanova [1,*], Tomáš Homola [2], Anton Bryukvin [1] and David C. Cameron [2]

[1] ASTRaL Team, Laboratory of Green Chemistry, School of Engineering Science, Lappeenranta University of Technology, Sammonkatu 12, FI-50130 Mikkeli, Finland; brykvin@gmail.com

[2] R & D Centre for Low-Cost Plasma and Nanotechnology Surface Modification, Masaryk University, Kotlářská 267/2, 611 37 Brno, Czech Republic; tomas.homola@mail.muni.cz (T.H.); dccameron@mail.muni.cz (D.C.C.)

* Correspondence: tatiana.ivanova@student.lut.fi; Tel.: +358-401-978-567

Received: 31 May 2018; Accepted: 28 June 2018; Published: 4 July 2018

Abstract: The catalytic behaviour of Ag_2O and Ag doped CeO_2 thin films, deposited by atomic layer deposition (ALD), was investigated for diesel soot oxidation. The silver oxide was deposited from pulses of the organometallic precursor (hfac)Ag(PMe_3) and ozone at 200 °C with growth rate of 0.28 Å/cycle. Thickness, crystallinity, elemental composition, and morphology of the Ag_2O and Ag doped CeO_2 films deposited on Si (100) were characterized by ellipsometry, X-ray diffraction (XRD), X-ray photoelectron spectroscopy (XPS), atomic force microscopy (AFM), and field emission scanning electron microscopy (FESEM), respectively. The catalytic effect on diesel soot combustion of pure Ag_2O, CeO_2, and Ag doped CeO_2 films grown on stainless steel foil supports was measured with oxidation tests. Nominally CeO_2:Ag 10:1 doped CeO_2 films were most effective and oxidized 100% of soot at 390 °C, while the Ag_2O films were 100% effective at 410 °C. The doped films also showed much higher stability; their performance remained stable after five tests with only a 10% initial reduction in efficiency whereas the performance of the Ag_2O films reduced by 50% after the first test. It was concluded that the presence of Ag^+ sites on the catalyst is responsible for the high soot oxidation activity.

Keywords: silver oxide; cerium oxide; oxidation; diesel soot; catalysis; ALD

1. Introduction

The number of diesel-powered vehicles has increased rapidly in recent years due to their reduced fuel consumption and thus lower CO_2 emission compared to petrol engines. However, diesel engines produce a high content of nitrogen oxides (NO_x) and particulate matter (PM) in their exhaust [1]. These emissions have a negative impact on human health causing respiratory, cardiovascular, and lung diseases, as well as on the environment such as disruption of the natural growth of plants and pollution of air, water, and soil [2,3]. Even though it is likely that many diesel engines will be replaced by petrol or electric engines in the future, there will still be a great need for diesel exhaust cleaning for some time to come.

In order to remove soot from the exhaust, diesel particulate filters (DPFs) are widely used [1]. Conventional DPFs require periodic regeneration by increasing the temperature of the exhaust gases to the soot combustion temperature, which is approximately 600 °C [4]. This method results in an increase in fuel consumption and clogging of the DPF by ash resulting in a slow increase of back pressure in the exhaust [1].

The composition of the exhaust mixture also affects the catalytic activity. Oxygen and NO_2 are generally used to oxidize diesel soot. NO contained in the raw exhaust gas is oxidized with excess oxygen into NO_2. Therefore, the development of catalysts, which can produce highly reactive oxygen species from O_2 molecules and NO_2 from NO, is the key issue. The catalyst promotes NO to NO_2 oxidation and NO_2 is then transported via the gas phase over the soot particles, oxidizing carbon while being reduced back to NO [5,6].

The preferred solution for continuous regeneration of the DPF is a catalysed diesel particulate filter (C-DPF) [7]. The main requirements for the catalyst are a reduction in temperature at which soot combustion occurs and long-term thermal and chemical stability.

Ceria-based catalysts have been studied in depth for various environmental applications such as three-way catalysts (TWC) for automotive pollution control, fluid catalytic cracking (FCC), and fuel cells [8,9]. The high potential of ceria as a catalyst is due to its fast and reversible reduction to sub-stoichiometric phases (CeO_2–CeO_{2-x}) as well as the high mobility of oxygen ions in its crystal lattice [10]. However, the use of metal-doped oxide catalysts can improve the performance of the bare oxide due to the increased mobility of oxygen species or the facilitation of the redox mechanisms associated with oxygen release/adsorption [11].

The influence of doping elements on the catalytic properties of ceria has been reported on recently by many researchers. The catalytic activity of ceria can be enhanced by doping with isovalent (Ti^{4+}, Zr^{4+}, Hf^{4+}, Sn^{4+}, etc.) and aliovalent (Zn^{2+}, La^{3+}, Ag^{+}, Eu^{3+}, etc.) cations into the ceria lattice [12–15]. Furthermore, the beneficial influence of Rh, Pd, Cu, Au, and Ag supported CeO_2 catalysts has been reported on elsewhere [16–18]. These reports showed increased electron mobility between the cerium buffer layer and support, favouring the formation of oxygen vacancies in CeO_2. Rangaswamy et al. [19] studied CeO_2–Sm_2O_3 and CeO_2–La_2O_3 catalysts, which could oxidize 50% of diesel soot under loose contact mode at 517 and 579 °C, respectively.

Among the metal additives investigated so far, Ag-based materials are the most promising catalysts for oxidizing diesel soot at low temperatures. Aneggi et al. [20] reported the effect of Ag addition on various metal oxides (CeO_2, ZrO_2, Al_2O_3) during soot oxidation activity. They showed that Ag/CeO_2 and Ag/ZrO_2 catalysts have high soot oxidation activity in the temperature region around 300 °C under tight contact mode. Haneda et al. [21] also performed isotopic transient kinetic analysis on Ag/ZrO_2 catalyst and concluded that the presence of Ag^{+} sites in Ag/ZrO_2 was responsible for the high soot oxidation activity. Ag and Fe doped Mn_2O_3 catalysts were examined by Kuwahara et al. to enhance soot oxidation under tight contact mode and showed the T50 (the temperature for 50% of soot combustion) at 290 °C and at 328 °C, respectively. Based on their measurements, the mechanism of soot oxidation was proposed to be by the activated lattice oxygen species in Ag doped Mn_2O_3 catalyst via the redox of Ag^0/Ag_2O species [22].

Machida et al. [9] investigated silver loading onto CeO_2 and showed the enhancement of catalytic activity for soot oxidation because of the enhanced generation of superoxide. Shimizu et al. [23] showed that the presence of Ag metal nanoparticles on CeO_2 significantly improved the reactivity of CeO_2 lattice oxygen during soot decomposition under oxygen and under inert atmosphere. In addition, a dopant of silver in CeO_2 may increase oxygen mobility due to a weakened Ce–O bond [24].

There are a number of methods of preparation of Ag doped CeO_2 catalysts such as co-precipitation [25], impregnation [19,26], and liquid-phase chemical reduction [20]. We chose to use atomic layer deposition (ALD). The benefits of ALD compared to the other methods are extreme film thickness uniformity, precise thickness control, excellent step coverage, and high reproducibility. The thickness of the films can be easily controlled by controlling the number of deposition cycles. Furthermore, the fact that ALD operates via self-limiting surface reactions in consecutive cycles means that doping materials can be introduced with greater control and tuning than other deposition methods. ALD can be used to deposit catalytic coatings on high surface area porous powder supports or on geometrically complex structures [27] such as particulate filters in diesel engine exhaust systems.

In this study, we investigated the ALD of Ag_2O and Ag doped CeO_2 for catalytic applications in soot combustion under loose contact mode. The crystal structure, morphology, and composition properties of the deposited films were analysed. The effect of doping on the efficacy of soot combustion in annealing tests was also studied, paying particular attention to the doping concentration and oxidation state of silver in the CeO_2 thin films.

2. Materials and Methods

2.1. Catalyst Preparation

The deposition of Ag doped cerium oxide was carried out using an F-120 ALD reactor (ASM Microchemistry Ltd., Espoo, Finland). Thin films were deposited with different doping concentrations at a reaction temperature of 200 °C. The cyclic nature of ALD means that pulses of dopant can easily be incorporated into the main process. The desired composition of catalytic thin film can be achieved by depositing n cycles of the base CeO_2 material (where n can be varied to suit the required doping level) with one cycle of the doping material inserted (Figure 1). The supercycle (n + 1), which consists of two individual ALD processes, was repeated x times until the required film thickness was achieved. The process for CeO-based material contains two half-cycles using 2,2,6,6-tetramethyl-3,5-heptadionatecerium $Ce(C_{11}H_{19}O_2)_4$ ($Ce(thd)_4$ for brevity) and O_3 as precursors. The Ag doping material also comprises two half-cycles of Ag precursor (see below) and O_3.

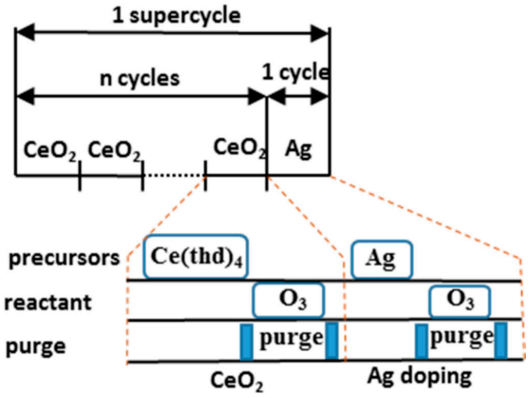

Figure 1. A schematic representation of the atomic layer deposition (ALD) supercycle used to deposit Ag doped CeO_2 catalytic thin films.

$Ce(thd)_4$ (Volatec, Porvoo, Finland) and trimethylphosphine (hexafluoroacetylacetonalo)-silver $Ag(CF_3COCHCOCF_3)P(CH_3)_3$ ((hfac)Ag(PMe_3), 99%; Strem Chemicals, Newburyport, MA, USA) were used as Ce and Ag precursors respectively. Ozone O_3 was used as the co-reactant in both cases and was generated by an ozone generator (Wedeco Modular 4HC Lab, Herford, Germany) from a pure oxygen (>99.999%) source. Ozone concentration was 120 g/m^3. Nitrogen (>99.999%) was used as a carrier and purge gas between precursor pulses. The pressure in the reactor was approximately 1 mbar. $Ce(thd)_4$ and (hfac)Ag(PMe_3) were evaporated at 160 and 80 °C, respectively to achieve sufficient vapour pressure. The saturated deposition rate in the ALD supercycle should be obtained when the two individual ALD processes are in saturation. We used the previously optimized CeO_2 ALD process parameters: 1.5 s $Ce(thd)_4$ dose, 2.5 s purge, 2.5 s O_3 dose, 2.5 s purge [28]. The pulse time for (hfac)Ag(PMe_3) was varied from 0.5 to 4 s in 0.5 s steps while keeping the O_3 pulse time constant at 2.5 s. After finding the optimal pulse time for (hfac)Ag(PMe_3) the pulse time for O_3 was determined with the same method with 2.5 s of the purge time.

In order to achieve doping of CeO_2 with Ag, one supercycle consisted of n CeO_2 cycles, with n equal to 10, 20, and 30, and 1 cycle of Ag. The supercycle was repeated 150, 75, and 50 times for CeO_2:Ag ratios 10:1, 20:1, and 30:1 respectively in order to achieve comparable film thicknesses.

Silicon substrates <100> (Si-Mat, Kaufering, Germany) were used for process development while stainless steel foil AISI 316 with a thickness of 0.025 mm (Goodfellow Cambridge Ltd., London, UK) was used as a substrate for soot burning tests. Stainless steel foil was chosen because of its relatively low weight, which reduced the error during weighing of samples to determine the amount of soot oxidation. The substrates were cut in pieces of 20 mm × 10 mm and cleaned using an ultrasonic bath with acetone, isopropanol, and deionized water consecutively, each with a time of 5 min and thereafter dried using compressed air.

2.2. Soot Deposition System

The soot deposition system was described in detail in the previous report [28]. Briefly, the diesel soot was generated with a Webasto diesel engine preheater (Webasto group, Stockdorf, Germany) from diesel fuel and air. The samples were placed on the heating plate and exposed to exhaust gases for 1.5 min. The amount of deposited soot was measured by weighing the samples.

2.3. Catalyst Characterization

A spectroscopic ellipsometer J.A. Woollam M-2000UI (J.A. Woollam Co., Lincoln, NE, USA) was used to determine the catalytic film thickness. This was obtained by using a Cauchy model for fitting.

The surface topography of the catalytic thin films was evaluated with field emission scanning electron microscopy (FESEM) Hitachi S-4800 (Hitachi, Tokyo, Japan). An atomic force microscopy (AFM) (Park NX10, Park Systems, Suwon, Korea) was utilized for analysing the film morphological properties such as roughness and cluster size. All measurements were done in non-contact mode with a cantilever force constant of 42 N/m.

The crystal structure of the catalytic materials was studied by a Rigaku SmartLab® Type F XRD (Rigaku, Tokyo, Japan; Cu-Kα radiation, λ = 1.5418 Å). The grazing incidence X-ray diffraction (GIXRD) scan was collected with a grazing incidence angle of 0.5°. Scan speed of 0.9°/min and 2θ values from 20° to 90° were used. The high resolution scan was taken with speed 0.045°/min.

The surface chemical composition, bonding properties and analysis of impurities in the deposited films were investigated by X-ray photoelectron spectroscopy (XPS) using an ESCALAB 250Xi (Thermo Scientific, Loughborough, UK) with a monochromated Al-Kα (energy of 1486.7 eV) X-ray source in the constant pass energy mode with a value of 50 eV. For high resolution spectra of Ag 3*d* a pass energy of 20 eV with resolution 0.1 eV was used. Charging compensation by an electron flood source was used in all measurements to minimize binding energy shifts. The binding energy of C 1*s* was set to be 284.5 eV as an internal standard for calibration. Sputtering by Ar^+ ions at 2 kV for 20 s was applied to remove surface contaminations and obtain actual carbon levels in the films. Deconvolution and fitting of the obtained peaks were made with Avantage software (Version 5.938) using Smart type background and applying 90:10 Gaussian-Lorentzian peaks.

2.4. Catalytic Activity

Five samples of Ag doped CeO_2, pure CeO_2 and pure Ag_2O catalytic coatings were separately deposited on stainless steel foils for evaluation of catalytic activity. For measurement of the amount of combusted soot, annealing tests were performed by placing the catalytic samples covered with soot into an oven and measuring the weight loss of the samples over 2 h in the temperature range of 300–490 °C in ambient atmosphere. The molar ratio of catalysts to carbon was approximately 1:80 with average soot mass of 0.7 g. The annealing measurements were repeated 5 times to evaluate reproducibility of the prepared catalysts.

3. Results and Discussion

3.1. Ag_2O and Ag-Doped CeO_2 ALD Film Deposition

3.1.1. Ag_2O

The concept of the supercycle can be effective when two individual processes are compatible with each other and each is in saturation. Therefore, before the introduction of Ag as a dopant into the CeO_2 structure, silver oxide thin films were deposited first on silicon substrates to find the self-limiting growth regime of the ALD process. This could be assessed by measuring the growth rate as a function of the amount of precursor delivered into the reactor. The ALD saturation growth study was carried out at deposition temperature of 200 °C. This temperature was chosen to match the reaction temperature of CeO_2 and it has been shown that the nucleation period of Ag is significantly shortened at this temperature [29]. Figure 2 shows the saturation curves for (hfac)Ag(PMe_3) and O_3. The pulsing time of (hfac)Ag(PMe_3) or O_3 was adjusted within the range of 0.5–4 s while the other precursor pulse was fixed at 2.5 s. The saturation of (hfac)Ag(PMe_3) and O_3 precursors can be seen at 2.5 s with constant Ag_2O growth rate of 0.28 Å/cycle. No further increase of the growth rate was noticed after increasing the precursor pulse time up to 4 s.

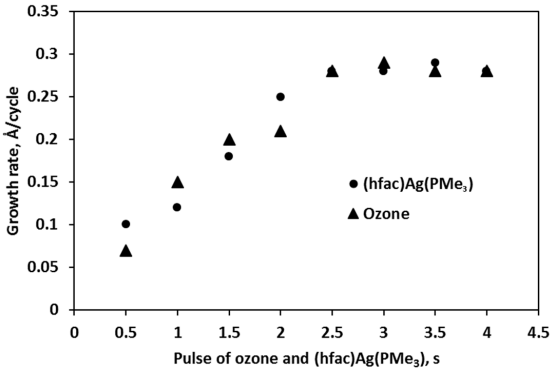

Figure 2. The effect of ozone and (hfac)Ag(PMe_3) pulse time on the growth rate of silver oxide at 200 °C reactor temperature.

Figure 3 shows the Ag_2O film thickness versus the number of ALD cycles from 10 to 750 deposited at 200 °C. From Figure 3 it can be seen that the thickness increases linearly after 100 ALD cycles. The incorporation of silver atoms is directly related to the density of hydroxyl groups on the substrate surface that act as adsorption sites for (hfac)Ag(PMe_3) molecules. As illustrated in Figure 3, the initial growth rate of the films per cycle (GPC) is substrate dependent at the start of the ALD process and it takes about 100 cycles to obtain a stable GPC of 0.28 Å/cycle. The film growth can be separated into two regimes: an island-like growth for the first 100 cycles and layer-by-layer growth as is expected from the proceeding atomic layer deposition. If the bare Si has a higher density of reactive sites compared to the deposited Ag_2O or these sites have a higher reactivity than the reactive sites on Ag_2O, then the growth rate will initially be higher until a complete film is formed. Alternatively, some hfac ligands may not be completely removed by ozone and may remain bound to the surface. These comments are expanded on in Section 3.1.2.

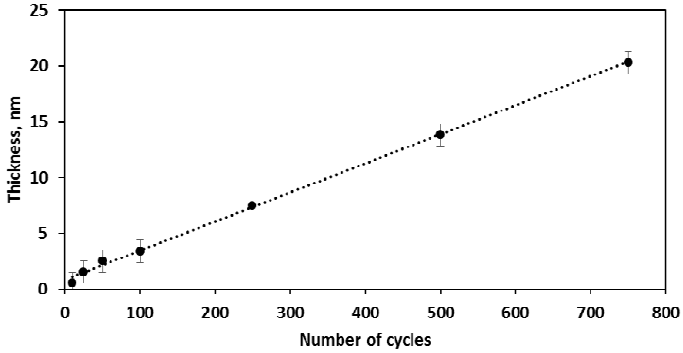

Figure 3. Thickness of the silver oxide film as a function of the number of deposition cycles at the deposition temperature of 200 °C.

3.1.2. Ag Doped CeO_2

The film thickness after deposition with different CeO_2:Ag ratios was measured by spectroscopic ellipsometry. The total number of CeO_2 cycles was chosen to be 1500 while the number of Ag cycles was varied from 50 up to 150 according to the supercycle configuration. Growth rate of the films per cycle (GPC) over the total number of ALD cycles is shown in Figure 4 as a function of Ag dopant fraction in CeO_2 film. The reduction of GPC with increasing Ag dose observed in Figure 4 could be the result of a slight etching of CeO_2 by (hfac)Ag(PMe_3), but it could also be due to nucleation delay and the inhibition of CeO_2 growth after (hfac)Ag(PMe_3) pulsing.

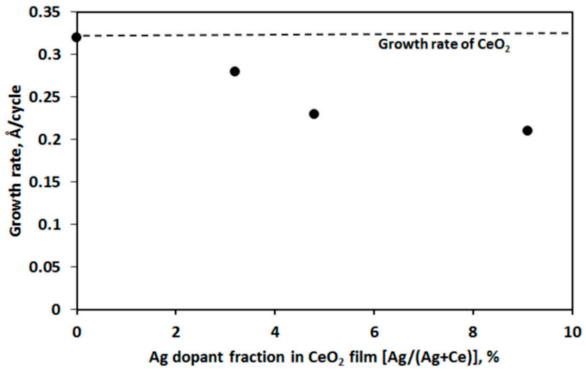

Figure 4. The effect of Ag concentration on the growth rate of Ag doped CeO_2 thin films at 200 °C reactor temperature.

The comparison of the two calculated and experimental silver doping concentrations inside the Ag doped CeO_2 films is shown in Figure 5. The calculated value is determined by the ratio of the number of doping ALD cycles divided by the total number of ALD cycles in one supercycle ($1/(n+1)$). The experimental value is obtained from XPS measurements. It is worth emphasizing that the concentrations of dopant do not relate directly to the doping efficiency. Some of the dopant silver atoms might have formed silver oxide or alloy clusters rather than only doping the film, as will be discussed in Section 3.2.

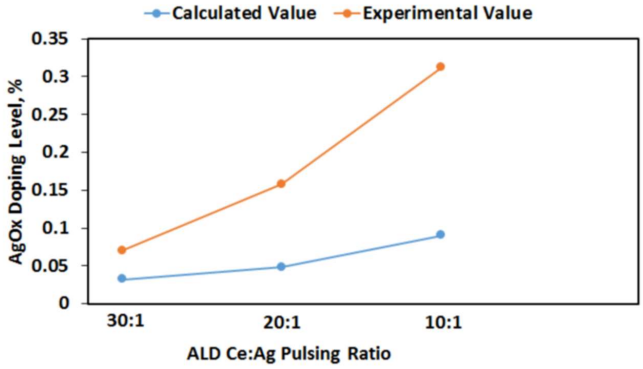

Figure 5. Relationship between CeO_2:Ag pulsing ratio vs. silver molar percent in the corresponding Ag doped CeO_2 thin films.

The hypothetical deposition of Ag doped CeO_2 by ALD can be explained as follows: (a) $Ce(thd)_4$ adsorbs on nucleation sites (–OH) and dissociates into the attached fraction $Ce(thd)_x$*, where * designates surface species, with x varying from 1 to 3 depending on the number of OH sites it bonds to. Most probably, some –OH groups remain unreacted, due to steric hindrance; (b) Ozone regenerates O* groups which can act as nucleation sites during subsequent (hfac)Ag(PMe_3) exposures. The O_3 half-cycle also probably results in the formation of OH groups because of decomposition of the precursor ligand; (c) (hfac)Ag(PMe_3) may adsorb on Ce–O* or Ce–OH nucleation sites and on unreacted –OH groups, and dissociates into Ce(hfac)* and Ag(hfac)* species; (d) ozone may react with Ce(hfac)* and Ag(hfac)* species regenerating O* groups for further $Ce(thd)_4$ exposures. We propose that during $Ce(thd)_4$ treatments, not all –OH or regenerated O* groups can react with the precursor or, as mentioned above, hfac ligands remain bound to the surface and cannot be completely removed by ozone. This statement is supported by XPS measurements, where a high level of impurities was noticed, and is discussed in detail in Section 3.2. It could be the reason for formation of Ag_2O clusters in the films with higher concentration of Ag doping, as will be considered during AFM and SEM analysis. With more CeO_2 ALD cycles, more nucleation sites are generated and this facilitates the growth of CeO_2 thin film with Ag as a dopant.

3.2. Catalyst Characterization

Ag_2O and Ag-Doped CeO_2

In examining the nucleation effect and morphology of the resulting ALD of Ag_2O, several AFM images were taken with variable ALD cycles (Figure 6). The average size of Ag_2O nanoparticles after 25 ALD cycles was around 22 nm with film roughness of 1.5 nm. After 100 ALD cycles, large nanoparticles with size of around 40 nm were present with a high nanoparticle density (Figure 6a) and overall surface coverage. The AFM image of 500 cycles of Ag_2O film is shown in Figure 6b, which demonstrates that the surface is now fully covered with silver, having grain sizes between 40 and 46 nm. As was shown in Figure 3, the nucleation region for Ag_2O ALD occurs over 100 cycles; Ag_2O films can nucleate and grow by the Volmer–Weber (VW) growth mechanism, where the deposited atoms form islands or clusters and three dimensional aggregates on the substrate. Growth of these clusters, along with coarsening, can be a cause of rough thin films on the substrate surface [30].

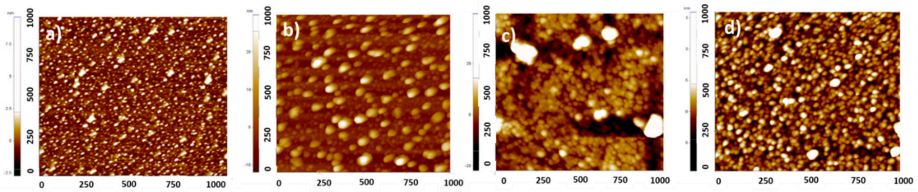

Figure 6. The atomic force microscopy (AFM) non-contact mode images of Ag_2O deposited with: (**a**) 25 cycles (R_a 0.7 nm); (**b**) 100 cycles (R_a 1.5 nm); (**c**) 250 cycles (R_a 1.6 nm); and (**d**) 500 cycles (R_a 1.7 nm). Axis scales are in nm.

All the Ag_2O thin films deposited on Si had a visual matt finish, which is a sign of rough microstructure. SEM studies supported the AFM results (Figure 7). The 250 and 500 ALD cycles films were confirmed to consist of particles with widely different sizes as a result of coalescence and secondary nucleation on existing particles.

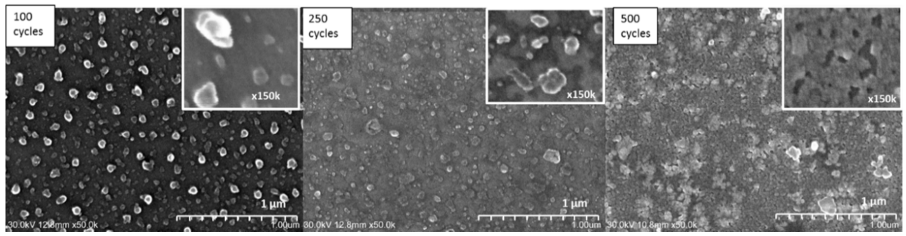

Figure 7. Scanning electron microscope (SEM) images of Ag_2O thin films deposited with different number of cycles at 200 °C resulting in different thicknesses (5.8, 8.8, and 13.8 nm).

The AFM and SEM analyses on Figures 8 and 9 show that the surface morphology of Ag doped CeO_2 films changes in accordance with silver concentration in the film. It can be seen that the reduction of Ag concentration dramatically decreases crystal and cluster sizes in doped films. Figures 8a and 9a suggest that higher concentration of Ag (CeO_2:Ag 10:1) inhibits CeO_2 growth so that the Ag nuclei are not covered with CeO_2 and so the next Ag cycle nucleates more easily on top of the Ag and can therefore form bigger crystals of about 50 nm in size. Such large nanoparticles were noticed on pure Ag_2O and described above. With lower doping concentration of Ag in CeO_2 thin films, no crystals larger than 25 nm were noticed.

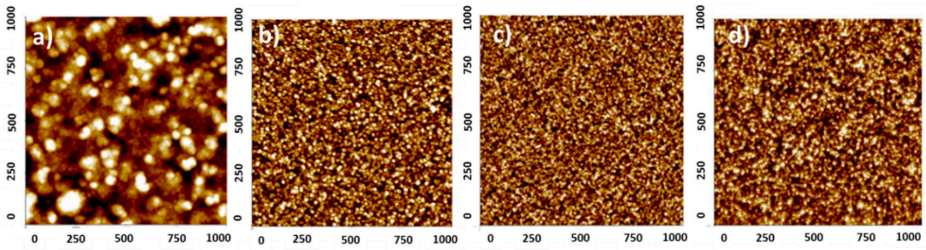

Figure 8. The AFM non-contact mode images of Ag doped CeO_2 in different CeO_2:Ag ratios deposited at 200 °C: (**a**) 10:1; (**b**) 20:1; (**c**) 30:1; and (**d**) CeO_2. The scales are in nm.

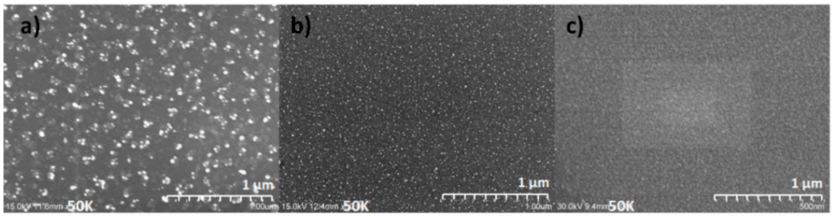

Figure 9. SEM of Ag doped CeO_2 in different CeO_2:Ag ratios (**a**) 10:1, (**b**) 20:1, and (**c**) 30:1 deposited at 200 °C.

Figure 10a shows XRD spectra of Ag_2O, CeO_2, and Ce:Ag 10:1, 20:1, and 30:1 Ag doped CeO_2 films in the 2θ range of 20°–90°. The Ag_2O films showed strong X-ray diffraction peaks at 2θ = 32.7° and 38.3° related to the (111) and to (200) cubic planes of Ag_2O, respectively (ICCD Card No: 00-41-1104). They revealed that the films deposited at 200 °C contained only Ag_2O crystallites. The diffraction peaks at 2θ angles of 28.6°, 33.6°, 47.6°, and 56.3° can be identified for all the other samples and attributed to (111), (200), (220), and (311) planes of cubic cerium oxide, respectively (COD database, card No 9009008). The XRD patterns of CeO_2, Ag_2O, and Ag doped CeO_2 in the 2θ range 24–40° were expanded (Figure 10b) to analyse the position of CeO_2 and Ag_2O reflections in the X-ray spectra in more detail. Figure 10b shows that the cerium oxide peak intensity and the shape of (200) plane reflection in the Ag doped CeO_2 samples decreased and broadened, respectively, with increasing Ag doping, compared to the pure CeO_2 catalyst.

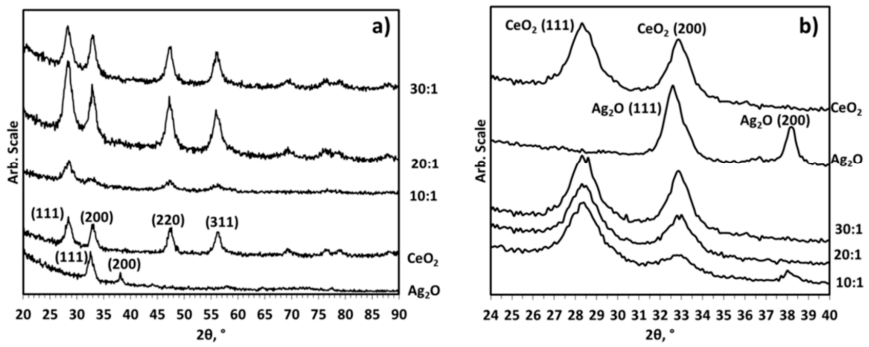

Figure 10. (**a**) X-ray diffraction (XRD) patterns of Ag_2O, CeO_2 and Ag doped CeO_2 with different Ce:Ag ratios 10:1, 20:1, and 30:1 deposited at 200 °C. (**b**) XRD patterns of slow scans of CeO_2, Ag_2O and Ag doped CeO_2 with different Ce:Ag ratios 10:1, 20:1, 30:1 in the 2θ range of 24–40°.

The mean grain size, assuming spherical grains, of CeO_2 can be determined from the full width at half maximum (FWHM) of the (111) XRD peak, through Scherrer's equation. The grain sizes calculated from the (111) plane reflection of CeO_2 are indicated in Table 1. XRD analyses confirm the decrease of the CeO_2 crystallite size of (111) plane as the Ag amount increases. This behaviour is related to the occurrence of lattice defects due to the presence of the dopant, which leads to deformations in the crystalline structure and smaller crystallites. The XRD data do not show any peaks related to Ag species for CeO_2:Ag 20:1 and 30:1 catalysts, which is, most probably, demonstrative of a high distribution of the dopants in the CeO_2 samples. The CeO_2 (200) and Ag_2O (111) appear at very similar positions. However, for higher amount of Ag doping Ce:Ag 10:1, a small peak from the Ag_2O (200) plane reflection can be observed (Figure 10b). In the CeO_2 lattice, the radius of Ce^{4+} ion is 0.97 Å. However, the ionic radius of Ag^+ ions is 1.28 Å [31]. As such, substitution or replacement of Ag^+ ions

for Ce^{4+} ions in the CeO_2 lattice requires high energy [32] and from the XRD there is no evidence of significant substitutional doping during ALD of Ag doped CeO_2 thin films from a shift in the position of the CeO_2 peaks to smaller angles. Ag_2O forms as metal oxide or alloy clusters in CeO_2:Ag 10:1 catalyst and inhibits CeO_2 crystal formation.

Table 1. Grain size of CeO_2 (111) plane reflection based on Scherrer's equation.

Catalyst	Grain Size of CeO_2 (111) (nm)
CeO_2	10.2
Ce:Ag 30:1	8.7
Ce:Ag 20:1	7.1
Ce:Ag 10:1	6.2

XPS was employed to analyse the chemical state of the as-deposited Ag_2O thin films and the Ag doping in CeO_2 films, which were controlled by varying the Ce:Ag supercycle binary process pulse ratio. The information on silver and cerium oxidation states was obtained from the high resolution Ag 3*d* and Ce 3*d* spectra after Ar^+ bombardment to exclude surface contaminations.

Using the values of surface atomic composition from Table 2, an estimation of the O/Ce and O/Ag atomic ratio can be obtained. The ratio O/Ce for the cerium oxide deposited at 200 °C is around two, which indicates that the pure CeO_2 is stoichiometric. The carbon impurity level is around 21 at.%, which arise from the $Ce(thd)_4$. The Ag to O ratio in the Ag_2O films was estimated to be close to 2:1, which indicates that the film primarily consists of Ag_2O with 14.2% of carbon, 0.5% of F, and 3% of N as the main impurities in that film. With regard to the Ag/Ce surface atomic ratio, an important enhancement with Ag loading is observed, indicative of an increase in the number of Ag surface atoms. We found from survey spectra that by changing the Ce:Ag ratio from 30:1 to 10:1 the amount of Ag increases from ~2 at.% to ~9.7 at.%., as measured by XPS (Table 2).

Table 2. Surface elemental composition of Ag doped CeO_2, Ag_2O, and CeO_2 thin films.

Catalyst	Surface Composition (at.%)						Ag/Ce (from Survey)
	Ce 3*d*	Ag 3*d*	O 1*s*	C 1*s*	F 1*s*	N 1*s*	
Ce:Ag 10:1	21.4	9.7	46.1	13.9	8.1	6	0.453
Ce:Ag 20:1	23.9	4.5	43.8	15.7	7.1	5	0.188
Ce:Ag 30:1	26.6	2.0	39.9	17.4	5.7	3.6	0.075
Ag_2O	–	56	27.3	14.2	0.5	3	–
CeO_2	25.9	–	52.9	21.5	–	–	–

High resolution spectra of the Ag 3*d* peaks of Ag_2O and Ag doped CeO_2 thin films with the nominal ratio Ce:Ag from 30:1 to 10:1 give us indications of the chemical state of Ag atoms (Figure 11). The pure Ag_2O films showed only one peak at 368.2 eV. The binding energy which has been observed for pure Ag_2O thin film is 367.2 eV, which consists of the dominant oxidation state Ag^+ [33]. The spectrum here shows a shift of ~1 eV in the peak position compared to the previously found results which may be due to sample charging. The spectrum showed core level binding energies at about 368.2 ± 0.1 eV and 374.2 ± 0.1 eV related to the Ag $3d_{5/2}$ and Ag $3d_{3/2}$ respectively with spin orbit separation of 6 eV [34]. Each Ag 3*d* level in Ag doped CeO_2 films can be deconvoluted into three peaks, with corresponding binding energies 368.2, 369.2, and 367.2 eV, which are consistent with those of Ag^+, Ag^0, and Ag^{2+} (Table 3), allowing for the shift due to sample charging [35–37]. The estimated percentages of the three peaks, shown in Table 3, indicates that with increasing Ag doping concentration in CeO_2 films from 30:1 to 10:1, the Ag^+ oxidation state also grows from 38.4% to 85%, respectively. At the same time the Ag^0 oxidation state decreases from 59% to 9.7% for CeO_2 doped Ag films deposited with the ratio Ce:Ag from 30:1 to 10:1, respectively.

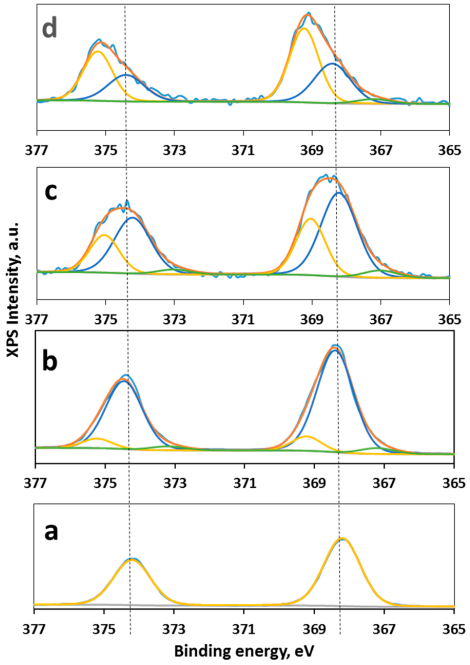

Figure 11. High resolution Ag 3*d* X-ray photoelectron spectroscopy (XPS) spectra of (**a**) pure Ag_2O and Ag doped CeO_2 in different CeO_2:Ag ratio (**b**) 10:1, (**c**) 20:1, and (**d**) 30:1.

Table 3. Binding energies and integrated peak areas of Ag 3*d* spin-orbit doublets in Ag_2O, Ag doped CeO_2 and CeO_2 thin films.

Catalyst	Compound (BE, eV)			Concentration of Ce^{4+} (at.%) (Excluding C)	Concentration of Ce^{3+} (at.%) (Excluding C)	Ce^{3+}/Ce^{4+} (%)
	Ag^+ (368.2 ± 0.1)	Ag^0 (369.2 ± 0.1)	Ag^{2+} (367.2)			
Ag_2O	100	–	–	–	–	–
Ce:Ag 10:1	85	9.7	4.5	77	23	29.8
Ce:Ag 20:1	59	35	6	80	20	25.0
Ce:Ag 30:1	38.4	59	2.6	82	18	21.9
CeO_2	–	–	–	83	17	20.4

Figure 11 and Table 3 show that at low doping concentration, Ag species mainly exist as Ag^0, while as doping concentration increases, Ag^+ species increase remarkably. It is likely that at low concentrations of Ag_2O doping, some of the silver oxide is reduced by the CeO_2; a similar effect has been reported on Ag_2O-doped TiO_2 [38]. For higher Ag dopant concentration, most of the silver present in the catalysts remains as cations and probably interacts with CeO_2 through the Ag–O bonds. Based on previous studies involving silver oxides [39–42], it can be concluded that some electrons may transfer from CeO_2 to the Ag dopant and there is strong interaction between the Ag species and the CeO_2 catalyst.

It is interesting to note that the concentration of Ce^{4+} decreased from 82% to 77% and the concentration of Ce^{3+} increased from 18% to 23% with increasing Ce:Ag doping from 30:1 to 10:1, respectively, further suggesting the existence of the interaction between Ag and CeO_2. This is probably because the Ag^+ ions in Ag doped CeO_2 can partially substitute Ce^{4+} in the CeO_2 matrix in the form of $Ce_{1-x}Ag_xO_{2-\delta}$. As was shown earlier from the XRD spectra, there is no evidence of substitutional doping. However, the increasing Ag content also produced smaller crystallites so it may be that the

increasing Ce^{3+} arises as a consequence of interaction between the CeO_2 and the Ag in the disordered regions at the grain boundaries. In summary, Ag atoms deposited on a stoichiometric CeO_2 surface tend to result in reduction of the Ce ions, which leads to the stabilization of the Ag in the +1 oxidation state. These results are in good agreement with the literature reports [43–45].

3.3. Catalytic Activity of Ag_2O, CeO_2, and Ag-doped CeO_2 catalysts

The evaluation of the catalytic activity of Ag_2O, CeO_2, and Ag doped CeO_2 thin films deposited at 200 °C on stainless steel foil was carried out to show the effectiveness of the catalysts for soot combustion applications. The annealing tests of carbon soot, which was generated from diesel fuel, was carried out under ambient air environment inside an oven in the temperature range 300–490 °C for 2 h.

Figure 12 shows histograms of soot conversion vs. annealing temperature for catalytic and non-catalytic combustion. The conversion is defined as:

$$C(\%) = \frac{M_0 - M}{M_0} \times 100\% \quad (1)$$

where is M_0 is the initial soot mass, and M is the amount of soot left on the catalyst after burning by heating up to a given T value. Weight loss values were obtained by weighing the samples before and after the annealing test which continued for 2 h.

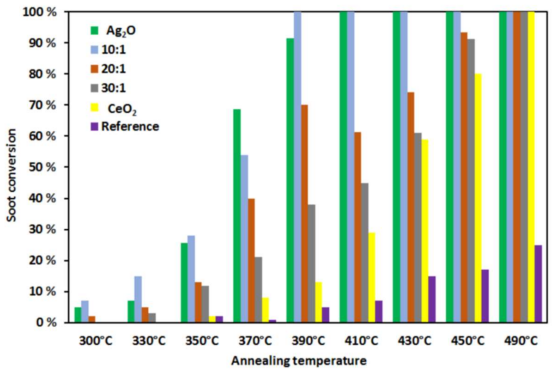

Figure 12. Conversion of oxidized soot on silver oxide, cerium oxide, and silver doped cerium oxide in ratio CeO_2:Ag 10:1, 20:1, 30:1 thin films deposited on stainless steel foil at 200 °C vs. annealing temperature over 2 h. The measurement uncertainty is approximately 5%.

The conversion of oxidized soot was demonstrated on non-catalysed reference steel foil, and on cerium oxide, silver oxide, and Ag doped CeO_2 thin films deposited on stainless steel foil at 200 °C in loose contact mode (Figure 12). As expected, complete soot conversion on the uncoated reference sample was only achieved at 600 °C. All the catalysts were effective in promoting combustion at temperatures below 490 °C. Although the soot was well oxidized on pure CeO_2 and Ag_2O thin films themselves, Ag loading into CeO_2 thin films caused a significant enhancement of soot oxidation rate, in accordance with previous reports [28]. It is noteworthy that the soot oxidation activity of Ag doped CeO_2 was different depending on the dopant concentration. The sample having the maximum silver loading CeO_2:Ag 10:1 and pure Ag_2O showed the lowest oxidation temperature of 300 °C and complete combustion of the soot was achieved below 390 and 410 °C under real-world loose contact conditions, respectively. Table 4 lists the characteristic temperatures, where the ignition temperature (T_i) is the temperature at which the combustion began, and the final temperature (T_f) is the temperature at which the soot was completely oxidized.

Table 4. Catalytic performance for soot oxidation.

Catalyst	T_i (°C)	T_f (°C)
None	410	600
CeO_2	350	490
CeO_2:Ag 10:1	300	390
CeO_2:Ag 20:1	300	490
CeO_2:Ag 30:1	330	490
Ag_2O	300	410

The catalysts with silver doping concentration of Ce_2O:Ag 20:1 and 30:1 showed lower performance for 100% soot oxidation at T_f = 490 °C. This indicates that the highest concentration of Ag^+ ions, which is contained mostly in CeO_2:Ag 10:1 catalyst, can effectively promote 100% soot oxidation at T_f = 390 °C due to the oxygen species formed on Ag^+ sites. Zou et al. [46] proposed that during silver oxide decomposition, its released oxygen migrates to soot surfaces to form carbon–oxygen intermediates, which are subsequently oxidized further. Finally, the adsorbed oxygen on the silver promotes the regeneration process. The redox reaction of Ag^+ and the active oxygen species prevail in the reaction at low combustion temperatures. In addition, the silver oxide contributes to the adsorption of reactants to form complex π bonds that are significant for the formation of peroxide and superoxide species [47]. It is worth mentioning that higher concentration of Ce^{3+} contained in CeO_2:Ag 10:1 catalyst can also form more active oxygen vacancies, which promote the activation of adsorbed oxygen to form superoxides in the lattice. These types of oxygen react with soot efficiently [48].

Because the melting point of Ag_2O oxides is relatively low, compared with CeO_2 (2400 °C), the stability of Ag/CeO_2 catalysts during the soot oxidation is an important factor from the practical point of view. In order to gain information on the stability of Ag/CeO_2, repetitive activity tests were carried out in loose contact mode at annealing temperature 430 °C. Figure 13 shows the conversion of oxidized soot after five replicate trials, and the observed results showed acceptable reproducibility with relative standard deviation of less than 5%. The pure Ag_2O catalyst lost its catalytic activity immediately after the first trial from 100% to 50% of oxidized soot. Further use of Ag_2O catalyst (in the third, fourth, and fifth trials) led to significant restructuring of the film and total loss of catalytic properties. For this reason, bulk Ag_2O cannot be used in catalytic systems operating at higher temperature (above 300 °C).

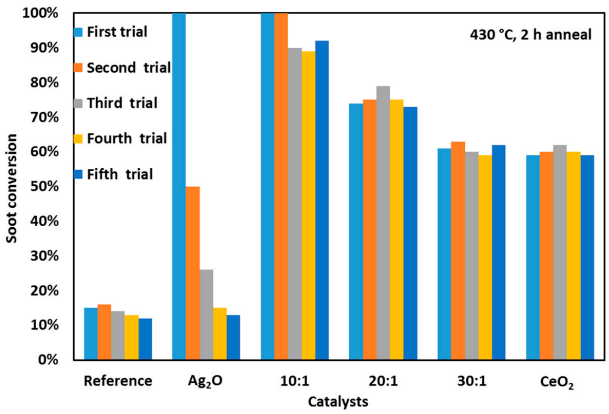

Figure 13. Repetitive soot oxidation in the presence of silver oxide, cerium oxide, and silver doped cerium oxide in ratio CeO_2:Ag 10:1, 20:1, and 30:1 thin films deposited on stainless steel foil at 200 °C vs. annealing temperature over 2 h at 430 °C.

It appears that CeO_2/Ag 10:1 lost 10% of its activity in the third combustion test, indicating the deactivation of Ag/CeO_2. However, during further trials this catalyst showed stable results of 90% oxidized soot. We can assume that Ag ions have a strong interaction with the CeO_2 catalyst and remain stable after durability tests. Other catalysts such as CeO_2:Ag 20:1, 30:1 and pure CeO_2 do not lose activity, since the combustion curves obtained from the first to the fifth tests were very similar.

4. Conclusions

We have demonstrated that ALD can be used to deposit Ag_2O and Ag doped CeO_2 catalysts at 200 °C with (hfac)Ag(PMe_3), Ce(thd)$_4$, and O_3 as precursors. The growth rate stabilized to a steady-state Ag_2O GPC of 0.28 Å/cycle after 100 ALD cycles. The silver doping concentration was finely tuned by setting the CeO_2:Ag cycle ratio to 10:1, 20:1, and 30:1. With increasing Ag concentration in the CeO_2 thin films, the overall GPC decreased from 0.32 down to 0.21 Å/cycles. AFM and SEM analyses showed that higher concentration of Ag (CeO_2:Ag 10:1) inhibited CeO_2 growth so that the Ag nuclei were not covered with CeO_2 and so the next Ag cycle nucleated more easily on top of the Ag and could therefore form bigger crystals. XRD and XPS analyses showed that the Ag^+ oxidation state dominated for CeO_2:Ag 10:1 catalysts and stoichiometric CeO_2 tended to be reduced from Ce^{4+} to Ce^{3+} ions.

The performance of soot combustion with Ag_2O and Ag doped CeO_2 with different silver concentrations was compared at operating temperatures 300–500 °C. The annealing test showed that higher concentration of Ag^+ in CeO_2:Ag 10:1 catalytic films was as effective as Ag_2O films; effectively promoting 100% soot oxidation at T_f = 390 °C due to the oxygen species formed on Ag^+ sites. It is worth mentioning that the higher concentrations of Ce^{3+} in the CeO_2:Ag 10:1 catalyst films can also form more active oxygen, which then reacts with soot to yield carbon dioxide.

In repetitive tests in loose contact mode, the Ag doped CeO_2 catalysts showed stable performance after a small initial decrease (down to approximately 90% of the initial performance for the case of CeO_2:Ag 10:1 films) whereas the performance of the pure Ag_2O films decreased by 50% after the first test and continued to decrease thereafter.

Overall, the results show that Ag-doped CeO_2 films grown by ALD are effective and stable as catalysts for soot oxidation.

Author Contributions: Conceptualization, T.V.I. and A.B., D.C.C.; Methodology, T.V.I., T.H., D.C.C.; Investigation, T.V.I., T.H., A.B., D.C.C.; Writing—Original Draft Preparation, T.V. Ivanova, D.C.C; Supervision, D.C.C.

Funding: This research was funded by TEKES, the Finnish Agency for Technology and Innovation (70006/13), European Regional Development Fund (project CZ.1.05/2.1.00/03.0086), and Ministry of Education Youth and Sports of Czech Republic (project LO1411 (NPU I)).

Acknowledgments: Acknowledgment is given to Monika Stupavská and Pavel Souček for acquiring XPS and XRD data.

Conflicts of Interest: The authors declare no conflict of interest.

References

1. Neeft, J.P.A.; Makkee, M.; Moulijn, J.A. Diesel particulate emission control. *Fuel Process. Technol.* **1996**, *47*, 1–69. [CrossRef]
2. Nielsen, T.; Jørgensena, H.E.; Larsen, J.C.; Poulsen, M. City air pollution of polycyclic aromatic hydrocarbons and other mutagens: Occurrence, sources and health effects. *Sci. Total Environ.* **1996**, *189–190*, 41–49. [CrossRef]
3. Anda, A.; Illes, B. Impact of simulated airborne soot on maize growth and development. *J. Environ. Prot.* **2012**, *3*, 773–781. [CrossRef]
4. Stratakis, G.A.; Stamatelos, A.M. Thermogravimetric analysis of soot emitted by a modern diesel engine run on catalyst-doped fuel. *Combust. Flame* **2003**, *132*, 157–169. [CrossRef]
5. Jequirim, M.; Tshamber, V.; Brilac, J.F.; Ehrburger, P. Oxidation mechanism of carbon black by NO_2: Effect of water vapour. *Fuel* **2005**, *84*, 1949–1956. [CrossRef]

6. Pisarello, M.L.; Milt, V.; Peralta, M.A.; Querini, C.A.; Miró, E.E. Simultaneous removal of soot and nitrogen oxides from diesel engine exhausts. *Catal. Today* **2002**, *75*, 465–470. [CrossRef]
7. Prasad, R.; Bella, V.R. A review on diesel soot emission, its effect and control. *Bull. Chem. React. Eng. Catal.* **2010**, *5*, 69–86. [CrossRef]
8. Trovarelli, A.; de Lietenburg, C.; Boaro, M.; Dolcetti, G. The utilization of ceria in industrial catalysis. *Catal. Today* **1999**, *50*, 353–367. [CrossRef]
9. Machida, M.; Murata, Y.; Kishikawa, K.; Zhang, D.; Ikeue, K. On the reasons for high activity of CeO_2 catalyst for soot oxidation. *Chem. Mater.* **2008**, *20*, 4489–4494. [CrossRef]
10. Oliveira, C.F.; Garcia, F.A.C.; Araujo, D.R.; Macedo, J.L.; Dias, S.C.L.; Dias, J.A. Effects of preparation and structure if cerium-zirconium mixed oxides on diesel soot catalytic combustion. *Appl. Catal. A Gen.* **2012**, *413–141*, 292–300. [CrossRef]
11. Krishna, K.; Bueno-Lopez, A.; Makkee, M.; Moulijin, J.A. Potential rare earth modified CeO_2 catalysts for soot oxidation: I. Characterisation and catalytic activity with O_2. *Appl. Catal. B Environ.* **2007**, *75*, 189–200. [CrossRef]
12. Vinodkumar, T.; Rao, B.G.; Reddy, B.M. Influence of isovalent and aliovalent dopants on the reactivity of cerium oxide for catalytic applications. *Catal. Today* **2015**, *253*, 57–64. [CrossRef]
13. Durgasri, D.N.; Vinodkumar, T.; Lin, F.; Alxneit, I.; Reddy, B.M. Gandolinium doped cerium oxide for soot oxidation: Influence of interfacial metal-support interactions. *Appl. Surf. Sci.* **2014**, *314*, 592–598. [CrossRef]
14. Bueno-Lopez, A.; Krishna, K.; Makkee, M.; Mouljin, J.A. Enhanced soot oxidation by lattice oxygen via La3+-doped CeO_2. *J. Catal.* **2005**, *230*, 237–248. [CrossRef]
15. Atribak, I.; Bueno-Lopez, A.; Garcia-Garcia, A. Combined removal of diesel soot particulates and NO_x over CeO_2-ZrO_2 mixed oxides. *J. Catal.* **2008**, *259*, 123–132. [CrossRef]
16. Scire, S.; Riccobene, S.P.M.; Crisafulli, C. Ceria supported group IB metal catalysts for the combustion of volatile organic compounds and the preferential oxidation of CO. *Appl. Catal. B Environ.* **2010**, *101*, 109–117. [CrossRef]
17. Tarasov, A.L.; Przhevalskaya, L.K.; Shvets, V.A.; Kazanskii, V.B. Influence of the metal-oxide electronic interaction on the reactivity of adsorbed oxygen radicals. Applied catalysts containing cerium oxide and Cu, Ag, and Au. *Kinet. Katal.* **1988**, *29*, 1181–1188.
18. Soria, J.; Martinez-Arias, A.; Conesa, J.C. Effect of oxidized rhodium on oxygen adsorption on cerium oxide. *Vacuum* **1992**, *43*, 437–440. [CrossRef]
19. Rangaswamy, A.; Sudarsanam, P.; Reddy, B.M. Rare earth metal doped CeO_2-based catalytic materials for diesel soot oxidation at lower temperatures. *J. Rare Earths* **2015**, *33*, 1162–1169. [CrossRef]
20. Aneggi, E.; Llorca, J.; de Leitenburg, C.; Dolcetti, G.; Trovarelli, A. Soot combustion over silver-supported catalysts. *Appl. Catal. Environ.* **2009**, *91*, 489–498. [CrossRef]
21. Hanedaa, M.; Towata, A. Catalytic performance of supported Ag nano-particles prepared by liquid phase chemical reduction for soot oxidation. *Catal. Today* **2015**, *242*, 351–356. [CrossRef]
22. Kuwahara, Y.; Fujibayashi, A.; Uehara, H.; Mori, K.; Yamashita, H. Catalytic combustion of diesel soot over Fe and Ag-doped manganese oxides: Role of heteroatoms in the catalytic performances. *Catal. Sci. Technol.* **2018**, *8*, 1905–1914. [CrossRef]
23. Shimizu, K.; Kawachi, H.; Satsuma, A. Study of active sites and mechanism for soot oxidation by silver-loaded ceria catalyst. *Appl. Catal. B Environ.* **2010**, *96*, 169–175. [CrossRef]
24. Preda, G.; Pacchioni, G. Formation of oxygen active species in Ag-modified CeO_2 catalyst for soot oxidation: A DFT study. *Catal. Today* **2011**, *177*, 31–38. [CrossRef]
25. Yamazaki, K.; Kayama, T.; Dong, F.; Shinjoh, H. A mechanistic study on soot oxidation over CeO_2-Ag catalyst with 'rice-ball' morphology. *J. Catal.* **2011**, *282*, 289–298. [CrossRef]
26. Castoldi, L.; Aneggi, E.; Matarrese, R.; Bonzi, R.; Llorca, J.; Trovarelli, A.; Lietti, L. Silver-based catalytic materials for the simultaneous removal of soot and NO_x. *Catal. Today* **2015**, *258*, 405–415. [CrossRef]
27. O'Neill, B.J.; Jackson, D.H.K.; Lee, J.; Canlas, C.; Stair, P.C.; Marshall, C.L.; Elam, J.W.; Kuech, T.F.; Dumesic, J.A.; Huber, G.W. Catalyst design with atomic layer deposition. *ACS Catal.* **2015**, *5*, 1804–1825. [CrossRef]
28. Ivanova, T.V.; Toivonen, J.; Homola, T.; Maydannik, P.S.; Kääriäinen, T.; Sillanpää, M.; Cameron, D.C. Atomic layer deposition of cerium oxide for potential use in diesel soot combustion. *J. Vac. Sci. Technol. A* **2016**, *34*, 031506. [CrossRef]

29. Masango, S.S.; Peng, L.; Marks, L.D.; Van Duyne, R.P.; Stair, P.C. Nucleation and growth of silver nanoparticles by AB and ABC-type atomic layer deposition. *J. Phys. Chem. C* **2014**, *118*, 17655–17661. [CrossRef]
30. Puurunen, R.; Vandervorst, W. Island growth as a growth mode in atomic layer deposition: A phenomenological model. *J. Appl. Phys.* **2004**, *96*, 7686. [CrossRef]
31. Shannon, R.D. Revised effective ionic radii and systematic studies of interatomic distances in halides and chalcogenides. *Acta Crystallogr. A* **1976**, *32*, 751–767. [CrossRef]
32. Cui, X.S. *The Basic Theory of Solid Chemistry*; Beijing Institute of Technology Printing: Beijing, China, 1991. (In Chinese)
33. Murray, B.J.; Li, Q.; Newberg, J.T.; Menke, E.J.; Hemminger, J.C.; Penner, R.M. Shape- and size-selective electrochemical synthesis of dispersed silver(I) oxide colloids. *Nano Lett.* **2005**, *5*, 2319–2324. [CrossRef] [PubMed]
34. Tjeng, L.H.; Meinders, M.B.J.; van Elp, J.; Ghijsen, J.; Sawatzky, G.A.; Johnson, R.L. Electronic structure of Ag_2O. *Phys. Rev. B* **1990**, *41*, 3190–3194. [CrossRef]
35. Abe, Y.; Hasegawa, T.; Kawamura, M.; Sasaki, K. Characterization of Ag oxide thin films prepared by reactive RF sputtering. *Vacuum* **2004**, *76*, 1–6. [CrossRef]
36. Kaspar, T.C.; Droubay, T.; Chembers, S.A.; Bagus, P.S. Spectroscopic evidence for Ag(III) in highly oxidized silver films by X-ray photoelectron spectroscopy. *J. Phys. Chem. C* **2010**, *114*, 21562–21571. [CrossRef]
37. Ferraria, A.M.; Carapeto, A.P.; do Rego, A.M.B. X-ray photoelectron spectroscopy: Silver salts revisited. *Vacuum* **2012**, *86*, 1988–1991. [CrossRef]
38. Sadanandam, G.; Kumari, V.D.; Scurrell, M.S. Highly stabilized Ag_2O-loaded nano TiO_2 for hydrogen production from glycerol: Water mixtures under solar light irradiation. *Int. J. Hydrogen Energy* **2017**, *42*, 807–820. [CrossRef]
39. Zhang, H.; Wang, G.; Chen, D.; Lv, X.; Li, J. Tuning photoelectrochemical performances of Ag-TiO_2 nanocomposites via reduction/oxidation of Ag. *Chem. Mater.* **2008**, *20*, 6543–6549. [CrossRef]
40. Xin, B.; Jing, L.; Ren, Z.; Wang, B.; Fu, H. Effects of simultaneously doped and deposited Ag on the photocatalytic activity and surface states of TiO_2. *J. Phys. Chem.* **2005**, *109*, 2805–2809. [CrossRef] [PubMed]
41. Priya, K.V.B.R.; Shukla, S.; Biju, S.; Reddy, M.L.P.; Patil, K.; Warrier, K.G.K. Comparing ultraviolet and chemical reduction techniques for enhancing photocatalytic activity of silver oxide/silver deposited nanocrystalline anatase titania. *J. Phys. Chem. C* **2009**, *113*, 6243–6255. [CrossRef]
42. Li, J.; Xu, J.; Dai, W.-L.; Fan, K. Dependence of Ag deposition methods on the photocatalytic activity and surface state of TiO_2 with twistlike helix structure. *J. Phys. Chem. C* **2009**, *113*, 8343–8349. [CrossRef]
43. Ansari, A.A.; Labis, J.P.; Alam, M.; Ramay, S.M.; Ahmed, N.; Mahmood, A. Preparation and spectroscopic, microscopic, thermogravimetric, and electrochemical characterization of silver-doped cerium(IV) oxide nanoparticles. *Anal. Lett.* **2017**, *50*, 1360–1371. [CrossRef]
44. Deshpande, S.S.; Patil, S.V.N.; Kuchibhatla, T.; Seal, S. Size dependency variation in lattice parameter and valency states in nanocrystalline cerium oxide. *Appl. Phys. Lett.* **2005**, *87*, 133113. [CrossRef]
45. Cai, S.; Zhang, D.; Zhang, L.; Huang, L.; Li, H.; Gao, R.; Shi, L.; Zhang, J. Comparative study of 3D ordered macroporous $Ce_{0.75}Zr_{0.2}M_{0.05}O_{2-\delta}$ (M = Fe, Cu, Mn, Co) for selective catalytic reduction of NO with NH_3. *Catal. Sci. Technol.* **2014**, *4*, 93–101. [CrossRef]
46. Zou, G.; Fan, Z.; Yao, X.; Zhang, Y.; Zhang, Z.; Chen, M.; Shangguan, W. Catalytic performance of Ag/Co-Ce composite oxides during soot combustion in O_2 and NO_x: Insights into the effects of silver. *Chin. J. Catal.* **2017**, *38*, 564–572. [CrossRef]
47. Bukhtiyarov, V.I.; Havecker, M.; Kaichev, V.V.; Knop-Gericke, A.; Mayer, R.W.; Schlögl, R. Atomic oxygen species on silver: Photoelectron spectroscopy and X-ray absorption studies. *Phys. Rev. B* **2003**, *67*, 235422. [CrossRef]
48. Aneggi, E.; de Leitenburg, C.; Llorca, J.; Trovarelli, A. Higher activity of diesel soot oxidation over polycrystalline ceria and ceria–zirconia solid solutions from more reactive surface planes. *Catal. Today* **2012**, *197*, 119–126. [CrossRef]

© 2018 by the authors. Licensee MDPI, Basel, Switzerland. This article is an open access article distributed under the terms and conditions of the Creative Commons Attribution (CC BY) license (http://creativecommons.org/licenses/by/4.0/).

ACTA UNIVERSITATIS LAPPEENRANTAENSIS

821. LIND, LOTTA. Identifying working capital models in value chains: Towards a generic framework. 2018. Diss.

822. IMMONEN, KIRSI. Ligno-cellulose fibre poly(lactic acid) interfaces in biocomposites. 2018. Diss.

823. YLÄ-KUJALA, ANTTI. Inter-organizational mediums: current state and underlying potential. 2018. Diss.

824. ZAFARI, SAHAR. Segmentation of partially overlapping convex objects in silhouette images. 2018. Diss.

825. MÄLKKI, HELENA. Identifying needs and ways to integrate sustainability into energy degree programmes. 2018. Diss.

826. JUNTUNEN, RAIMO. LCL filter designs for paraller-connected grid inverters. 2018. Diss.

827. RANAEI, SAMIRA. Quantitative approaches for detecting emerging technologies. 2018. Diss.

828. METSO, LASSE. Information-based industrial maintenance - an ecosystem perspective. 2018. Diss.

829. SAREN, ANDREY. Twin boundary dynamics in magnetic shape memory alloy Ni-Mn-Ga five-layered modulated martensite. 2018. Diss.

830. BELONOGOVA, NADEZDA. Active residential customer in a flexible energy system - a methodology to determine the customer behaviour in a multi-objective environment. 2018. Diss.

831. KALLIOLA, SIMO. Modified chitosan nanoparticles at liquid-liquid interface for applications in oil-spill treatment. 2018. Diss.

832. GEYDT, PAVEL. Atomic Force Microscopy of electrical, mechanical and piezo properties of nanowires. 2018. Diss.

833. KARELL, VILLE. Essays on stock market anomalies. 2018. Diss.

834. KURONEN, TONI. Moving object analysis and trajectory processing with applications in human-computer interaction and chemical processes. 2018. Diss.

835. UNT, ANNA. Fiber laser and hybrid welding of T-joint in structural steels. 2018. Diss.

836. KHAKUREL, JAYDEN. Enhancing the adoption of quantified self-tracking wearable devices. 2018. Diss.

837. SOININEN, HANNE. Improving the environmental safety of ash from bioenergy production plants. 2018. Diss.

838. GOLMAEI, SEYEDMOHAMMAD. Novel treatment methods for green liquor dregs and enhancing circular economy in kraft pulp mills. 2018. Diss.

839. GERAMI TEHRANI, MOHAMMAD. Mechanical design guidelines of an electric vehicle powertrain. 2019. Diss.

840. MUSIIENKO, DENYS. Ni-Mn-Ga magnetic shape memory alloy for precise high-speed actuation in micro-magneto-mechanical systems. 2019. Diss.

841. BELIAEVA, TATIANA. Complementarity and contextualization of firm-level strategic orientations. 2019. Diss.

842. EFIMOV-SOINI, NIKOLAI. Ideation stage in computer-aided design. 2019. Diss.

843. BUZUKU, SHQIPE. Enhancement of decision-making in complex organizations: A systems engineering approach. 2019. Diss.

844. SHCHERBACHEVA, ANNA. Agent-based modelling for epidemiological applications. 2019. Diss.

845. YLIJOKI, OSSI. Big data - towards data-driven business. 2019. Diss.

846. KOISTINEN, KATARIINA. Actors in sustainability transitions. 2019. Diss.

847. GRADOV, DMITRY. Experimentally validated numerical modelling of reacting multiphase flows in stirred tank reactors. 2019. Diss.

848. ALMPANOPOULOU, ARGYRO. Knowledge ecosystem formation: an institutional and organisational perspective. 2019. Diss.

849. AMELI, ALIREZA. Supercritical CO2 numerical modelling and turbomachinery design. 2019. Diss.

850. RENEV, IVAN. Automation of the conceptual design process in construction industry using ideas generation techniques. 2019. Diss.

851. AVRAMENKO, ANNA. CFD-based optimization for wind turbine locations in a wind park. 2019. Diss.

852. RISSANEN, TOMMI. Perspectives on business model experimentation in internationalizing high-tech companies. 2019. Diss.

853. HASSANZADEH, AIDIN. Advanced techniques for unsupervised classification of remote sensing hyperspectral images. 2019. Diss.

854. POPOVIC, TAMARA. Quantitative indicators of social sustainability applicable in process systems engineering. 2019. Diss.

855. RAMASAMY, DEEPIKA. Selective recovery of rare earth elements from diluted aqueous streams using N- and O –coordination ligand grafted organic-inorganic hybrid composites. 2019. Diss.

856. IFTEKHAR, SIDRA. Synthesis of hybrid bio-nanocomposites and their application for the removal of rare earth elements from synthetic wastewater. 2019. Diss.

857. HUIKURI, MARKO. Modelling and disturbance compensation of a permanent magnet linear motor with a discontinuous track 2019. Diss.

858. AALTO, MIKA. Agent-based modeling as part of biomass supply system research. 2019. Diss.

ISBN 978-952-335-384-8
ISBN 978-952-335-385-5 (PDF)
ISSN-L 1456-4491
ISSN 1456-4491
Lappeenranta 2019